CZECH TECHNICAL
UNIVERSITY
IN PRAGUE

FACULTY
OF ELECTRICAL
ENGINEERING

DOCTORAL
THESIS

JAKUB
POSPÍŠIL

2021

Czech Technical University in Prague
Faculty of Electrical Engineering
Department of Radioelectronics

Compact Structured Illumination Microscopy and Performance Evaluation in Live Cell Super-resolution Imaging

Doctoral Thesis

Ing. Jakub Pospíšil

Prague, October 2021

Ph.D. programme: Electrical Engineering and Information Technology (P2612)
Branch of study: Radioelectronics (2601V010)

Supervisor: Prof. Ing. Miloš Klíma, CSc.
Supervisor-Specialist: Ing. Karel Fliegel, Ph.D.

Supervisor:
Prof. Ing. Miloš Klíma, CSc.

Co-Supervisor:
Ing. Karel Fliegel, Ph.D.

Department of Radioelectronics
Faculty of Electrical Engineering
Czech Technical University in Prague
Technická 2
166 27 Prague 6
Czech Republic

Declaration

I hereby declare that I worked out the presented thesis independently and I quoted all sources used in this thesis in accord with methodical instructions about ethical principles for writing academic theses.

Prague, 24 October 2021 Jakub Pospíšil

Acknowledgements

I would like to express my sincere gratitude to my supervisor Prof. Ing. Miloš Klíma, CSc. for the continuous support of my Ph.D. studies and related research, and for his guidance. Besides my supervisor, I would like to thank my co-supervisor Ing. Karel Fliegel, Ph.D., Prof. Dr. Thomas Huser, and Ing. Tomáš Lukeš, Ph.D., for their inspiring comments and encouragement.

Special thanks go to the colleagues from the Department of Radioelectronics in Prague, Biomolecular Photonics Group in Bielefeld, and the Ph.D. colleagues, who have already defended their work, for everyday valuable discussions and motivation. Special thanks also go to all my friends, whom I had the honor to meet during my studies, for their endless support in difficult work and life moments.

I would like to express also the an acknowledgment to the European Union's Horizon 2020 research and innovation program, The Grant Agency of the Czech Republic, and to the Grant Agency of the Czech Technical University in Prague. This work has been partially supported by the program under the Marie Skłodowska-Curie Grant Agreement No. 766181 project "DeLIVER", GA17-05840S "Multicriteria optimization of shift-variant imaging system models", SGS16/167/OHK3/2T/13 "Algorithms for video-sequenced live cell super-resolution microscopy", SGS18/141/OHK3/2T/13 "Analysis and advanced algorithms for ultra-wide imaging systems", and SGS20/179/OHK3/3T/13 "Modern Optical Imaging Systems with Non-linear Point Spread Function and Advanced Algorithms for Image Data Processing".

Last but not least, I would like to thank my whole family for supporting me in my life in general.

Prague, 24 October 2021 Jakub Pospíšil

Abstract

Structured illumination microscopy (SIM) is one of the most common means of achieving a spatial resolution beyond the diffraction limit in fluorescence microscopy. The super-resolution SIM doubles the spatial resolution of optical microscopy, which is sufficient to visualize cellular organelles and their substructures at ∼100 nm. Current commercially available SR-SIM microscopes are often unaffordable to many biological laboratories and are relatively bulky systems covering more than one optical table. The high demand for inexpensive compact SR-SIM microscopes leads to the development of the custom-built systems using alternative ways of generating the striped illumination pattern essential for the SIM reconstruction, e.g., using a digital micromirror device (DMD), a ferroelectric liquid-crystal-on-silicon (FLCOS) microdisplay, or fiber optics. This thesis details development of a novel custom-built structured illumination microscopy system based on all-fiber optic components (*fiberSIM*). The proposed SIM system provides promising super-resolution results confirming the concept and indicates that *fiberSIM* could become the basis of a versatile "Plug&Play" illumination module with the capability of turning any conventional microscope into the SR-SIM microscope. Furthermore, five freely available SIM datasets with complete documentation are introduced. This SIM data provides a benchmark essential for the further development of reconstruction algorithms or analysis tools in SR-SIM microscopy. The final step in the development of a custom-built SR microscope is the quantitative evaluation of the resolution gain. In this thesis, a recently developed resolution estimation technique based on circular average power spectral density (PSD_{ca}) analysis is introduced. The proposed method allows to determine the resolution limit from a single image, which is suitable for the analysis of video sequences of a living cell. Furthermore, the most common conventional resolution assessment techniques that are able to measure the actual resolution limits of a microscope are discussed. The combination of a compact low-cost SIM illumination unit with open-source reconstruction and analysis algorithms makes SR-SIM available to any biological laboratory.

Keywords: super-resolution (SR), structured illumination microscopy (SIM), live cell imaging, fiber optics, resolution, estimation, power spectral density (PSD), Fourier transform.

Abstrakt

Mikroskopie se strukturním osvětlením (structured illumination microscopy – SIM) je jedním z nejpoužívanějších způsobů ve fluorescenční mikroskopii, jak dosáhnout prostorového rozlišení za hranicí difrakčního limitu. SIM, jako metoda schopná tzv. superrozlišení (super-resolution – SR), zdvojnásobuje prostorové rozlišení optického mikroskopu, což je dostatečné pro vizualizaci buněčných organel a jejich substruktur o velikosti ∼100 nm. Současné komerčně dostupné SR-SIM mikroskopy jsou často finančně nedostupné pro mnoho biologických laboratoří a jsou relativně objemnými systémy pokrývajícími více než jeden optický stůl. Vysoká poptávka po levných kompaktních SR-SIM mikroskopech vede k vývoji nových systémů, využívajících alternativní způsoby generování pruhovaného vzoru osvětlení nezbytného pro SIM rekonstrukci, např. pomocí digitálního mikrozrcadlového zařízení (digital micromirror device – DMD), feroelektrického mikrodispleje z tekutých krystalů (ferroelectric liquid crystal on silicon – FLCOS) nebo vláknové optiky. Tato práce podrobně popisuje vývoj nového SIM zařízení využívající komponenty vláknové optiky (*fiberSIM*). Navrhovaný SIM systém poskytuje slibné výsledky v oblasti super-resolution mikroskopie potvrzující tento koncept a ukazuje, že *fiberSIM* by se mohl stát základem pro univerzálního "Plug&Play" modulu schopný proměnit jakýkoli konvenční mikroskop v SR-SIM zařízení. Práce dále představuje pět volně dostupných SIM datových sad s kompletní dokumentací. Tato SIM data poskytují referenci nezbytnou pro další vývoj rekonstrukčních algoritmů nebo nástrojů pro analýzu v SR-SIM mikroskopii. Posledním krokem ve vývoji SR mikroskopu je kvantitativní vyhodnocení zlepšení rozlišení. V této práci je představena nedávno vyvinutá technika odhadu rozlišení založená na analýze kruhově průměrované spektrální výkonové hustoty (circular average power spectral density – $\mathrm{PSD_{ca}}$). Navržená metoda umožňuje určit limit rozlišení z jednoho snímku, což je vhodné pro analýzu videosekvencí živých buněk. Práce dále pojednává nejpoužívanější konvenční techniky hodnocení rozlišení, které jsou schopny měřit skutečné meze rozlišení mikroskopu. Kombinace kompaktní nízkonákladové osvětlovací jednotky pro SIM s open-source algoritmy pro rekonstrukci a analýzu zpřístupňuje SR-SIM mnoha biologickým laboratořím.

Klíčová slova: super-resolution (SR), mikroskopie se strukturním osvětlením (SIM), zobrazování živých buněk, vláknová optika, rozlišení, odhad, spektrální výkonová hustota (PSD), Fourierova transformace.

Contents

List of Figures

List of Tables

Glossary

A431	A specific model human cell line
Alexa Fluor 488	Green-fluorescent dye
Atto 565	Fluorescent label belonging to the class of rhodamine dyes
BFP	Back focal plane
BPAE	Bovine pulmonary artery endothelial
CCD	Charge-coupled device
CMOS	Complementary metal oxide semiconductor
DMD	Digital micromirror device
DNA	Deoxyribonucleic acid
ESF	Edge spread function
fairSIM	Free algorithms, instrumentation and resources for structured illumination microscopy
FFT	Fast Fourier transform
fiberSIM	Structured illumination microscopy system based on all-fiber optic components
FLCOS	Ferroelectric liquid-crystal-on-silicon
FOV	Field of view
FRC	Fourier ring correlation
FSC	Fourier shell correlation
FWHM	Full width at half maximum
GFP	Green fluorescent protein
HEP-G2	Human liver cancer cell line
HR	High resolution
HR-MAP	High resolution maximum a posteriori probability
imDecorr	Image decorrelation analysis
LAMP1	Lysosome-associated membrane protein 1
LCOS	Liquid crystal on silicon
LR	Low resolution
LR-HOM	Low resolution homodyne detection
LSCM	Laser scanning confocal microscopy
LSF	Line spread function
LSFM	Light-sheet fluorescence microscopy
MAP	Maximum a posteriori probability
MAP-SIM	Maximum a posteriori probability SIM
MEMS	Microelectromechanical systems

MSD	Mean-squared displacement
MTF	Modulation transfer function
NA	Numerical aperture
NL-SIM	Non-linear SIM
OS-SIM	Optical sectioning SIM
OTF	Optical transfer function
PALM	Photoactivated localization microscopy
PBS	Phosphate-buffered saline
PlanApo	Plan apochromat objective (Olympus)
PlApo	Plan apochromat objective (Leica)
PSD	Power spectral density
PSD_{ca}	Circular average power spectral density
PSF	Point spread function
ROI	Region of interest
SBR	Signal to background ratio
sCMOS	Scientific CMOS
SIM	Structured illumination microscopy
SIMFLUX	Structured illumination with minimal emission fluxes
SIMPLE	Structured illumination based point localization estimator
SLM	Spatial light modulator
SMLM	Single molecule localization microscopy
SNR	Signal to noise ratio
SOFI	Super-resolution optical fluctuation imaging
SPT	Single particle tracking
SQUIRREL	Super-resolution quantitative image rating and reporting of error locations
SR	Super-resolution
SR-SIM	Super-resolution SIM
STED	Stimulated emission depletion
STORM	Stochastic optical reconstruction microscopy
TIR	Total internal reflection
TIRF	Total internal reflection fluorescence
TIRFM	Total internal reflection fluorescence microscopy
U2-OS	Human osteosarcoma cell
UPlanApo	Universal plan apochromat objective (Olympus)
UPlanFLN	Universal plan semi apochromat objective (Olympus)
UPlanSApo	Universal plan super apochromat objective (Olympus)
VIS	Visible spectrum

Introduction

Deep understanding of all processes of the world around us was always one of the biggest priorities of mankind. Next to the other senses, vision allows us to observe, describe, or learn how the world works. However, we have reached the limit of this unique sense quite soon and instruments allowing us to see objects unobservable with the naked eye (both macro- and microscopic) take an essential role in many scientific fields. From there, observations such as galaxies far from Earth, nanostructures of the human body, or individual molecules led to a better understanding of many important processes and improved the quality of our lives. Although astronomical telescopes or optical microscopes can dramatically extend the vision of the naked eye, there are many factors setting the limits of an individual instrument. The diffraction limited optics of the optical system and aberrations due to the propagation of light through the atmosphere (in astronomy), or a tissue (in microscopy) are two main limiting factors decreasing the quality of the final observation. In the last decades, a rapid development in electronics, such as the increasing of the computation power together with the improvement of digital imaging sensors and micro-electromechanical systems (MEMS) opened many possibilities to build complex systems able to overcome the physical limits of the optical instruments.

This work covers part of the field of light microscopy applied in live cell biology. Noninvasive investigation of live cell structures is an essential part of all life science studies. For decades, light microscopy is widely used in this field. Next to brightfield microscopy or phase contrast microscopy, fluorescence microscopy allows the examination of live cells by marking individual molecules with fluorescence dyes. This microscopy technique allows us to observe the dynamics of the individual molecules in real time in the noninvasive natural environment of the cell. Despite this benefit, the resolving capability of modern light microscopes is about 200-300 nm in lateral dimension[1–3] due to diffraction of light. However, attributes of the fluorescence microscopy allow the development of a powerful microscope techniques called super-resolution (SR) microscopy. Many novel SR methods able to extend the resolution of an optical microscope beyond the diffraction limit have been developed in the last few decades. SR techniques can be divided into 4 main strategies including single molecule localization microscopy (SMLM)[4–7], super-resolution optical fluctuation imaging (SOFI)[8,9], stimulated emission depletion (STED) microscopy[10,11], and structured illumination microscopy (SIM)[12–15]. Selected fluorescence and SR techniques are discussed in the chapters *1.2: Fluorescence Microscopy Techniques* and *2.1: Super-resolution Microscopy*. Super-resolution imaging nanostructures of a cell typically requires long image sequences (up to ∼10,000 frames), which leads to the high demand on the stability of the whole system over relatively long time. To achieve the best possible quality of the SR reconstruction, modern instruments typically include high-quality optics in combination with precise opto-mechanical components fulfilling the high stability requirements. This often results in

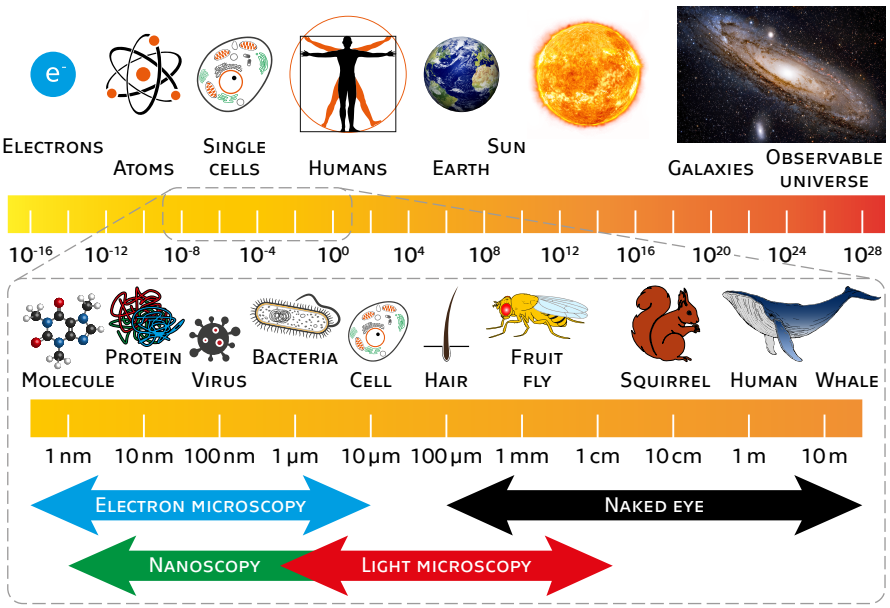

Figure 1: Scale of Nature. Upper scale shows representatives of the known world from the electrons (radius ∼0.001 fm) to the large galaxies (e.g., Milky Way with size of 52,850 light years.). Group of objects observable with a naked eye and microscopes is zoomed in the lower scale.

rather large, complex, and expensive optical systems covering one or more optical tables. High demand for super-resolution microscopes, therefore, leads to the development of compact, low-cost, and often custom-built SR devices that allow every laboratory to examine live cells with the resolution below the diffraction limit.

The final resolution enhancement can be theoretically defined for each SR technique[13,14,16]. However, every complex reconstruction method has the limitations which do not allow reaching the theoretical resolution gain. In order to compare the efficiency of different methods, the resolution assessment in reconstructed images is the essential part of SR imaging. For this purpose several resolution evaluation techniques are mostly used including full width at half maximum (FWHM) and modulation transfer function (MTF) estimation, Fourier ring correlation (FRC)[17,18], or Fourier shell correlation (FSC)[19]. Furthermore, there are several ImageJ[a] plugins combining some of the estimation techniques such as NanoJ: A high-performance open-source super-resolution microscopy toolbox including super-resolution quantitative image rating and reporting of error locations (SQUIRREL) tool[20,21]. Recently, Descloux et al. presented innovative estimation method based on decorrelation analysis[22].

[a]Image Processing and Analysis in Java, https://imagej.nih.gov/ij/

Aims of the Doctoral Thesis

Commercially available super-resolution structured illumination microscopy systems are often unaffordable for many biological laboratories investigating live cells. These SR-SIM microscopes are usually rather bulky systems covering more than one optical table. Based on this observation, the aims of the doctoral thesis can be divided into three steps:

1. To provide freely available SIM datasets as a ground truth for further SIM software development, e.g., SIM reconstruction and image quality analysis.
2. To develop a low-cost and compact SIM microscope allowing every lab to examine live cells with the resolution bellow the diffraction limit.
3. To provide a robust resolution assessment tool able to estimate resolution in one microscopy image, e.g., single frame of live cell video sequences.

Structure of the Doctoral Thesis

The thesis is organized in 4 chapters covering the necessary steps towards the aims with conclusions and future outlook. State of the art followed by the author's contribution to the field is included in both Chapter 2 and Chapter 3). The publications of the author are referred as "A-number" in the main text and are listed in the section *Publications of the Author Relevant to the Thesis* in the end of this work. The following paragraphs briefly introduce individual chapters:

1. *Light Microscopy*: Chapter introduces the fundamentals of light microscopy, especially fluorescence microscopy, and briefly discusses modern fluorescence techniques on the basic level. Presented microscopy techniques lay the groundwork for all super-resolution approaches discussed in the following chapters.
2. *Super-resolution Microscopy*: Chapter presents the overview of the most common super-resolution fluorescence microscopy techniques including single molecule localization microscopy (SMLM), super-resolution optical fluctuation imaging (SOFI), stimulated emission depletion microscopy (STED) and super-resolution structured illumination microscopy (SR-SIM). The chapter focuses on the detailed explanation of the structured illumination microscopy (SIM) technique and the recent development on a low-cost and compact approach in SIM. This development took place in close collaboration with the Biomolecular Photonics group, Bielefeld University, Germany, with the participation of the author of this thesis. Detailed description of the compact SIM system (*fiberSIM*) is major part of this chapter. Furthermore, five freely available SIM datasets created in close collaboration with UCCS Center for the Biofrontiers Institute, University of Colorado at Colorado Springs, USA, are presented.

3. *Assessing Resolution in Microscopy*: The most common resolution assessment techniques and their current development are presented. The first section provides a brief overview of the resolution limits in fluorescence microscopy. The state of the art in the field of assessing resolution includes common techniques such as full width at half maximum (FWHM), modulation transfer function (MTF), and Fourier ring correlation (FRC). Furthermore, an assessing resolution technique based on the power spectral density (PSD) analysis is presented.

4. *Conclusions*: The last chapter summarizes the results, relates them to the objectives set in the introduction, and briefly discusses the outlook for future research.

1

Light Microscopy

This chapter introduces the fundamentals of light microscopy, especially fluorescence microscopy, essential to address the aims of the thesis. Furthermore, modern fluorescence techniques are introduced that lay the groundwork for all super-resolution microscopy approaches discussed in the following chapter.

Contents

1.1 Fundamentals of Light Microscopy

The resolution of a standard light microscope is restricted by the Abbe diffraction limit[23]. Modern optical microscopes can achieve the maximum resolving capability at ∼200 nm[1,3]. This resolution barrier could be overcome with an electron microscope, due to the much smaller wavelength of an electron (typically a few picometers)[24] compared to the photons (in the range of ∼380-700 nm for visible light). This allows one to investigate nanostructures with details of the size below nanometers. However, the minimal needed electron dose to obtain required contrast is often higher than the lethal dose known to cause live cell death[25]. Despite recent research on live cell electron microscopy[25–27], the light microscopy, particularly fluorescence microscopy, is still the most common choice for researchers in molecular and live cell biology.

1.1.1 Fluorescence Microscopy

Fluorescence microscopy is a powerful tool which provides a possibility to examine individual fluorescent molecules. In standard light microscopy, light passes through a sample and the observed image depends on the specimen properties of light absorption, optical path differences, phase gradient, and refraction. In contrast to that, fluorescence microscopy allows the visualization of single molecules that fluoresce after excitation with light. The investigation of intracellular location, movements of macromolecules, and molecular mechanisms of large macromolecules is possible using this technique.[3]

This kind of microscopy is based on tagging the molecule with fluorescent dyes to make it visible after external excitation by laser light. Great progress in the field of biochemistry and microscopy led to the Nobel Prize in Chemistry in 2014[28] awarded for the development of super-resolved fluorescence microscopy. Different types of fluorescent probes, labeling methods, light excitation methods, instrumentation, and imaging techniques make the evolution of super-resolution techniques possible. The excitation of the stained sample with a specific illumination pattern gives the basis for structured illumination microscopy imaging.

Fluorescence is the emission of photons by molecules whose electrons are stimulated to a higher excitation state by an external excitation laser. Once the fluorescent molecule absorbs an excitation photon of the wavelength λ_{ex}, the absorbed photon interacts with an electron, which is then excited to a higher energy state, the excited singlet state. The collapse of the excited electron to its initial ground state is almost immediate. Within this energy collapse, the molecule releases the absorbed energy as a fluorescent photon with the wavelength λ_f. There is some energy loss in the process, which leads to the lower oscillation and longer wavelength of the emitted fluorescent photon than the absorbed photon. These energy losses are typically referred

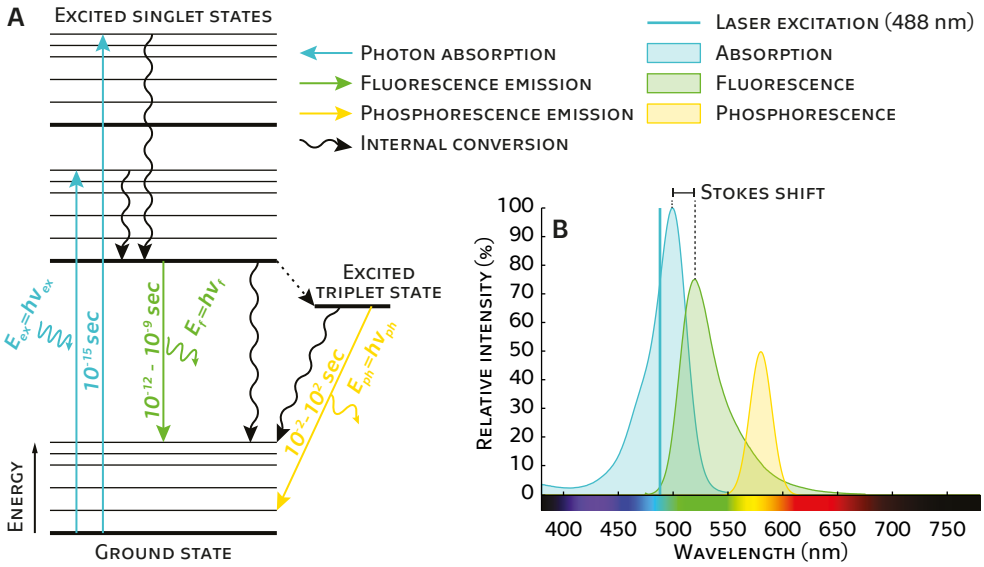

Figure 1.1: Jablonski diagram showing energy levels occupied by an excited electron within a fluorescent molecule (A) and an example of the spectrum diagram (B). Fluorescent dye absorbs excitation photons ($\lambda_{ex} = 488\,\text{nm}$) with the energy of $E_{ex} = h\nu_{ex}$, where h is the Planck constant and $\nu = c/\lambda$ represents the photon frequency, where c is the speed of light. This absorption excites electrons from the ground state to the excited state (blue arrows). Excited electrons then collapse back to the ground state on one of three following pathways. Fluorescence, where photons with lower energy $E_f = h\nu_f$ (higher wavelength λ_f) are emitted (green arrow); internal conversion, where no photons are emitted (black wavy arrows); or an electron can enter the triplet state, which can make the molecule chemically reactive (black dashed arrow). Electrons in triplet state can return to the ground state through internal conversion or by photon emission of phosphorescence. All black wavy arrows represent internal conversion where no photons are emitted. Energy losses in this process (mostly transformed into heat) are demonstrated in the graph (B) by decreasing the relative intensity of the emission spectra. The difference between the absorption and emission maxima is called Stokes shift.

to as vibronic states (internal conversion). The absorption and emission events occur almost simultaneously and the whole fluorescence process typically has a duration of picoseconds to nanoseconds. Therefore, fluorescence stops when there is no exciting incident light. However, there are molecules in which the electron can enter the triplet state. Then, the period between absorption and emission (at wavelength λ_{ph}) lasts fractions of seconds to minutes. This emission process is called phosphorescence. The molecules with electrons in this triplet state are chemically reactive[3]. Both situations are illustrated in Figure 1.1.

1.2 Fluorescence Microscopy Techniques

In this section, the fundamentals of the most common fluorescence microscopy techniques are described. These techniques include conventional widefield microscopy (hereinafter Widefield), total internal reflection fluorescence (TIRF) microscopy, confocal microscopy, and light sheet microscopy.

1.2.1 Widefield Microscope

A conventional widefield microscope represents the base for fluorescence microscopy. Any other fluorescence microscopy technique is technically a modification of this fundamental setup. In contrast to a bright-field microscope, which illuminates the sample from the bottom with white light and observes the sample from the top, a fluorescence microscope illuminates the sample typically with a single color light through an objective lens from the bottom and observes it with the same objective lens from the same direction (see Figure 1.2).

Widefield illumination is generated by focusing the excitation laser beam to the center of the pupil plane of the objective lens. The collimated beam then illuminates the full range of the field of view (FOV). However, the illumination has typically a Gaussian profile over the FOVresulting in lower excitation of the fluorophores further from the center of the FOV, thus lower fluorescence intensity at the edge of the FOV. This effect known as "vignetting" is not that problematic in the investigation of a single cell in the

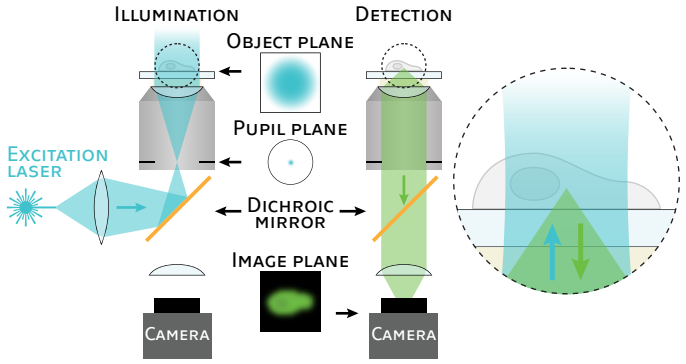

Figure 1.2: Schematics of the conventional fluorescence microscope setup. Widefield illumination of the sample is achieved by focusing the excitation laser beam to the center of the pupil plane of the objective lens. Fluorescence light is collected by the objective lens, transmitted through a dichroic mirror and focused on the camera chip by a tube lens.[b]

center of the FOV. However, it can bring a lot of difficulties in further postprocessing of large sample imaging, where the region of interest (ROI) (larger than FOV of an objective lens) is subdivided into multiple images. These images are then combined via stitching to a larger FOV. Vignetting then causes inequalities in the final large image and the stitching grid can be clearly distinctive. Furthermore, the illumination of the whole sample does not allow a proper tissue sectioning in the axial dimension. Despite focusing the objective lens in a single axial plane, the bright fluorescence signals from the outside of the focal plane (out-of-focus fluorescence) increase the intensity of the background, thus dramatically reduce the final contrast of the image.

1.2.2 Total Internal Reflection Fluorescence Microscope

Total internal reflection fluorescence TIRF microscopy extends widefield technique by optical sectioning and dramatic reduction of the out-of-focus fluorescence contribution in two-dimensional microscopy imaging. The key for the TIRF illumination is a shift of the focus point at the pupil plane of an objective lens from the center in the lateral dimension (see Fig. 1.4). This results in the change of the incidence angle of the illumination beam on the sample coverslip. If the incident angle θ of the excitation beam on the coverslip is larger than the critical angle, the light beam undergoes total internal reflection (TIR) and does not propagate deep into the sample. The critical angle, θ_c, is given by Snell's law[29]

$$\theta_c = sin^{-1}\left(\frac{n_1}{n_2}\right), \tag{1.1}$$

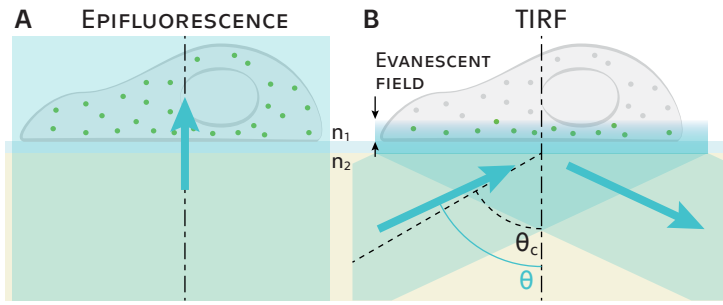

Figure 1.3: Total internal reflection fluorescence TIRF principle. (A) Epifluorescence typical for Widefield microscopes excites all fluorophores in the sample, which results in bright out-of-focus fluorescence, thus low-contrast images of an examined sample. (B) Illustration of the TIRF illumination. If the incidence angle θ of the excitation beam is larger than the critical angle θ_c, a thin field close to the coverslip is illuminated and most of the light is reflected back to the objective lens. The critical angle θ_c is defined by Snell's law (Eq. 1.1) and depends on the refractive indices of the sample and the coverslip/immersion oil, respectively.

where n_1 and n_2 are the refractive indices of the sample and the coverslip/immersion oil, respectively. To achieve TIR, the refractive index of the sample must be less than the refractive index of the coverslip. The thin layer close to the coverslip exciting the fluorophores in the sample is called the evanescent field. The thickness of this field is typically less then 0.2 µm[1,30]. This results to very thin optical sectioning and effective out-of-focus fluorescence elimination. Furthermore, significant signal-to-noise ratio (SNR) improvement can be achieved by using TIRF microscopy. The higher the numerical aperture (NA) of the objective lens, the lower gets the possible penetration depth of the evanescent field. From Figure 1.3 is, however, obvious that deep penetration into the sample is not possible and TIRF is limited to the 2D imaging of thin samples stuck on the cover glass, i.e., cell samples.

The TIRF microscope setup is very similar to the widefield microscope. The main difference is in the illumination path, where the excitation laser beam is focused on the pupil plane of the objective with the specific lateral offset. This offset ensures the incidence angle θ, which is necessary to achieve the total internal reflection.

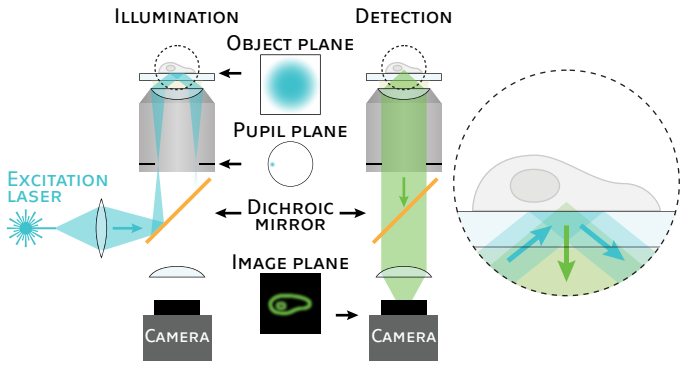

Figure 1.4: Fundamental setup of total internal reflection fluorescence TIRF microscope. Excitation laser beam is focused to the pupil plane of the objective with a lateral shift from the center. Specific shift of the beam results in the increasing incidence angle θ on the coverslip, which leads to the total internal reflection, thus very thin evanescent field in the sample lying on the coverslip. The imaging path is exactly the same as with the widefield microscope. TIRF brings the advantage of thin optical sectioning and reducing the out-of-focus fluorescence from the outside of the focal plane.[b]

1.2.3 Light-Sheet Fluorescence Microscopy

Light-sheet fluorescence microscopy (LSFM) is based on an orthogonal imaging geometry where the sample is illuminated from the side and fluorescence is collected at 90° with a high-numerical-aperture objective lens. The excitation beam is typically generated by the second objective lens in combination with a cylindrical lens, which results in a

narrow (in z direction) but wide (in x direction) illumination beam in the object plane. Positioning the illumination beam at the focal plane of the collecting objective lens ensures that the fluorescence excitation above and below the depth of focus is minimized. This results in efficient optical sectioning and avoiding unnecessary illumination of the specimen, which also helps to reduce the photobleaching (light-induced degradation)[31] of fluorophores out of the plane in focus. In comparison with TIRF which offers efficient optical sectioning as well, LSFM allows the volumetric scanning of the specimen. However, the illumination objective lens and collecting objective lens have to be fixed in the perpendicular position with respect to each other (light-sheet beam must stay in the focal plane of the collecting objective lens). Therefore, the scanning is typically performed by moving the sample z-axis with respect to the collecting objective lens. Recent developments in light-sheet fluorescence microscopy brought several options of volumetric scanning without necessity of sample manipulation[32–35].

Despite excellent optical sectioning with the option of rapid 3D imaging of larger volumes, the resolution of the final LSFM image is still dependent mostly on the detection objective lens. The objective lens with higher numerical aperture is usually quite large, and the working distance is typically in the range of tenths of a millimeter. Thus, detection and illumination objective lens must be in very close configuration (almost touching), which makes the LSFM setups very complicated to build. Furthermore, this configuration requires both objective lenses to be immersed in the immersion medium, which is often performed by using customized sample chambers. Manipulation of the biological samples become very complicated and it typically requires some training to be able operate LSFM. However, several approaches appeared to solve this difficulty[36,37].

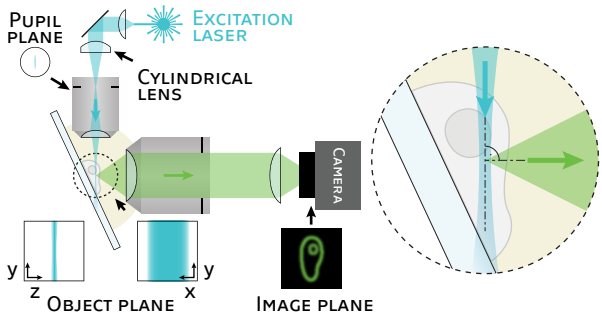

Figure 1.5: Fundamental setup of a light-sheet fluorescence microscope LSFM. The illumination beam (blue) is typically focused in only one direction by a cylindrical lens (see y-z and x-y profiles in object plane) and is perpendicular to the detection path (green). This configuration provides good optical sectioning with relatively large field of view. Volumetric scanning can be performed by moving the sample along the z-axis of the detection path. Both illumination and detection objective lens have to be immersed in the immersion medium such as water. Therefore, a specimen chamber filled with the immersion oil is often required.[b]

1.2.4 Laser Scanning Confocal Microscopy

In contrast to the widefield and TIRF microscopy, the excitation laser beam in a standard laser scanning confocal microscope (LSCM) fills the objective lens pupil plane, which generates a focused spot in the object plane. This focal point only excites a low number of the fluorophores mostly in the focal plane of the objective lens. Emitted light from the excited fluorophores is collected by the same objective lens and detected using a photodetector[38]. The image of the full field of view is then obtained by scanning with a rapid x-y scanning mirror. Confocal microscopy is capable of effective optical sectioning mostly by placing a finite pinhole in front of the photodetector right in the focal plane of the tube lens (see Fig. 1.6). This pinhole effectively blocks the out-of-focus fluorescence collected by the objective lens, which leads to higher contrast in the final confocal microscopy image. Although conventional LSCM provides 2D imaging, several confocal approaches extending LSCM to 3D are available[39–42]. Confocal microscopy can improve the resolution by 25% and ∼43% in lateral and axial dimensions, respectively. Resolution limits are discussed in more detail in the section *1.3: Resolution in Microscopy*.

In 1988, the rapid (real-time) scanning confocal microscopy using the Nipkow disk (see Fig. 1.6B), referred as spinning-disk confocal microscopy, was introduced[43]. While

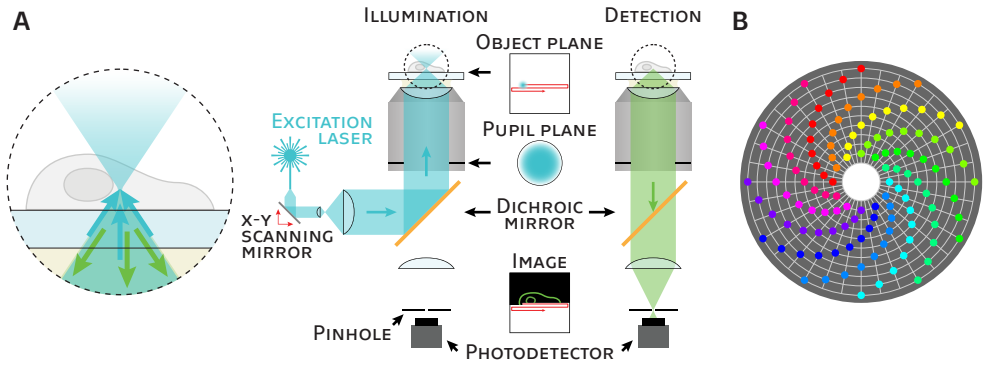

Figure 1.6: Fundamental setup of laser scanning confocal microscope LSCM (A). The pupil plane of the objective lens is filled with the illumination laser in order to generate a focused spot in the object plane. This spot excites a low number of fluorophores which emit the light collected by the objective lens. The detection of the fluorescence signals is performed by focusing the light onto a photodetector. A finite pinhole is placed in front of the photodetector leading to effective blocking of the out-of-focus fluorescence collected by the objective lens. The result of this blocking is improvement of the dynamic contrast in the final image. (B) Illustration of the Nipkow disk used for rapid scanning confocal microscopy. Color dots represents pinholes while the color codes each Archimedean spiral.[b]

[b]Figure was adapted with permission from "Super-resolution microscopy demystified," by Schermelleh, L., Ferrand, A., Huser, T. et al. Nat. Cell Biol. 21(1), p. 73. Copyright 2019 by Springer Nature Limited.

the Nipkow disk offers the scanning of multiple individual spots at the same time, it is necessary to exchange the photodetector for a camera (typically CCD sensor). This approach, however, brings several advantages to the concept of confocal microscopy. Charge-coupled device (CCD) cameras have higher quantum efficiency (65–90%) than photomultiplier tubes (∼50%) or avalanche photodiodes (∼40%). Furthermore, the higher detection sensitivity reduces the imaging exposure time, resulting in higher frame rates with equivalent image signal-to-noise ratio (SNR). Faster and more efficient spinning disk-scanning is capable of fast confocal imaging at 10-100× the rate of conventional laser scanning confocal microscope[43,44]. Further, the spinning-disk approach has been shown to cause significantly less photobleaching compared to LSCM leading to live cells imaging for considerably longer periods of time with lower risk of phototoxic degradation[45–47].

1.2.5 Summary of the Conventional Methods

Widefield fluorescence microscopy is one of the most used means for noninvasive examination of live cell structures and dynamics. Real-time imaging of the cell dynamics is achieved thanks to the simplicity of the widefield setup. The speed of the system only depends on the camera frame rate. Modern high-resolution microscope objective lenses allow biologists to observe structures with details slightly below 200 nm, depending on emission wavelengths. However, epifluorescence in a standard widefield microscope (Fig. 1.3A) leads to the decreasing dynamic range (contrast) due to the emission light coming from the emitters below and above the focal plane (out-of-focus light). This effect causes the decreasing of the resolving capability of the microscope. Increasing the contrast, thus resolution, can be achieved by image postprocessing (deconvolution and filtering) or by using objective lenses allowing total internal reflection fluorescence (TIRF) illumination. TIRF is an efficient way to instantly suppress the out-of-focus light from the observed sample, thus enhance the resolving capability of the microscope. However, volumetric imaging is not possible since the penetration depth of the evanescent field is typically around 100-150 nm (Fig. 1.3B)[48]. Therefore, only 2D structures stuck on the cover glass surface can be observed. Another way of real-time imaging with good optical sectioning is the light sheet microscope. This approach also brings the possibility of volumetric scanning. Despite the progress in optical sectioning, the light detection in all three methods is still diffraction limited, thus the resolution varies around 200 nm. Laser scanning confocal microscopy, however, is capable to enhance the lateral resolution by 25% with efficient optical sectioning. Moreover, the confocal microscope can also increase the axial resolution by ∼45%[3,38]. Despite this method is based on point scanning, several studies have shown the ability of real-time volumetric scanning. Although confocal microscopy overcomes the weaknesses of the widefield, the resolution limit is not sufficient anymore in many applications. Biologists' demands for higher resolution inevitably led to the invention of techniques called super-resolution SR microscopy. Chapter 2 deals with the most common SR techniques and outlines the current development in this field.

1.3 Resolution in Microscopy

Before defining the diffraction limit in microscopy, the numerical aperture of an objective lens has to be explained[3]. Figure 1.7 illustrates a diffraction limited objective lens and its response (point spread function - PSF) to a single infinitely small light source (2D Dirac delta function). When a point object is observed through the objective lens, the diffraction pattern consisting of a central spot (diffraction disk) surrounded by a series of diffraction rings can be observed. This point source diffraction pattern is referred to as an Airy disk. The size of the Airy disk depends on the wavelength λ of the light source, the refractive index of the medium in which the lens is working (1.00 for air, 1.333 for water, and typically 1.515 for immersion oil)[3], and the numerical NA aperture of the objective lens

$$\mathrm{NA} = n \cdot \sin\theta, \tag{1.2}$$

where θ is the half angle over which the objective lens can collect light coming from a focused object (see Fig. 1.7B)[3].

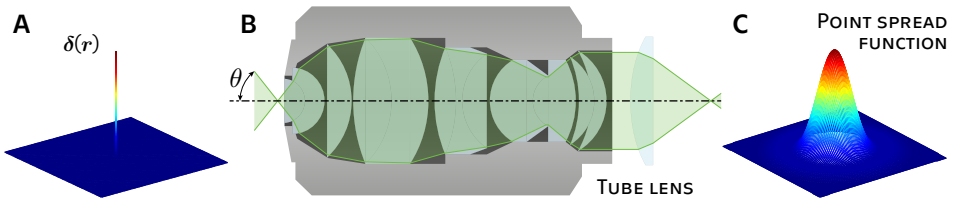

Figure 1.7: The illustration of a microscope objective lens with it's response (PSF) on the single point light source. (A) Two dimensional delta function representing a single point light source. (B) A cross section of the microscopes' objective lens with the typical configuration of the inner lenses. The illustration includes a tube lens focusing the light typically on the camera chip. Angle θ represents the half of the angle over which the objective lens collects light coming from the focal plane. This angle defines the final numerical aperture NA (see Eq. 1.2). (C) Point spread function in the shape of Airy disk as the response of an objective lens to the 2D delta function (A).

1.3.1 Spatial Resolution Limits

Spatial resolution, also known as resolving capability, of conventional microscopy is limited due to the diffraction of light. Every spot of light (Fig. 1.7A) observed by the microscope objective with a circular aperture is spread into the Airy disk (Fig. 1.7C). The diffraction limit describes the smallest resolvable distance between two points observed through an optical system. In 1937, German physicist Ernst Abbe defined the

resolution limit as[3,23]

$$d_{Abbe,\,lateral} = \frac{0.5\lambda}{\mathrm{NA}}, \tag{1.3}$$

in lateral dimension. 23 years later, in 1896, Lord Rayleigh redefined the Abbe diffraction limit to quantify the necessary separation between two Airy patterns to distinguish them as separate entities[3,49]. Rayleigh diffraction limit is then defined as

$$d_{Rayleigh,\,lateral} = \frac{0.61\lambda}{\mathrm{NA}}, \tag{1.4}$$

in lateral dimension. Compared to the Abbe lateral diffraction limit, the higher constant here corresponds to having a certain minimum modulation to be able to resolve the objects. Although Rayleigh diffraction limit in lateral dimension differs from Abbe, in the case of axial dimension, both definitions lead to the same diffraction limit[3,50,51]

$$d_{axial} = \frac{2n\lambda}{\mathrm{NA}^2}, \tag{1.5}$$

where n refers to the refractive index from Eq. 1.2.

Spatial resolution limit is often referred to as the cut-off frequency (f_c) in the Fourier domain. The cut-off frequency can be expressed as

$$f_c = 2\mathrm{NA}/\lambda, \tag{1.6}$$

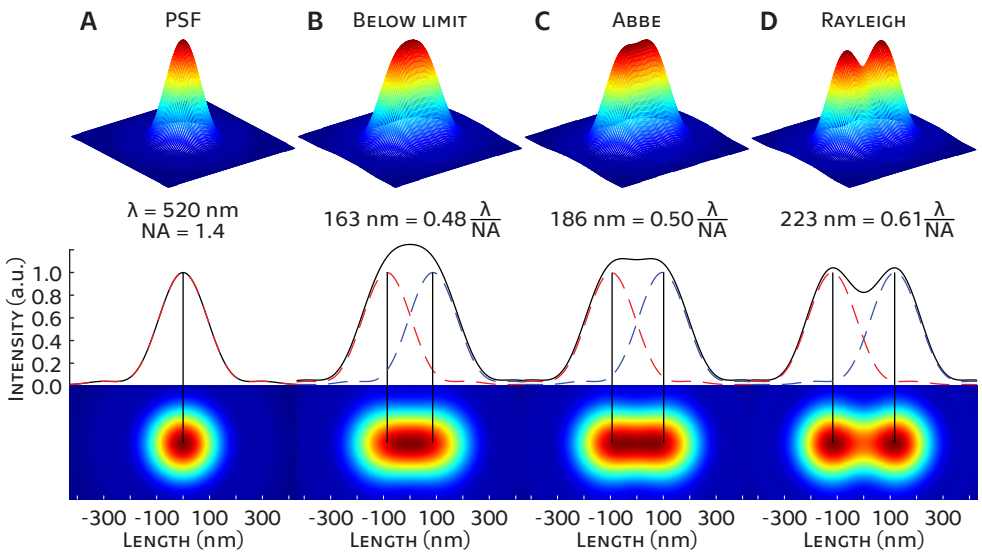

Figure 1.8: Simulation of point spread function (PSF) of the light microscope with an illustration of the diffraction limit. (A) PSF model for NA = 1.4, λ = 520 nm for green-fluorescence dye Alexa Fluor 488. (B) Example of two indistinguishable light sources - distance between sources is below the Abbe diffraction limit. (C) The Abbe diffraction limit definition. (D) The Rayleigh diffraction limit definition for a microscope.

which corresponds inversely to the Abbe diffraction limit (Eq. 1.3).

As mentioned in the Section 1.2.4, confocal microscopy can enhance the resolution by 25% in lateral and ∼43% in axial dimension. The resolution limit of the confocal microscope can be approximated as

$$d_{lateral} = \frac{0.4\lambda}{\mathrm{NA}} \tag{1.7}$$

in lateral dimension, and

$$d_{axial} = \frac{1.4n\lambda}{\mathrm{NA}^2} \tag{1.8}$$

in axial dimension[3,38].

1.3.2 DIGITAL MICROSCOPY

Digital cameras play a significant role in fluorescence microscopy. Many modern fluorescence microscopy systems use scientific-grade cameras that are designed to cover the requirements of a specific application. High demands on the detector with respect to sensitivity, noise, and image acquisition speed are placed in super-resolution microscopy. In this section, mainly a suitable pixel size with respect to the digital image sampling is discussed. To preserve the objective lens resolution during the acquisition with a digital camera, the Nyquist–Shannon sampling theorem must be fulfilled. The spatial sampling frequency must be at least two times the maximum spatial frequency (cut-off

Table 1.1: Digital imaging in microscopy. Example of three different digital cameras used with two objective lenses. Green and yellow color in emission wavelength row indicates the wavelength of the emission. Colored numbers in the table represent fulfilling the Nyquist–Shannon sampling theorem as following: Red - camera is not suitable for imaging in this configuration. Orange - camera fulfills the sampling theorem, but upsampling is required in SR-SIM reconstruction. Green - camera is well suitable for SR imaging with no need of upsampling in SR-SIM reconstruction.

Objective lens		PlanApo 60×1.45		UPlanApo 100×1.50	
Emission wavelength (nm)		546	590	546	590
Cut-off frequency (µm^{-1})		5.31	4.92	5.49	5.08
Camera model	Pixel size (µm)	Sampling frequency (µm^{-1})			
IDS UI-3270CP	3.45	8.70	8.70	14.49	14.49
PCO Edge 5.5	6.50	4.62	4.62	7.69	7.69
Camera	9.80	3.06	3.06	5.10	5.10

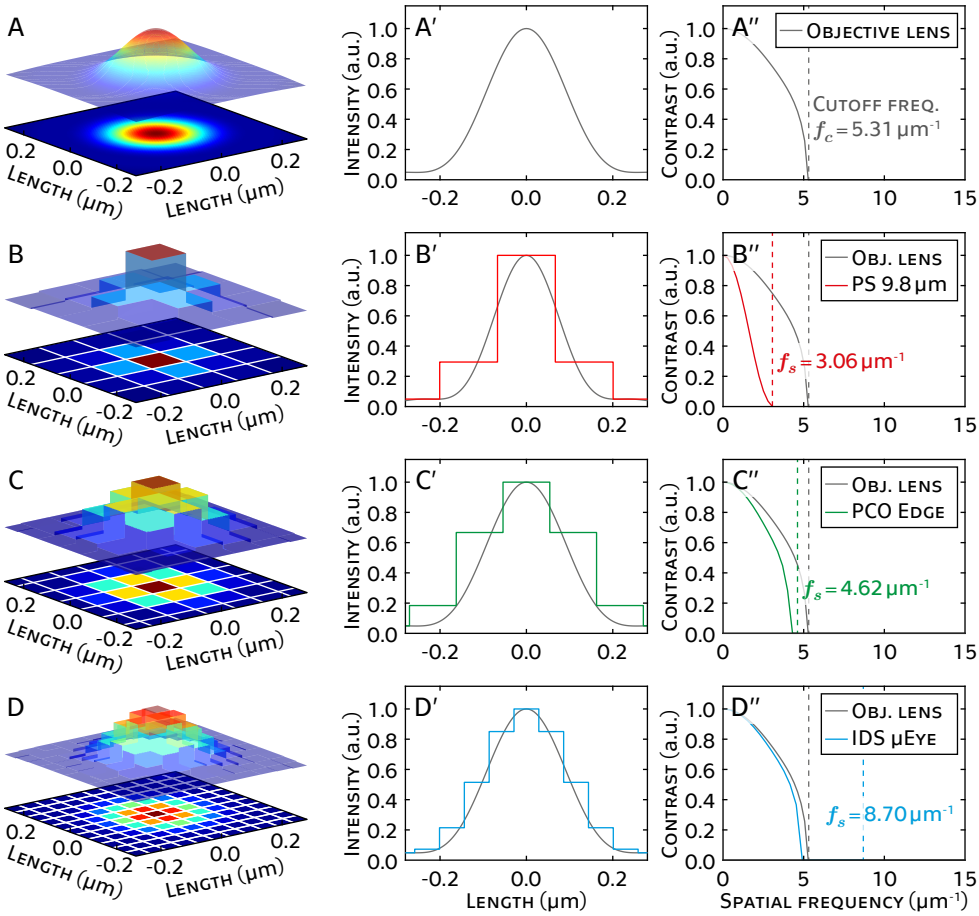

Figure 1.9: Digital imaging in microscopy demonstrating the impact of the Nyquist–Shannon sampling theorem. First column shows two- and three-dimensional representation of the point spread function (PSF). Second column with superscript (') shows the line profiles along the center of the PSF. Third column with the superscript (") shows the modulation transfer function of the second column. (A) Ideal PSF in high resolution close to the analogue signal of utilizing a typical objective lens (PlanApo 60×1.45) for the wavelength $\lambda = 546\,\text{nm}$.

frequency f_c) given by the objective lens. Thus, the physical size of one camera pixel must be at least two times smaller than the diffraction disk radius in the image plane of the objective lens[3]. For instance, using a $60\times/1.45$ objective lens with an emission wavelength $\lambda = 546\,\text{nm}$, cut-off frequency is equal to $f_c = 2\cdot 1.45/0.546 = 5.31\,\mu\text{m}^{-1}$, the sampling frequency must be equal to $f_s = 10.62\,\mu\text{m}^{-1}$. Considering the magnification $60\times$, the maximum camera pixel size equal to $60/f_s = 5.65\,\mu\text{m}$. The pixels in modern cameras used for biological imaging are usually smaller than $\sim 7\,\mu\text{m}$[52,53] which is sufficient in most of the SR microscopy applications.

Table 1.1 shows results of simulations of 12 possible digital microscope configurations resulting in the oversampling (green values), sufficient sampling for microscopy (orange values), and undersampling (red values) which is not sufficient in digital microscopy. Simulations were calculated for 2 objective lenses (60×1.45, and 100×1.50, see Table A.1), 2 fluorescence dyes (Atto 565, and Alexa Fluor 488), and three cameras (scientific camera PCO Edge 5.5[52], industrial camera IDS UI-3270CP[53], and theoretical model "Camera" using 9.8 µm pixels). Results from the first column of the Table 1.1 are graphically presented in the following Figure 1.9.

2

Super-resolution Microscopy

This chapter presents an overview of the most common super-resolution fluorescence microscopy techniques. The chapter focuses on the detailed explanation of the structured illumination microscopy (SIM) and the recent development on a low-cost and compact approach in SIM. Five freely available SIM datasets suitable for further software development of reconstruction and analysis tools are presented. Furthermore, a detailed description of the compact SIM system (fiberSIM) is major part of this chapter. Core findings presented in this chapter were published in Optics Express (2021)[A1], and GigaScience (2019, 2018)[A2,A3]. In order to explain fundamental principles of selected super-resolution techniques, Sections 2.1.1, 2.1.2, and 2.1.4 contain simulations with simplified demonstration images, e.g., "cameraman.tif", or synthetic image with individual emitters.

Contents

2.1 Super-resolution Microscopy

Super-resolution imaging in light microscopy is a powerful technique which extends the investigation of live biological samples to the level of nanostructures. Several methods are now available that increase the spatial resolution of fluorescence microscopy beyond the diffraction limit. These methods can be divided into four main categories. Single molecule localization microscopy (SMLM), super-resolution optical fluctuation imaging (SOFI)[8,9], stimulated emission depletion (STED) microscopy[11], and structured illumination microscopy (SIM). SMLM approach includes, e.g, stochastic optical reconstruction microscopy (STORM)[6,7], and photoactivated localization microscopy (PALM)[4,5]. Furthermore, super-resolution SIM (SR-SIM)[12], non-linear SIM (NL-SIM)[1313], optical sectioning SIM (OS-SIM)[15], or maximum a posteriori probability SIM (MAP-SIM)[54,55] methods have become popular for the investigation of live cell dynamics in the last decades. Despite many differences between these methods, fluorescence microscopy is a common and key element for super-resolution imaging. In live cell imaging, it has to be noted that in order to avoid artifacts using any of the SR microscopy method, the acquisition time should be shorter than the time it takes for the cell structure to move approximately one resolution length (the length equal to the diffraction limit of a microscope)[1]. This assumption limits the use of some SR methods for investigation of live cell dynamics. More details are discussed in the following sections.

2.1.1 Single Molecule Localization Microscopy (SMLM)

Single molecule localization microscopy (SMLM) offers the ability to obtain super-resolution microscopy images with a sub-diffraction-limit spatial resolution. The localization precision of SMLM is given by $s = \lambda/\mathrm{NA}$, with λ being the fluorescence emission wavelength and NA the numerical aperture of the detection objective lens. Current SMLM techniques can increase the resolving capability of an optical microscope up to ∼20 nm in lateral and ∼50 nm in axial dimension, more then 10-fold increase over the classical diffraction limit[1,4–6,56–58]. Stochastic switching individual fluorophores (blinking) enables to distinguish the single molecules to which the fluorophores are attached (see Fig. 2.1). To achieve a successful SMLM reconstruction, fluctuating emitters should fulfill the following conditions: 1) Fluorescence markers should switch between two distinguishable states, e.g., a bright/*on* state and a dark/*off* state. 2) Each emitter switches between these two states repeatedly and in a stochastic manner. 3) The point spread function of each emitter has to cover several camera pixels (to fulfill the Nyquist–Shannon sampling theorem, see Section *1.3.2: Digital Microscopy*). If a sufficient number of the photons are collected (roughly the square root of the number of photons detected), the position of an individual emitter can be determined with high accuracy. However, localization accuracy of SMLM techniques does not directly relate to the imaging resolution as multiple emitters in close proximity might be difficult to

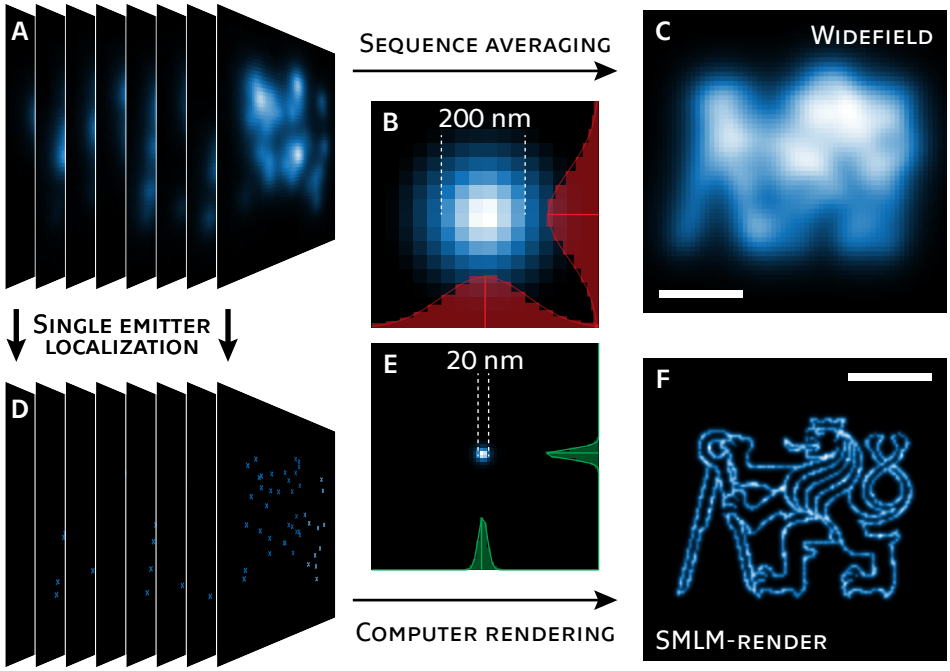

Figure 2.1: Demonstration of the SMLM image reconstruction. Single fluorescent emitters (D) are localized in each image from the sequence (typically thousands of frames) of individual stochastically blinking fluorophores (A). (B) Point spread function PSF of the diffraction limited detection objective lens. (C) Widefield image can be constructed by averaging the whole raw SMLM sequence (A) over time. (E) PSF model based on the localization precision used for the final SMLM image render (F). The scale bars in (C) and (F) are 0.5 µm.

distinguish.

Methods based on highly precise detection and localization of single molecules exploit the stochastic subset of fluorophores activated during the short acquisition of one image frame. The diffraction limited point spread functions of individual molecules appear isolated, and their positions can be localized with high accuracy. The final super-resolution image is composed of the individual molecule localizations from thousands of images in the SMLM sequence. The ability to fit the point spread function of a single emitting molecule gives its precise coordinates[16,57]. However, it has to be noted that the point spread function typically varies over the field of view[A10] which might bring some uncertainty during the PSF fitting in the SMLM reconstruction process.

SMLM methods such as photoactivated localization microscopy (PALM, SR imaging method reported in 2006)[4–6] and stochastic optical reconstruction microscopy (STORM, also published in 2006)[11,56,59] allow to explore sub-nanometer structures in a variety of

biological systems. That significantly helped with, e.g., the discovery of the periodic membrane skeleton structure in neurons[60], the structure of DNA at the end of the linear chromosome[61], the elucidation of the molecular organization of chemical synapses in the brain[62], or the architecture of the nuclear pore complex[63]. These examples clearly prove the importance and great potential of the SR techniques extending the spatial resolution of light microscopy.

Despite the significant improvement in the spatial resolution of an optical microscope, SMLM also brings disadvantages. The complex image reconstruction process requires a careful consideration of falsely localized individual emitters due to high label density or incorrect set of photoswitching rates. Furthermore, requirements on specifically photoswitchable or activatable fluorescent labels (for PALM) and special buffer conditions to make conventional dyes blinking (for STORM) are demanded for successful SMLM imaging. To reconstruct a single SMLM image, it is necessary to acquire thousands of camera frames. The overall length of an acquisition time then restricts the applicability of SMLM for live-cell imaging.

2.1.2 Super-resolution Optical Fluctuation Imaging (SOFI)

Similar to the SMLM, super-resolution optical fluctuation imaging (SOFI) is SR technique based on the nonlinear statistical analysis of temporal fluorescence fluctuation (blinking). The single stochastically blinking molecule is spatio-temporally correlated with itself, but uncorrelated with neighboring signals. This allows one to calculate the temporal n^{th} order cumulant for each pixel time trace (see Fig. 2.2 for illustration). Cumulants are a statistical measure, similar to moments, used to describe a probability distribution. Higher-order cumulants are a measure for non-Gaussianity[8,64]. The final SOFI image is given by calculating of the temporal cumulants or spatio-temporal cross-cumulants[16,65]. Further, calculating of cross-cumulants creates a virtual pixel between two neighboring pixels, which leads to n-fold upsampling in the SOFI image. Determining of n^{th} order cumulant for each pixel brings the spatial resolution enhancement of factor $\sqrt{n}$ over the reconstructed image. Moreover, an n^{th} order cumulant does not contain information from lower orders which would degrade the resolution enhancement[6,8,64,66]. Combining SOFI with the SMLM processing method on the same dataset reveals more information about the sample structure and properties, which can be useful for identification of the characteristic artifacts for each method[A3].

Despite the potential to be faster than SMLM[67] with the high impact on the spatial resolution enhancement, common SOFI reconstruction still requires a sequence of blinking emitters in the range of thousands of frames. Therefore, SOFI technique is still limited for the investigation of nanostructures of fixed cells.

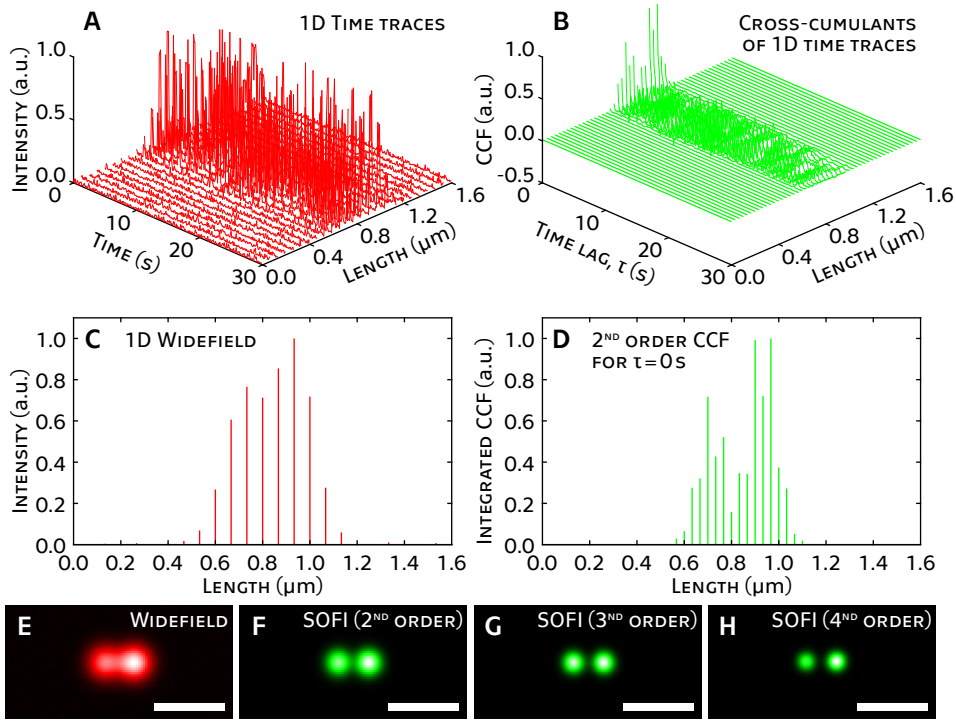

Figure 2.2: One dimensional explanation of super-resolution optical fluctuation imaging SOFI. (A) Time traces taken from 1D line of the input image sequence of two blinking emitters. Widefield image (E) and it's line profile (C) are constructed as the average of the input image sequence. (B) 2nd order cross-cumulants calculated from the intensity time traces for all time lags and it's zero-time lag ($\tau = 0$) (D). Note that the 2nd order cross-cumulant is equivalent to cross-correlation. (F)-(H) The resulting SOFI images up to 4th order. Time traces are 4-fold down-sampled for better visualization. The figure was generated with the simulation codes published in PLOS One vol. 11(9)[66]. The scale bars in (E)-(H) are 500 nm.

2.1.3 Stimulated Emission Depletion Microscopy (STED)

Stimulated emission depletion STED[50] microscopy is based on the reducing the extend of the PSF of the excitation beam by a depletion laser beam (hereinafter STED beam) with a ring profile (see Fig. 2.4B). The ring shape of the STED beam is created by the vortex phase mask in the depletion laser beam path. The STED beam suppresses the spontaneous fluorescence emission of the fluorophores except those in the middle of the STED ring-shaped beam. This results in a dramatic reduction in the volume of excited fluorophores close to targeting individual molecules in a live cell sample. It should be noted that synchronized pulse lasers have to be used to achieve proper depletion. The probability of depletion of the excitation state of the fluorophore by the stimulated

emission increases with the intensity of the STED beam. The final diameter of the effective fluorescence emission, which is related to the resolving capability of the STED microscope is given by[2,68]

$$d_{\mathrm{STED}} \approx \frac{d}{\sqrt{1 + \frac{I_{max}}{I_{sat}}}}, \tag{2.1}$$

where d is the resolution limit of the microscope objective lens, I_{max} is the intensity of the excitation laser beam in the middle of the depletion ring (typically 0.1-1 GW/cm^2), and I_{sat} is the intensity of the depletion beam. This is the intensity when the stimulated emission reduces the quantum efficiency of the spontaneous fluorescence by half[68]. This shows that the STED microscope can theoretically achieve any resolving capability assuming the high power depletion laser. In practice, the final resolving capability of STED is limited to the nanometer scale by many factors, such as aberrations of the microscope optical components, refraction of the light in the biological sample, or photostability of fluorophores. Therefore, the lateral resolution of the STED microscope is typically in the range of 30-80 nm.

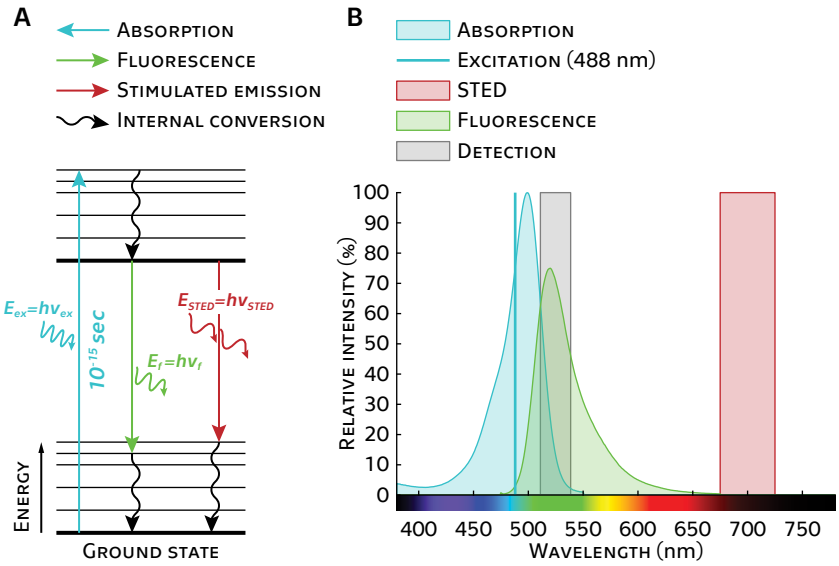

Figure 2.3: Simplified Jablonski diagram for describing the stimulated emission depletion microscopy. (A) After initial stimulated absorption (cyan wave arrow) a fluorophore is excited from the ground state to the excited state (vertical arrow up). After internal conversion, fluorescence is spontaneously emitted (green wave arrow). Fluorescence can be silenced by applying stimulated emission. After the fluorophore excitation, far red-shifted depletion light (red wave arrow) can stimulate the energy decay into the electronic ground state (red arrow down) and a replica of the depletion light is emitted. Stimulated depletion can thus deplete spontaneous fluorescence when present. (B) Spectrum diagram of a fluorescence dye Alexa Fluor 488.

A successful STED reconstruction requires very precise temporal synchronization of the two laser sources with different wavelengths. To reach a suitable emission depletion, a short depletion pulse (with λ_{dep}) must follow the excitation pulse (with λ_{ex}) with the temporal precision of 10^{-15} seconds (see Fig. 2.3, where Jablonski diagram shows the process of the stimulated emission depletion). Furthermore, because STED is a scanning microscopy technique, the synchronization of the two scanning mirrors (see Fig. 2.4 has to be ensured. Once these two conditions are secured, STED microscopy becomes a powerful SR technique which allows us to observe the nanostructures of cells. The temporal resolution of STED varies in the range of seconds to minutes, depending on the size of the scanned area. Therefore, this technique is not suitable for examination of the dynamics of live cells.

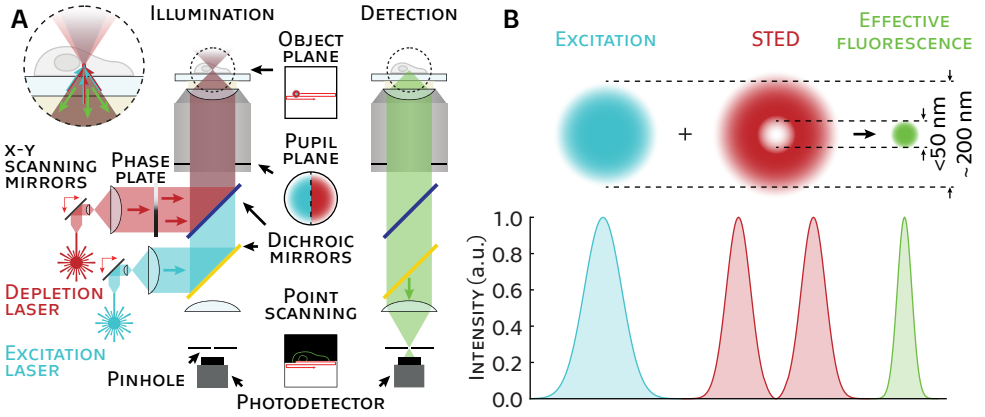

Figure 2.4: Schematics of the STED microscope with an illustration of the effective fluorescence beam shaping. (A) Principle of the STED microscope. Two temporally synchronized laser sources illuminate a small spot of the sample (object plane) by changing the lateral position with two synchronized x-y scanning mirrors. So called "donut shape" STED beam (red) is shaped by the vortex phase mask in the depletion laser beam path. Stimulated fluorescence emission (green) is collected by the objective lens and the light transmitted through the dichroic mirrors is detected on the photodetector. Final SR image is then reconstructed point-by-point in a computer. (B) Formation of the effective fluorescence spot (green) by combination of the excitation (blue) and depletion (red) beam profiles.[a]

[a]Figure was adapted with permission from "Super-resolution microscopy demystified," by Schermelleh, L., Ferrand, A., Huser, T. et al. Nat. Cell Biol. 21(1), p. 73. Copyright 2019 by Springer Nature Limited.

2.1.4 Structured Illumination Microscopy (SIM)

Super-resolution structured illumination microscopy (SR-SIM) is one of the most common means of achieving a spatial resolution beyond the diffraction limit with fluorescence microscopy. In contrast to the SMLM, or SOFI techniques, SR-SIM doubles the spatial resolution of optical microscopy, which is, however, readily sufficient to visualize cellular organelles and their substructures well below 200 nm. Moreover, SR-SIM provides high-speed reconstruction well suitable for living cell imaging[12,14,69–71]. In addition to this, SR-SIM is a widefield imaging method, making it highly efficient in the use of the available photon budget, while minimizing photoinduced effects, which can be detrimental to the sample health. Furthermore, rapid imaging of individual cells over extended periods of time with multiple color channels has been demonstrated using this SR technique[37,72]. Even high speed SIM systems utilizing real-time image reconstruction have been developed[71,73,74]. These implementations allow biologists to examine living cells and their dynamics at super-resolution, even during data acquisition.

In the last decade SIM has rapidly gained in popularity. Depending on the optical setup and data processing method used, SIM can achieve effective optical sectioning (OS-SIM[15]), which greatly reduces out-of-focus light. This effect is well known in laser scanning confocal fluorescence microscopy. SIM also performs imaging beyond the diffraction limit in fluorescence microscopy. The most common implementation[14] of the super-resolution SIM (SR-SIM[12,75]) uses laser illumination to create a high-frequency interference fringe pattern (close to or at the resolution limit of the microscope) to illuminate the sample. Sample information with details beyond the diffraction limit of the microscope used is aliased into the acquired images. By acquiring multiple images with shifting illumination patterns, a high-resolution image can be reconstructed[12,75]. Two-dimensional SR-SIM enables a two-fold resolution improvement in the lateral dimension[12,69,75,76]. If a three-dimensional (3D) illumination pattern is used, a two-fold resolution improvement can also be realized in the axial direction[14,72,77]. SIM is a powerful super-resolution method for imaging live cells because it does not require high illumination powers, can work with most dyes and fluorescent proteins, uses efficient widefield detection, and can achieve high imaging rates (close to real-time). SIM has been demonstrated in several applications, including two-dimensional (2D)[69,76] and 3D imaging[77,78].

As interest in super-resolution imaging has increased, several alternative approaches for SIM have been introduced that use various kinds of patterned illumination[79–83]. For example, in multifocal structured illumination microscopy[79], a 2D array of focused laser spots is scanned across a sample, and subsequent image processing is used to achieve an image with improved resolution. Structured illumination methods have also been combined with light sheet excitation, a method suitable for imaging live cells[32,84–87]. In addition to new illumination schemes, alternative data processing methods have also been introduced[54,88–93]. For example, a 2D method for SIM reconstruction based on Bayesian estimation[89] has been introduced. Bayesian reconstruction methods in SIM have several potential advantages and can achieve a performance comparable to

traditional SIM methods[90]. The maximum a posteriori probability SIM (MAP-SIM)[54], a method based on reconstruction of the SIM data using a Bayesian framework, also allows 3D super-resolution imaging. Image restoration approaches are useful when working with low signal levels in SIM[94] and have been reviewed[95].

Currently, most 2D and 3D SR-SIM realizations are based on utilizing the interference pattern generated by projecting the $\pm 1^{\text{st}}$ and 0^{th} (in the 3D case) diffraction orders of a diffraction grating into the objective lens focal plane. 2-beam interference patterns are typically utilized to achieve 2D resolution enhancement in the lateral direction, while 3-beam interference patterns allow for 3D resolution enhancement[14,70]. Taking into account that SR-SIM is based on exciting fluorescence by interference fringes, then other means of creating and rapidly changing such patterns can be envisioned. Alternative ways of creating stable interference patterns, e.g., by laser beam interferometry, could also be devised and have been used in the past. Interfering waves along the x- and y-direction created by deflecting laser beams at high incidence angles via a prism-system to the focus plane of an inverted microscope were used to realize one of the first SIM systems[96]. Current implementations of SR-SIM devices are, however, rather bulky systems. Two major limiting factors for high speed acquisition can be identified. 1) In SR-SIM systems based on diffraction optics, only a fraction of the original laser light is delivered to the sample. This limits high speed image acquisition because the fluorescence is not excited efficiently enough to result in sufficient signal strength at low exposure times. 2) The rate at which some electro-optic devices, such as liquid crystal-based spatial light modulators[71,97,98], can switch between patterns is significantly below a camera frame rate.

Concept of Structured Illumination Microscopy

The SR-SIM method uses a harmonic striped illumination pattern to copy the high frequency content to lower frequencies where it can be recovered. The harmonic pattern illuminates a fluorescent labeled specimen with the high spatial frequency close to or at the resolution limit (cut-off frequency) of the microscope. The high frequency information is encoded into the observed image through aliasing (see Fig. 2.5E). The observed sample is illuminated with a set of illumination patterns with different spatial shifts and orientations. Three orientations and three phase shifts are used in traditional 2D SIM. The illumination pattern can be described as[99]

$$I_{\theta,n}(\boldsymbol{r}) = 1 - \alpha \cos(2\pi \boldsymbol{p}_\theta \boldsymbol{r} + \varphi_n), \tag{2.2}$$

where $\boldsymbol{r} = (x, y)$ is a spatial vector, α is the modulation factor, $\boldsymbol{p}_\theta = (p \cdot \cos\theta, p \cdot \sin\theta)$ is the illumination frequency vector oriented with angle θ and φ_n is n^{th} phase shift $(n = 1 \dots N)$. The phase shifts for one orientation are chosen so that the sum of all illumination patterns cover the full sample (the step of the phase shift is π/N). The mathematical representation of the n^{th} acquired image $D_{\theta,n}(\boldsymbol{r})$ is

$$D_{\theta,n}(\boldsymbol{r}) = \Big[S(\boldsymbol{r}) \cdot I_{\theta,n}(\boldsymbol{r}) \Big] \otimes H(\boldsymbol{r}) + N(\boldsymbol{r}), \tag{2.3}$$

where $S(\boldsymbol{r})$ and $I_n(\boldsymbol{r})$ are the observed specimen and harmonic illumination pattern, respectively. $H(\boldsymbol{r})$ is the point spread function (PSF) of the microscope optical system and $N(\boldsymbol{r})$ represents the additive camera noise, $\otimes$ is a convolution operator. The Fourier transform of the observed image is

$$\begin{aligned}\widetilde{D}_{\theta,n}(\boldsymbol{k}) &= \left[\widetilde{S}(\boldsymbol{k}) \otimes \widetilde{I}_{\theta,n}(\boldsymbol{k})\right] \cdot \widetilde{H}(\boldsymbol{k}) + \widetilde{N}(\boldsymbol{k}) \\ &= [\widetilde{S}(\boldsymbol{k}) + \frac{\alpha}{2}\widetilde{S}(\boldsymbol{k} - \boldsymbol{p}_\theta)e^{+2j\pi\varphi_n} \\ &\quad + \frac{\alpha}{2}\widetilde{S}(\boldsymbol{k} + \boldsymbol{p}_\theta)e^{-2j\pi\varphi_n}\Big] \cdot \widetilde{H}(\boldsymbol{k}) + \widetilde{N}(\boldsymbol{k}), \end{aligned} \tag{2.4}$$

where $\widetilde{S}(\boldsymbol{k})$ and $\widetilde{I}_{\theta,n}(\boldsymbol{k})$ are Fourier transforms of the specimen and illumination pattern, respectively. The optical transfer function (OTF) is represented by $\widetilde{H}(\boldsymbol{k})$.

Equation (2.4) shows that $\widetilde{D}_{\theta,n}(\boldsymbol{k})$ is a combination of spectral components $\widetilde{S}(\boldsymbol{k})$ and $\widetilde{S}(\boldsymbol{k} \pm \boldsymbol{p}_\theta)$. Assuming that the pattern spatial frequency, orientation, and phase shift are known, the spectral components can be separated, shifted to their proper positions, and aligned together (see Fig. 2.5G).

SIM reconstruction is successful under two conditions. First, the OTF of an optical system is known or can be precisely measured. Second, the shape (spatial frequency, angle, and phase) of each illumination pattern is known. However, a drift of the specimen during image acquisition may distort the illumination pattern properties, and the pattern shape may vary in each image. The pattern distortion results in undesired image reconstruction artifacts and hampers the resolution enhancement in practice. Moreover, the high noise levels in the raw data may cause an improper shift of the spectral components, which degrade the super-resolved image[100].

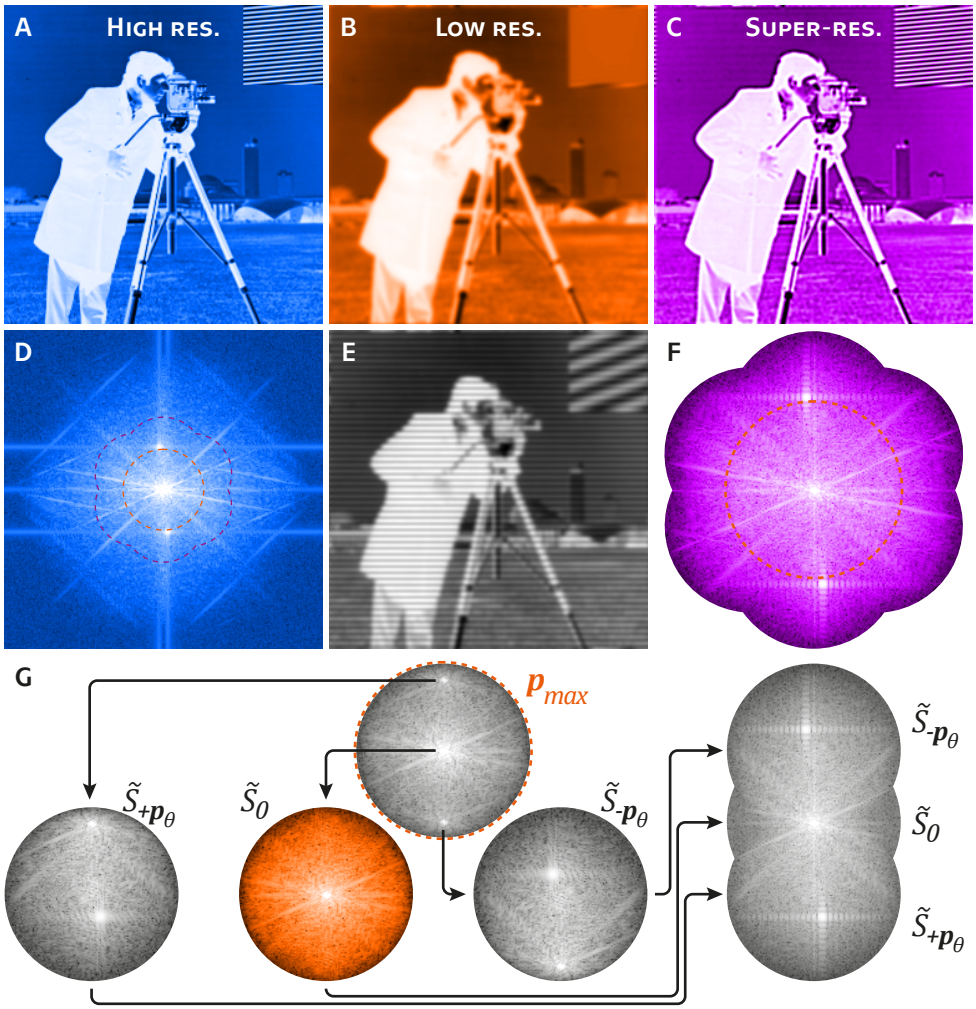

Figure 2.5: Simulation of structured illumination microscopy (SR-SIM) reconstruction. (A) A real sample with the high frequency content (HR). (B) Diffraction limited image (low resolution - LR) of (A). (C) Super-resolution (SR) image after SIM reconstruction. (D) Fourier transform of HR image (A). Orange and purple dashed lines represent the cut-off frequency of diffraction limited image (low resolution, $f_c = \boldsymbol{p}_{max}$) and reconstructed image (super-resolution), respectively. (E) Low resolution image illuminated with the striped pattern with the spatial frequency $\boldsymbol{p}_\theta$. (G) Fourier transform of observed image (E) and its decomposition into three spectral components ($\tilde{S}_{+\boldsymbol{p}_\theta}$, $\tilde{S}_0$, and $\tilde{S}_{-\boldsymbol{p}_\theta}$). Zero component ($\tilde{S}_0$) corresponds to the low resolution image (B). Aligning these three spectral components results in SR image with spatial resolution enhancement in one direction. (F) Fourier space of super-resolved image (C) where the spatial resolution is enhanced in three directions (30°, 90°, and 150°). Orange dashed line represents the LR cut-off frequency $f_c = \boldsymbol{p}_{max}$.[b]

[b] Testing image *cameraman.tif* has been used for illustration of the SIM reconstruction. To approximate the fluorescence image, the original image grayscale has been inverted.

2.2 Live Cell SR-SIM Imaging

Following section is mainly based on the article published in GigaScience (2019)[A2].

Complete raw and processed SIM datasets from several situations in cell biology studies are presented in this section. Both live and fixed mammalian cells as well as fixed tissues were imaged using an alternative SIM illumination approach based on FLCOS microdisplay[54,55,98]. Microscope setup uses either light-emitting diode (LED) or laser illumination and a fast ferroelectric liquid crystal-on-silicon (FLCOS) microdisplay, also known as a spatial light modulator (SLM), for SIM pattern definition. SLMs have seen use in SIM and related applications when high-speed imaging and flexibility in controlling the spatial and temporal properties of the illumination are priorities[69,76–78,86,97,98,101–105]. Data analysis was performed on images reconstructed with OS-SIM, SR-SIM, and MAP-SIM methods. All of the raw and processed data are available on GigaDB[A2], and can be reused for testing of new SIM algorithms or another analysis purposes. Analysis software (*SIMToolbox*[c]) is open source and freely available[55].

2.2.1 Preparation of Samples for Imaging

All cell lines used were maintained in Dulbecco's modified eagle medium supplemented with 10% fetal calf serum, 100 U/mL penicillin, 100 U/mL streptomycin, and L-glutamate (Invitrogen) at 37° C and 100% humidity. Cell lines used for this study included U2-OS (human bone sarcoma, RRID:CVCL 0042), A431 (human skin carcinoma, RRID:CVCL 0037), and HEP-G2 (human liver carcinoma, RRID:CVCL 0027).

SIM data 1, Fig. 2.8: U2-OS cells expressing lysosome-associated membrane protein 1 labeled with green fluorescent protein (LAMP1-GFP) were grown in Petri dishes with coverslip bottoms (MatTek, USA) for 24 hours, then imaged in full medium at room temperature. In this experiment, microscopy system 1 (Olympus IX71, Table 2.2) was used.

SIM data 2, Fig. 2.9: A431 cells were grown on #1.5H coverslips (Marienfeld, Germany) for 48 hours in normal medium. The cells were washed once with phosphate-buffered saline (PBS), pH 7.4, and then treated the cells with 5 µ DiI-C16 (Molecular Probes, USA) in PBS at room temperature for 5 minutes. This probe is lipid modified with a fluorescent dye that inserts into the plasma membrane of live mammalian cells within a few minutes. Then the cells were washed twice with PBS, and imaged on the SIM system in fresh PBS at room temperature using a coverslip chamber (Biotech). In this experiment, microscopy system 3 (Leica DMi8, Table 2.2) was used.

[c] https://simtoolbox.github.io/

SIM data 3, Fig. 2.10: A prepared slide was acquired (AmScope, USA) that contained a sectioned rabbit testis stained with hematoxylin and eosin. In this experiment, microscopy system 3 (Leica DMi8, Table 2.2) was used.

SIM data 4, Fig. 2.11: HEP-G2 cells expressing Dendra2-histone 4[106] were grown on #1.5H coverslips for 24 hours, then fixed for 15 minutes at room temperature with 4% paraformaldehyde. Then the cells were permeabilized for 5 minutes at room temperature with 0.1% triton X-100, and washed with PBS. The actin cytoskeleton of the cells was then labeled for 1 hour at room temperature with 5 nM Atto 565 phalloidin, and washing the cells with PBS followed. Finally, the coverslips were mounted on clean slides using mowiol 4–88 (Honeywell Fluka, Germany). In this experiment, microscopy system 1 (Olympus IX71, Table 2.2) was used.

SIM data 5, Fig. 2.12: A prepared slide was acquired (Molecular Probes, USA) that contained bovine pulmonary endothelial (BPAE) cells stained with Alexa Fluor 488 phalloidin (to label the actin cytoskeleton) and Mitotracker CMXRos (to label mitochondria). In this experiment, microscopy system 2 (Olympus IX83, Table 2.2) was used. Table 2.1 summarizes the imaging parameters used for the different samples.

Table 2.1: Imaging parameters for the SR-SIM datasets.

Fig.	Sample	Label (structure)	Illumination	Exposure time	SIM system
2.8	U2-OS cells (live)	LAMP1-GFP (lysosomes and membrane)	LED 480 nm	25 ms	1
2.9	A431 cells (live)	DiI-C16 (membrane)	LED 530 nm	100 ms	3
2.10	Rabbit testis (fixed)	Hematoxylin and eosin (structural strain)	LED 530 nm	200 ms	3
2.11	Hep-G2 cells (fixed)	Dendra2-H4 (nucleus) Atto565-phalloidin (actin)	LED 480 nm LED 530 nm	500 ms	1
2.12	BPAE cells (fixed)	Alexa Fluor 488 phalloidin (actin) Mitotracker CMXRos (mitochondria)	Lumencor spectra-X 470 nm 550 nm	300 ms	2

2.2.2 Microscope Setup and Acquisition

Three custom-built SIM setups based on the same general design (Fig. 2.6)[54,55,98] were used for the data acquisition. These SIM systems were based on Olympus IX71, Olympus IX83, and Leica DMi8 microscopes coupled with sCMOS cameras (Andor, Northern Ireland) under the control of the IQ3 software (Andor, Northern Ireland). The parameters of the different microscope setups are shown in Table 2.2. In each microscope setup, the illumination patterns are produced by high-speed FLCOS microdisplay (SXGA-3DM, Forth Dimension Displays, 13.6 µm pixel pitch). This particular FLCOS microdisplay has been used previously in SIM[55,73,77,78,86,90,98,107–109] and in other optical sectioning systems such as programmable array microscopy[101,104,110]. The display is illuminated by a custom-built, three-channel LED system based on high-power LEDs (PT-54 or PT-120 with DK-114N or DK-136M controller; Luminous Devices) with emission maxima at 460 nm, 525 nm, and 623 nm. The output of each LED is filtered with a band pass filter (Chroma, USA), and the three wavelengths are combined with appropriate dichroic mirrors (Chroma, USA). The light is then vertically polarized with a linear polarizer (Edmund Optics, Ltd, UK). The microdisplay is imaged into the microscope using an external tube lens (Table 2.2) and polarizing beam splitter cube

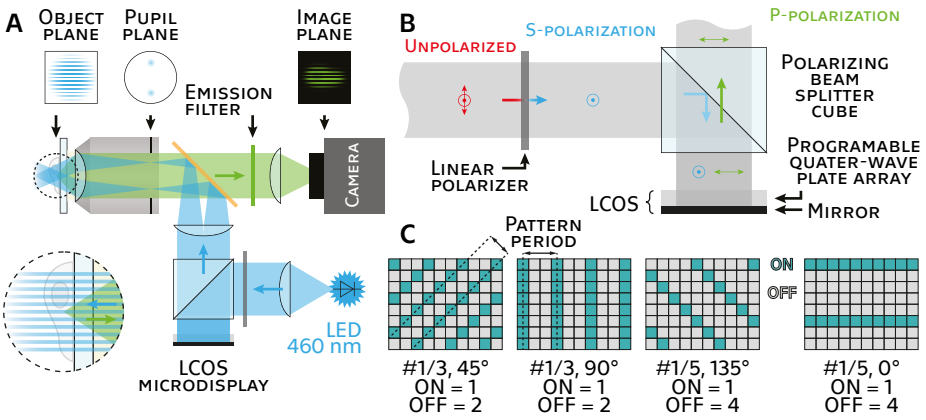

Figure 2.6: Illustration of the ferroelectric liquid crystal-on-silicon (FLCOS) based SIM setup. (A) High power LED illuminates the FLCOS microdisplay where the desired illumination pattern is generated (C). Pattern is then projected on the sample through the polarizing beam splitter, illumination tube lens, dichroic mirror, and objective lens. Emission light from the sample is then collected with the same objective lens and focused on the camera chip with the tube lens. Blue and green paths represent excitation and emission, respectively. (B) Detailed view on the polarizing beam splitter and LCOS (horizontally reflected in comparison with (A)). S-polarized light incident on the LCOS changes the polarization after the reflection to P-polarization which is transmitted through the polarizing beam splitter. This approach minimizes the power losses in comparison with common spatial light modulators (SLM).

Table 2.2: Parameters of the SR-SIM microscope systems.

Setup	Microscope	Obejctive	Andor sCMOS camera	Illumination tube lens focal length
1	Olympus IX71	100×/1.4 UPlanSApo	Neo 5.5	180 mm
2	Olympus IX83	100×/1.3 UPlanFLN	Zyla 4.2+	180 mm
3	Leica DMi8	100×/1.47 HCX PlApo TIRF	Zyla 4.2+	200 mm

(Thorlabs, Inc., USA). With any of the setups and when using a 100× objective lens, single microdisplay pixels are imaged into the sample with a nominal size of 136 nm, thus as diffraction-limited spots. This is important for achieving result with the highest resolution[98]. A Spectra-X light source (Lumencor, USA) was used in one experiment (Fig. 2.12).

The LCOS microdisplay brings the advantage of creating any desired illumination pattern (see Fig. 2.6C). In the following experiments, the illumination masks consist of line grids of different orientations (0°, 90°, 45°, and 135°). The lines are 1 microdisplay pixel thick (diffraction limited in the sample when using a 100× objective lens) with

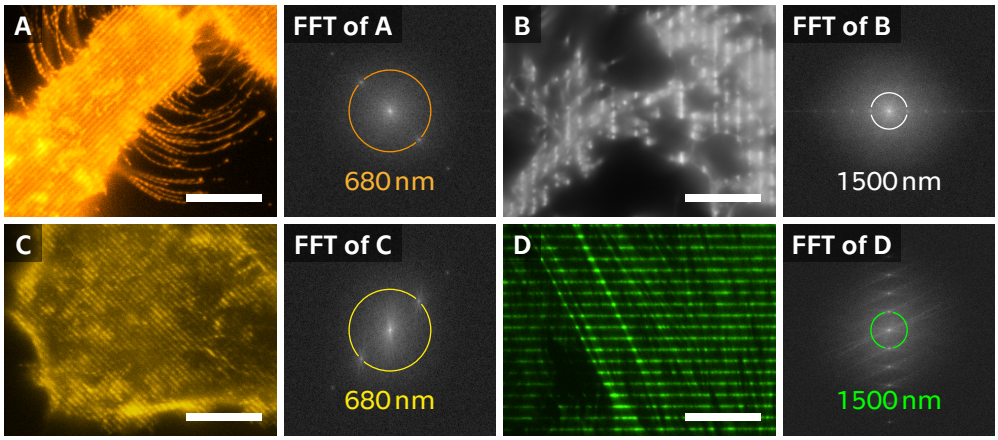

Figure 2.7: Example of the raw SIM data used in the imaging tissues and cells beyond the diffraction limit with structured illumination microscopy and Bayesian image reconstruction. (A), (B), (C), and (D) show the SIM illumination pattern in one of the four angles used. (FFT of A, B, C, and D) show the fast Fourier transforms of the illumination patterns over the cell or tissue sample. Color rings in each FFT represent the spatial frequency of the first harmonic of the illumination pattern. The scale bars are 10 µm.

a gap of "OFF" pixels in between. The illumination line grid is shifted by one pixel between each image acquisition to obtain a shifted illumination mask. The shift between each image is constant, and the sum of all illumination masks resulted in homogenous illumination. The presented optical setup, in which an incoherently illuminated microdisplay is imaged into the sample with highly corrected microscope optics, results in much more stable SIM illumination parameters compared to conventional SIM in which the illumination pattern is created by laser interference. The unique spatial calibration method is used to determine the position of the patterned illumination in the sample with very high accuracy[98]. This is a spatial domain process and does not rely on the fitting of data to a model except for the assumption that the imaging is linear and shift invariant.

2.2.3 Data Processing and Imaging Cells and Tissues

All presented data were processed using *SIMToolbox*, an open-source, user-friendly, and freely available program that our group developed for processing SIM data[55]. *SIMToolbox*, sample data, and complete documentation are freely available at the website: simtoolbox.github.io. *SIMToolbox* is capable of OS-SIM[15,98], SR-SIM[12,75], and MAP-SIM[54] methods. Additional details about these methods can be found in the Appendix B.

To demonstrate the utility of the presented SIM approach in imaging live cells, U2-OS cells that had been transfected with LAMP1-GFP were imaged. LAMP1 is a highly glycosylated protein that is found on the surface of lysosomes and in the plasma membrane[59]. Figure 2.8 shows Widefield, OS-SIM, and MAP-SIM images of U2-OS cells expressing LAMP1-GFP and the fast Fourier transform (FFT) of each image. The dotted circles in Fig. 2.8D–F show the approximate limit of the resolution in each image.

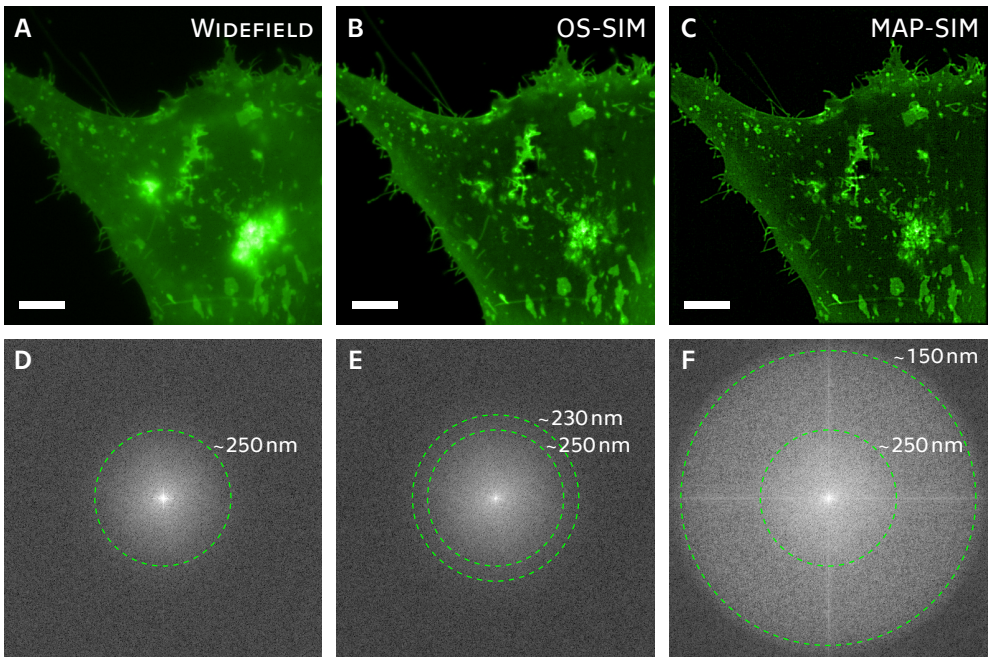

Figure 2.8: Imaging live U2-OS cells beyond the diffraction limit with MAP-SIM. U2-OS cells expressing LAMP1-GFP were imaged using the LCOS-based SIM system. Subsequent processing using OS-SIM or MAP-SIM methods. (A) Widefield, (B) OS-SIM, (C) MAP-SIM, (D) FFT of Widefield, (E) FFT of OS-SIM, and (F) FFT of MAP-SIM. The images were individually scaled for presentation. The dotted circular lines indicate the approximate resolution achieved in each image according to analysis of the FFT. The scale bars are 10 µm.

In addition to lysosomal expression, LAMP1-GFP is also present in high concentrations in the plasma membrane of U2-OS cells.

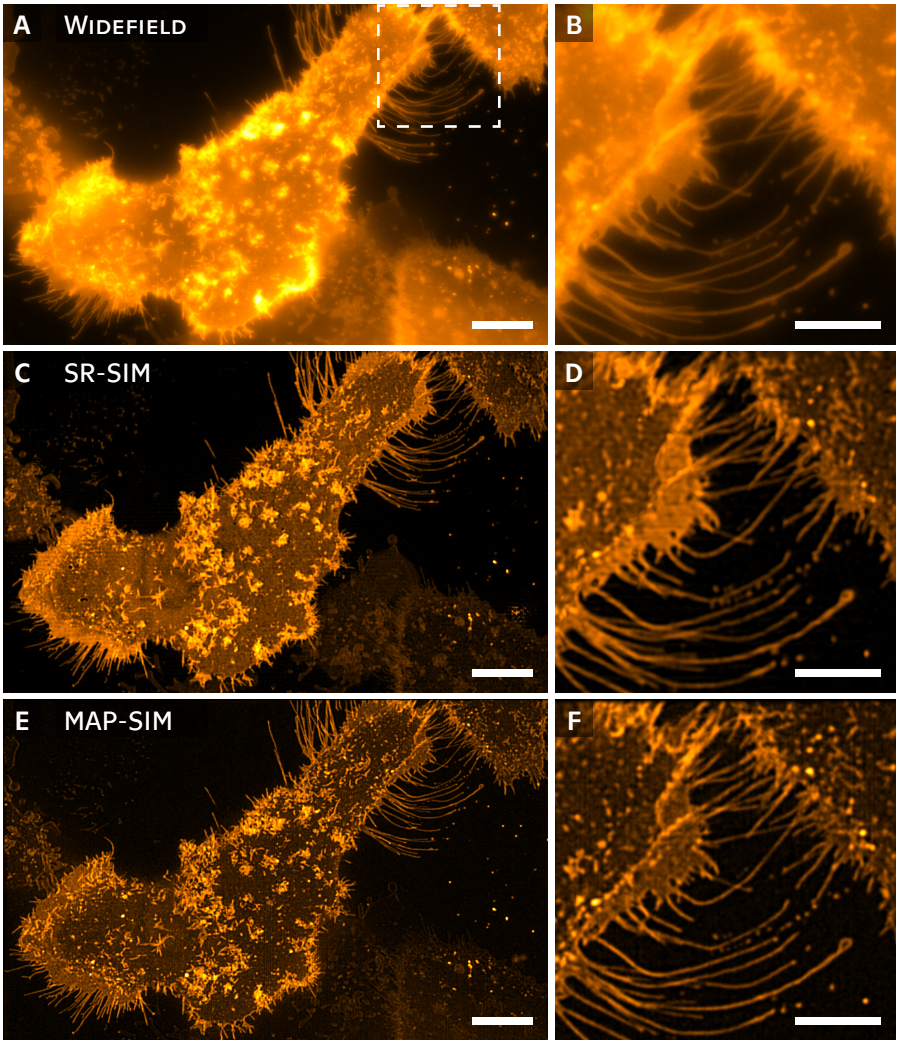

Figure 2.9: Imaging live A431 cells beyond the diffraction limit with SIM. A431 cells labeled with DiI-C16 were imaged using the LCOS-based SIM system. Subsequent processing using SR-SIM or MAP-SIM methods. (A) Widefield, (C) SR-SIM, (E) MAP-SIM. (B), (D), and (F) each show a zoom-in of the region indicated in (A). The images were individually scaled for visualization purposes. Each is a maximum intensity projection of 3 Z positions. The scale bars in (A), (C), and (E) are 10 µm. The scale bars in detailed ROIs (B), (D), and (F) are 5 µm.

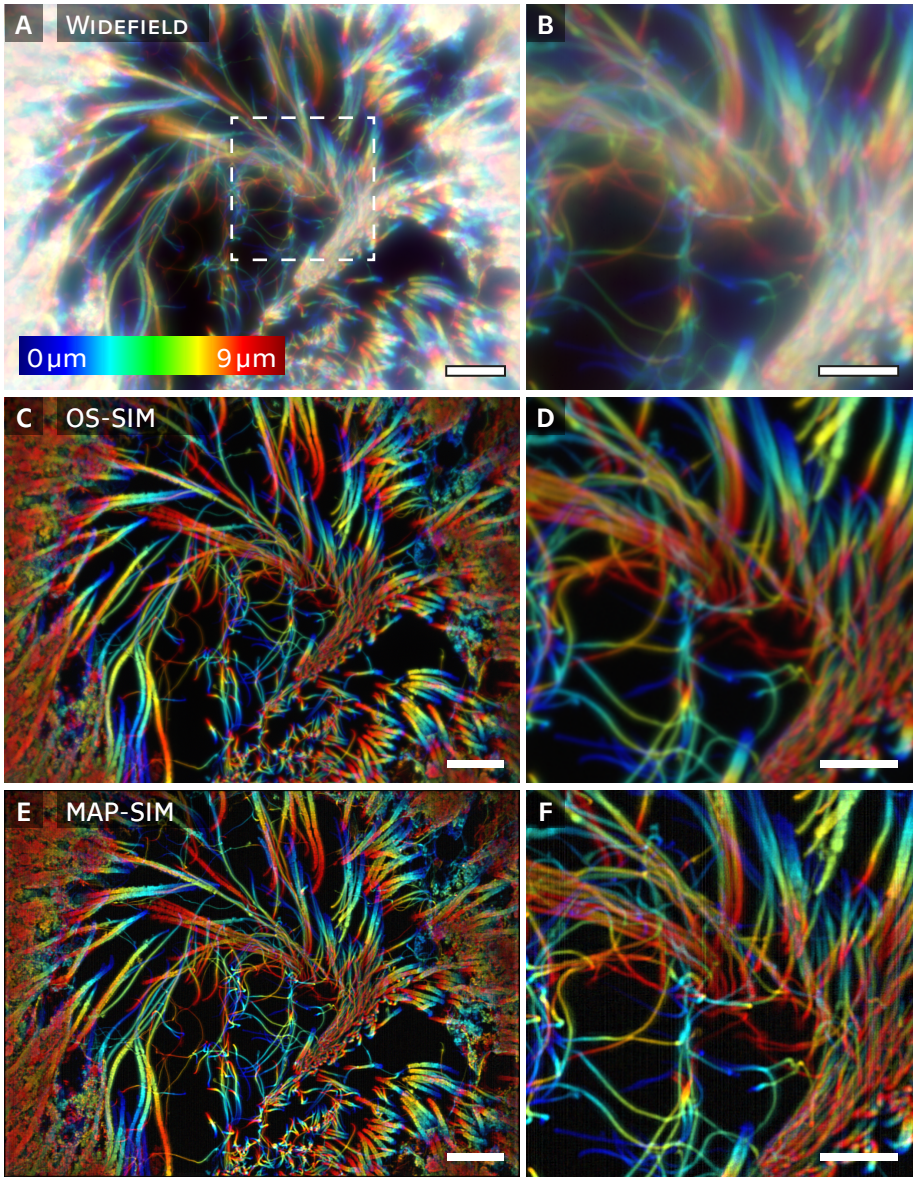

Figure 2.10: Volumetric imaging of animal tissues using the LCOS-based SIM system and subsequent processing of OS-SIM, and MAP-SIM reconstruction. All subfigures display a resulting volume projection with color-coded depth in range from 0 µm to 9 µm. Seminiferous tubule of the rabbit stained with hematoxylin and eosin. (A), (C), and (E) Widefield, OS-SIM, and MAP-SIM reconstruction. (B), (D), and (F) show a zoom-in of the region indicated in (A). The images were individually scaled for visualization purposes. The scale bars in (A), (C), and (E) are 10 µm. The scale bars in detailed ROIs (B), (D), and (F) are 5 µm.

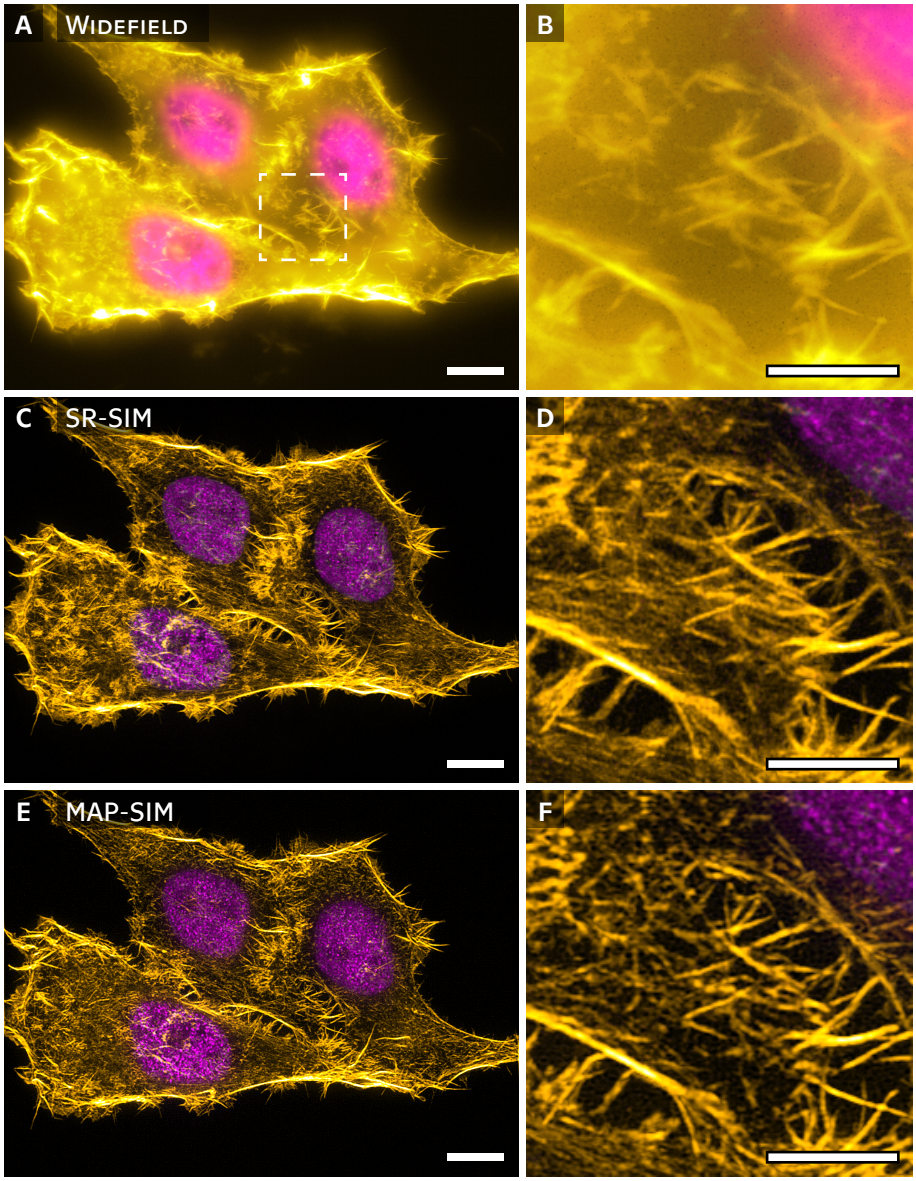

Figure 2.11: Imaging of fixed HEP-G2 cells expressing Dendra2-H4 (nucleus) labeled with Atto-532 phalloidin (green). (A), (C), and (E) Widefield, OS-SIM, and MAP-SIM reconstruction. (B), (D), and (F) show a zoom-in of the region indicated in (A). The images were individually scaled for visualization purposes. Each is a maximum intensity projection of 22 z-positions. The scale bars in (A), (C), and (E) are 10 µm. The scale bars in detailed ROIs (B), (D), and (F) are 5 µm.

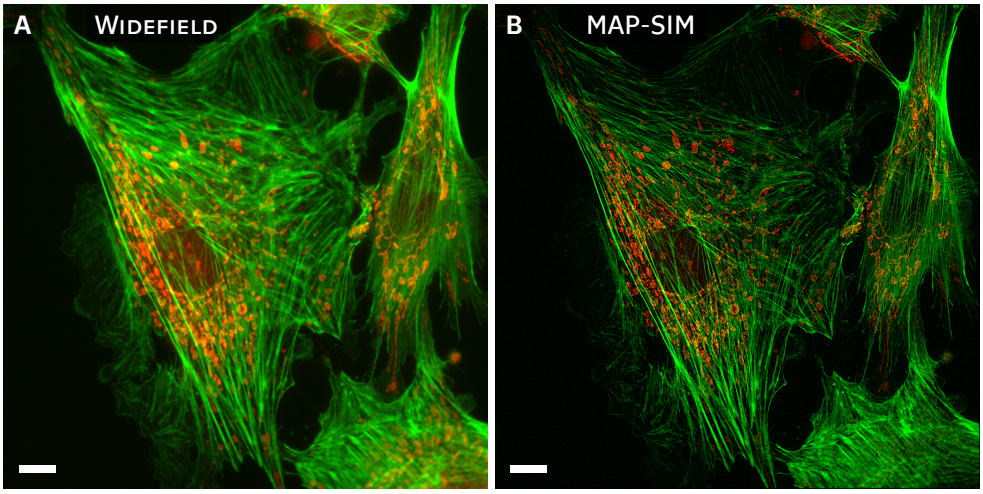

Figure 2.12: 2D SIM imaging of fixed BPAE cells labeled with Alexa 488-phalloidin (actin) and mitotracker CMXRos (mitochondria). (A), and (B) display Widefield, and MAP-SIM, respectively. The scale bars are 10 µm.

SIM results sometimes suffer from artifacts related to the illumination pattern. The artifacts, which can be severe and are a cause for concern, can be due to several factors, including illumination pattern phase instability and pattern distortion because of refractive index mismatch between the sample and the immersion fluid. Presented MAP-SIM results do not suffer from detectable patterned artifacts (Fig. 2.8C), and the Fourier transform of the MAP-SIM result is free of noticeable spurious peaks (Fig. 2.8F). This can be attributed to several factors, primarily the use of incoherent illumination together with an FLCOS microdisplay for the generation of illumination patterns. This, combined with precise synchronization of the SIM system, helps eliminate patterned artifacts. Additional artifacts in SIM images can arise due to the detector. In sCMOS cameras like the one used in this experiment, each pixel reads out through its own amplifier and, as such, each pixel exhibits a different gain. While very minor, such artifacts can be corrected using a variance stabilization method as has been introduced for single-molecule localization microscopy[111].

There are several other advantages to use incoherent illumination in SIM, including removing the need for a pupil plane mask to block undesired diffraction orders. Also, incoherent imaging of a microdisplay for pattern formation means that the pattern spatial frequency in the sample plane does not depend on the wavelength of the light that is used. On the other hand, in incoherent illumination, the contrast of the illumination pattern decreases with increasing spatial frequency according to the incoherent optical transfer function[112]. In coherent illumination SIM[12,14,75], the coherent optical transfer function applies[112], and so the pattern contrast does not decrease with increasing spatial frequency. This means that coherent illumination SIM can more efficiently mix high-resolution information from outside the frequency limit into the detection pass-band of the microscope, thereby potentially achieving the resolution enhancement

factor of 2.

The FLCOS microdisplay (and vendor-supplied microdisplay-timing program) can display an illumination pattern and switch to the next pattern in the sequence in 1.14 ms, allowing unprocessed SIM images to be acquired at rates of approximately 875 Hz. However, such rapid imaging is not useful due to short exposure time (low SNR) leading to the reconstructed SIM images of poor quality. Specifying the fastest possible acquisition rate is inadequate without consideration of the resolution and SNR of the results. Resolution analysis shown in Section *3.3.3: Power Spectral Density Analysis Results* uses measured quantities to evaluate SIM results. This analysis thereby helps to make realistic conclusions about imaging speeds (see also Appendix Fig. A.4).

2.3 fiberSIM: Highly Compact SR-SIM Microscope Based on Fiber Optics

Following section is mainly based on the article published in Optics Express (2021)[A1].

A particular advantage of fiber-based interferometry is the significantly lower loss in excitation light, which is limited to the amount of light that can be coupled into a single-mode fiber. Just this advantage alone would allow one to readily set up SR-SIM systems with less expensive low power lasers. In addition, optical fibers readily provide high stability, and, thus, robustness, to interferometers. They also allow for easy and very flexible means of light delivery. Already in 2006, a standing-wave TIRF system using the fiber optics to deliver the laser beams to the objective lens has been introduced[113]. While more recently, 2-beam interferometry using optical fibers to create a SIM-type interference pattern in opposing light sheets has been presented[33].

2.3.1 fiberSIM Microscope Setup

In this section, the development and operation of a SR-SIM microscope based on all-fiber optic components is detailed. Single-mode fiber-optic 1×2 splitters are used to set up coherent light paths to generate 2D interference patterns at specific illumination angles. A microelectromechanical systems (MEMS) based fiber switch is used to rapidly switch between different illumination angles, while the piezoelectric crystal-controlled displacement of fiber collimators provides the phase shifting required for 2D SR-SIM image reconstruction. This results in extremely flexible, compact, and robust SR-SIM illumination optics. We demonstrate and analyze its ability to efficiently generate SR-SIM illumination patterns. We also demonstrate the performance of this system by imaging mono-layers of fluorescent beads and by analyzing the resulting images using global metrics for determining image resolution.

To realize presented SR-SIM setup based on all-fiber optic components, a diode-pumped solid state laser operating at a wavelength of 532 nm and a power of 30 mW is coupled into the input fiber of a 1×4 microelectromechanical systems (MEMS) single-mode fiber switch (Sercalo AG, Switzerland). This device is designed for highly reliable and rapid switching between 4 different output fibers. (Details about the actual switching speed of the device are discussed in the Section *2.3.3: Performance of the System*). Three of these output fibers are used for the SR-SIM system to select between three different angles under which the interference pattern is generated. Each one of the output fibers is connected to a 1×2 fiber splitter (Thorlabs, Inc., USA) and the ends of these fibers are then used to define a specific angle of illumination. Since the current implementation does not (yet) utilize polarization maintaining fibers, in-line fiber polarization controllers (Thorlabs, Inc., USA) are used to adjust the output

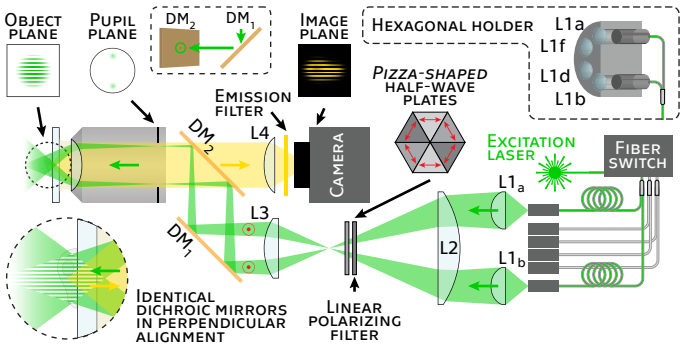

Figure 2.13: Schematics of the *fiberSIM* system. A hexagonal holder holds 6 fiber collimators in 60° intervals. A combination of two fiber collimators ($L1_a$, and $L1_b$) with a relative displacement of 180° are placed in equal distance from the central axis of the hexagonal holder. Each one of these two collimators focuses a laser beam to the back focal plane of a 60×/1.45 TIRFM objective lens (Olympus, Japan), resulting in a striped interference pattern at the object plane of the objective lens. Three pairs of the fiber collimators define the respective angles of illumination for the interference pattern. Lenses L2 and L3 form a telescope that changes the separation between two beams of each pair to accommodate the back focal plane of the objective lens. The polarization of each beam (red arrow) is rotated by *pizza-shaped* half-wave plates in between lenses L2 and L3. A pair of identical dichroic mirrors ensures that the polarization state of the excitation light is maintained. Rapid switching between pattern angles is performed by the fast MEMS fiber switch. Displacement along the axial axis of one collimator in a pair results in phase shifting of the illumination pattern in the object plane. Fluorescence emission is captured by the same objective lens and lens L4 focuses the fluorescence light to the CMOS camera chip.

polarization state and, thus, to control the output power of each fiber. The two branches of the 1×2 fiber splitter are placed opposite each other to form a pair (see Fig. 2.13), and each pair position is rotated by 60° with respect to each other. In total, six fiber outputs are mounted in a custom-made hexagonal fiber holder comprised of 6 collimation units housing a single lens for each fiber ($L1_a$-$L1_f$: $f = 25\,mm$).

Figure 2.13 shows an illustration of the all-fiber optic SR-SIM setup. Outfitting each fiber with its own individual collimating lens creates flexibility for focusing patterns with different opening angles to the back focal plane of the objective lens. This allows for free placement of the collimating holder relative to the microscope objective lens, enabling one to easily switch objective lenses based on the specific application. The physical dimensions of the collimating lenses set the minimum separation between the adjacent parallel beam pairs to 33 mm. The diameter of the back focal plane of the objective lens (Olympus, Japan) is ∼10 mm. Therefore, the separation between the beams is varied with a telescope (lenses L2: $f = 300\,mm$, and L3: $f = 50\,mm$). Suitable selection of telescope lenses, and thus the separation between the beams, allows us to easily change and adapt the pattern frequency of the 2-beam SIM microscope. The polarization state

for each beam pair is rotated by placing a linear polarizing filter and a *pizza-shaped* half-wave plate (Bolder Vision Optics, USA) between the telescope lenses. To separate the excitation light from the fluorescence signal and maintain the polarization of the excitation light, a pair of identical dichroic mirrors in the perpendicular arrangement is used[109,114]. In the perpendicular arrangement the dichroic mirrors are placed such that the first one reflects light within the plane of the optical table, while the second one reflects light upwards (perpendicular to the optical table). Fluorescence emission from the sample is collected by the same objective lens and the tube lens (L4: f = 200 mm) focuses the light to a CMOS camera chip.

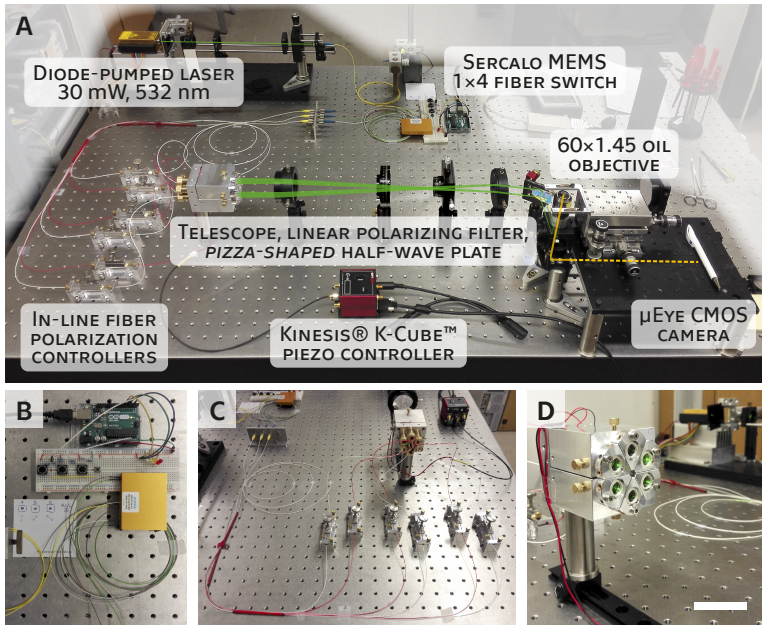

Figure 2.14: Photo of the *fiberSIM* microscope. A diode-pumped solid state laser is coupled into the input of a 1x4 MEMS fiber switch (B). Three output fibers are each connected to a 1x2 fiber splitter, respectively. The two fiber branches of each splitter are placed opposite each other to form a pair in the hexagonal holder (D). The polarization state in every one of the 6 single mode fibers is controlled by an in-line fiber polarization controller (C). Dedicated collimating lenses for each fiber focus the laser beams (green) to the back focal plane of the objective lens resulting in the interference pattern in the object plane. The separation between the beams is varied with a telescope. The polarization state for each beam pair is rotated by placing a linear polarizing filter and a *pizza-shaped* half-wave plate between the telescope lenses. The power of each individual beam is adjusted by the in-line fiber polarization controllers in combination with the linear polarizer. Fluorescence emission from a sample (yellow) is collected by the same objective lens and the tube lens focuses the light to the CMOS camera chip (a tube lens and CMOS camera are placed underneath the black base plate). Scale bar in (D) is 50 mm.

In this setup, inexpensive industry-grade CMOS camera (IDS, Germany) acquires the raw SIM images with a frame rate up to 41 fps. Photographs of the setup as well as the individual components are shown in Fig. 2.14. The theoretical line spacing of the interference pattern λ' can be defined as

$$\lambda' = \frac{\lambda_{ex} \cdot f}{d} = \frac{532\,\text{nm} \cdot 3\,\text{mm}}{5.5\,\text{mm}} = 290\,\text{nm}, \tag{2.5}$$

where λ_{ex} is the wavelength of the excitation laser, d is the distance between the interfering beams at the back focal plane (BFP) of the objective lens, and f is the objective lens' principal focal length. The actual spacing of the interference line pattern observed in the raw SIM data is ~300 nm,which corresponds to the distance between the interfering beams at the BFP $d = 5.5034$ mm. This variance is caused by a minor disalignment of the laser beams in the pair.

It should be noted that changes in the separation between the beams in the back focal plane of the microscope objective lens currently require changing lens combinations in the telescope of our *fiberSIM* system. Thus, it is lacking the flexibility provided by the choice of patterns that can be projected by a SLM-based SIM system[30]. We are, however, currently developing methods that allow for the flexible adjustment of the separation of the beams in the back focal plane, which will enable us to easily switch

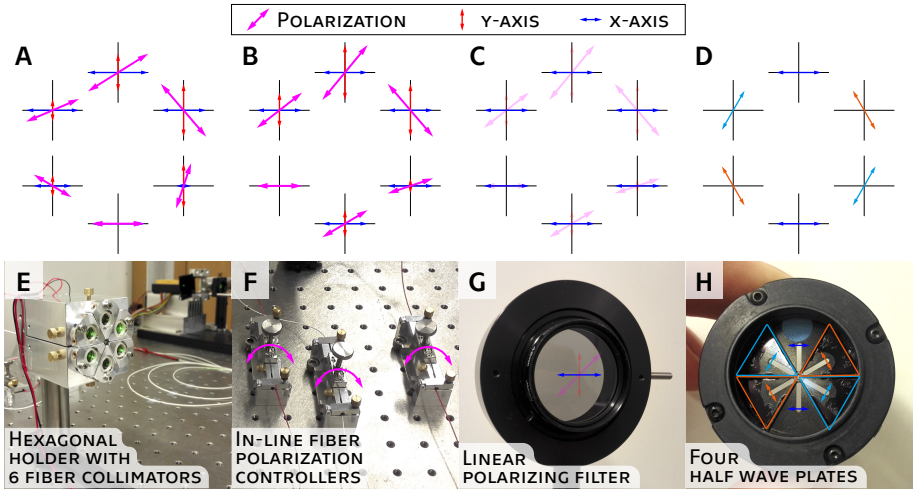

Figure 2.15: Intensity and polarization control of each individual laser beam step by step. (A) An orientation of polarization and light intensity of each individual beam at the outputs of 6 fiber collimators (E). Length of each magenta arrow represents the intensity of each laser beam. (B) Equalization of x-axis vectors by rotating the polarization of each beam using in-line fiber polarization controllers (F). (C) Linear polarizing filter (G) filters the x-axis component of each beam which results in the equal intensity and linear polarization of all 6 beams. (D) So called *pizza-shaped* half-wave plates (H) rotates the linear polarization of all beams in the desired orientation to achieve the maximum modulation depth of interference on the sample.

to grazing incidence and even TIRF excitation, where the highest spatial resolution in linear SR-SIM is achieved. Another benefit of our fiber-based SR-SIM implementation is that in a multicolor laser excitation system, the beam separation remains the same. Thus, incidence angles are maintained, which is rather important for TIRF and grazing incidence SR-SIM, and this makes such implementations more straightforward.

Ultra-compact MEMS based 1×4 fiber switch (Sercalo AG, Switzerland) is utilizing non-polarization maintaining broadband single mode fibers in the wavelength range of 480 nm - 650 nm. It provides a fairly low cost, but high speed means of switching light from an input fiber to four output fibers. The switching time between the four different output fibers is ∼3.5 ms (details in Section *2.3.3: Performance of the System*). Careful control of the polarization of interfering beams is critical for achieving a high pattern modulation depth. To control the polarization of the beams emitted from the non-polarization maintaining fibers, an in-line fiber polarization controller (Thorlabs, Inc., USA) is used for each optical fiber. These controllers in combination with the linear polarizing filter allow us to adjust the power of each individual beam (see Fig. 2.15). The *pizza-shaped* half-wave plate (Bolder Vision Optics, USA) placed directly behind the linear polarizing filter set the correct polarization for each beam pair to maximize the interference modulation depth. Being able to adjust the power of each beam is especially useful to compensate the different coupling efficiencies of the different fiber

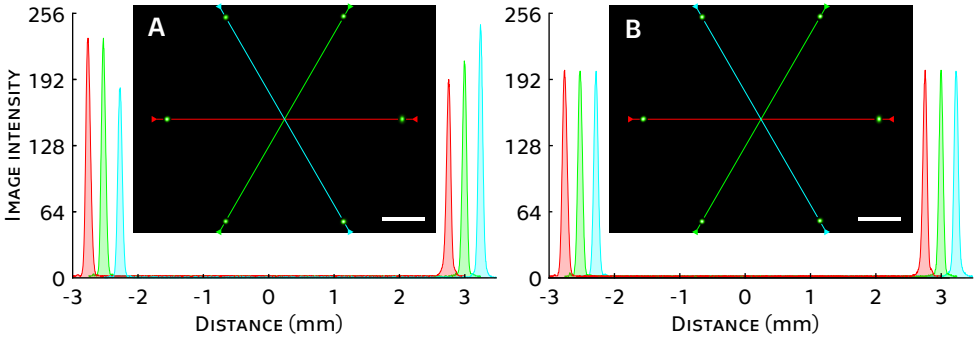

Figure 2.16: Example of the intensity profiles of the individual laser beams focused to the back focal plane of the microscope objective lens in front of and behind in-line fiber polarization controller based adjustments. (A) The image is the sum of three individual images (one image = one angle) where the intensities of the focus of each beam are not yet controlled. (B) The same image as shown in (A) after individual adjustment of the polarization state within each optical fiber by the in-line fiber polarization controller. The red, green and blue lines represent the line profiles acquired for each angle in the image, at 0°, 60°, and 120°, respectively. Line profiles are shown shifted along the x-axis with a step size of 240 µm to avoid overlapping of the peaks for better comparison. The field of view is limited by the physical size of the camera sensor (7.093 mm × 5.320 mm), thus the line profiles are limited to 6 mm despite the diameter of the back focal plane of the objective lens being ∼10 mm. The scale bars are 1 mm.

switch outputs and the coupling ratio tolerance of the 1×2 fiber splitters. In order to ensure that the intensities of all 6 beams are set equally, a CMOS camera can be placed at the position of the back focal plane instead of the objective lens. Figure 2.16 shows an example of a measurement of the beam intensities in front of and behind intensity adjustment with the in-line fiber polarization controllers.

2.3.2 Phase-shifting Accuracy of the Illumination Pattern

Shifting the phase of the interference pattern is achieved with a piezoelectric crystal (piezo). The open-loop piezo is a part of the hexagonal fiber collimator assembly, which is split in two opposing halves. One half, containing 3 fibers and their corresponding collimating lenses, can glide on metal rods in along the optical axis and is pulled against the piezo by a spring. By applying a voltage to the piezo, the piezo translates this half of the assembly against the stationary other half, resulting in a defined path

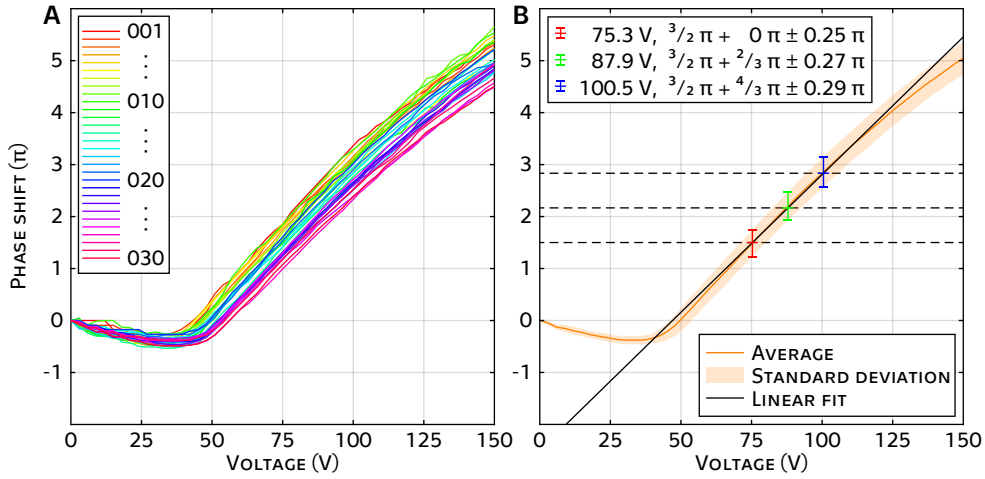

Figure 2.17: Measurement of the interference pattern phase shift induced by open-loop piezoelectric displacement of the fiber collimators. The graphs show a dependence of the pattern phase on the voltage applied to the piezoelectric crystal. (A) The phase curves were obtained by conducting the experiment in 30 cycles by applying a voltage between 0 V to 150 V with a step size of 2 V to the piezo crystal. (B) The mean (orange line) and the standard deviation (light orange area) of the measurements. The linear regression (black line) fits the average data in the range between 65 V to 120 V where the average phase shift exhibits an almost linear dependence on voltage. Black dashed lines indicate the ideal phase shifts of patterns (with $3\pi/2$ offset) utilized for the subsequent SR-SIM image reconstruction. The standard deviation of each phase shift is indicated by a colored error bar (red, green, and blue). This step size is equal to $2\pi/3$ to cover the entire field of view with 3 phase steps.

length difference (phase shift). In this initial implementation, we use an inexpensive piezoelectric crystal (Thorlabs, Inc., USA) operated in open-loop mode to achieve the spatial displacement of one of the fibers in each pair by up to 2 µm. Since the piezo does not contain a feedback sensor to monitor its length change, the corresponding phase changes, and in particular its reproducibility, need to be calibrated a priori. Precise knowledge of the phase of the SR-SIM illumination pattern is a rather critical parameter for accurate image reconstruction. If the phase estimation, which is typically conducted by analyzing raw SR-SIM images[55,115,116], is not sufficiently precise, then artifacts, i.e. line breaks, are created during image reconstruction. Such artifacts can also occur if the phase estimation is conducted only once on an initial raw image set, and it is then assumed that the phase shift is reproducible for images acquired at a later time point. These artifacts can be avoided either by accurately determining the phase shift for every raw image individually or by ensuring a very high degree of reproducibility, e.g. by using a piezo with a capacitive feedback sensor.

The presented *fiberSIM* system uses the first method, while also ensuring that the inexpensive piezo is operated in a highly linear range of the induced phase shifts. Figure 2.17 shows the dependence of the phase shift on the applied voltage of the piezo in the full range from 0 V to 150 V. To examine the reproducibility of the phase shift, the experiment was performed in 30 consecutive cycles, which are shown in Fig. 2.17A. The average of the 30 individual curves and the standard deviation shown in Fig. 2.17B illustrate the nonlinearity of the piezo displacement over the full voltage range. However, in the region from approximately 65 V to 120 V the curve is sufficiently linear to generate the equidistant phase shift over 2π as needed for successful artifact-free image reconstruction. The three dashed lines show the voltage points which were chosen for the three phase shifts required for successful SR-SIM image reconstruction. Please note that the displacements in the curves shown in Fig. 2.17A indicate a consistent unilateral long-term phase shift between the first and the last measurement of the cycle. This is currently the main source of uncertainty between the phase shifts. Improving the mechanical and thermal stiffness of the setup should allow us to further and drastically reduce this uncertainty.

2.3.3 Performance of the System

In this section, the *fiberSIM* system performance is demonstrated. To examine the speed of our SR-SIM system, two experiments were performed. The duration that it takes for the MEMS fiber switch to switch between output fibers (controlling the illumination pattern rotation) and the time that it takes the piezo-electric element to shift between discrete phase settings were measured. A free-space biased photo detector (Si detector DET10A, Thorlabs, Inc., USA) in combination with a digital oscilloscope was used for detecting the incidence light of the fiber collimators. The oscilloscope input is equipped with a load resistor $R_{load} = 1\,\mathrm{M}\Omega$ and the photo detector has a junction capacitance $C_j = 6$ pF. This configuration leads to the photo detector time response t_r equal to 13.2 µs, which is sufficient for our measurements, as can be seen below.

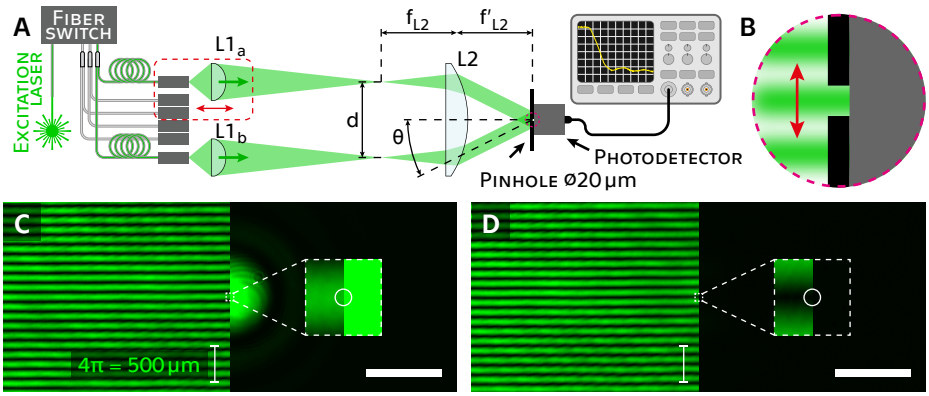

Figure 2.18: Illustration of the interference pattern phase shift speed measurement. (A) Experimental setup based on the 6-beam collimator holder (Fig. 2.13, or Fig. 2.14D), focusing lens L2 (f = 1000 mm), photo detector with a pinhole with diameter of 20 µm, and digital oscilloscope. Two collimated beams (with a distance d between each other equal to 4.3 mm) behind the lens L2 interfere in the focal plane f'_{L2}. Line spacing of the interference pattern was equal to $\lambda' = 532\,\text{nm} \cdot 1\,\text{m}/4.2\,\text{mm} = 125\,\mu\text{m}$ (see Eq. 2.5). (B) Detailed view at the pinhole placed in front of the photodetector with the interference pattern. Red arrows in (A) and (B) indicate the interference pattern phase shift. Images of the interference pattern on a camera chip in the position of the photodetector with the phase equal to 0: maximum intensity of the sinusoidal pattern (C), and phase equal to π: minimum intensity of the sinusoidal pattern (D). One half of the image displays full interference pattern, while the second half represents the light passing through 20 µm pinhole (white circle in the center of the dashed detail) placed right in front of the camera chip (this imitate the situation with the photodetector instead of the camera). The scale bars are 10 µm.

The time response between *OFF* and *ON* states of the fiber switch (see Fig. 2.19B) was measured by placing the photo detector directly in front of one of the six output collimators. For the measurement of the phase shifting speed, one pair of fiber collimator lenses focuses the beams to the negative focal plane of a f = 1000 mm lens. Distance between these two laser beams was equal to 4.2 mm. This creates a coarse interference pattern (from the equation 2.5, the line spacing was equal to ∼125 µm) in the positive focal plane where the photo detector with a pinhole with diameter of 20 µm is placed. This configuration allows us to sample the sinusoidal pattern with 6.25 samples over 2π. To ensure the maximum intensity difference on the photo detector, a phase shift of 1π resulting in a change from maximum intensity to a local minimum of the sinusoidal pattern. The smaller phase step of $2\pi/3$ as required for the pattern displacement in SR-SIM will, thus, only be faster.

If we consider that 3 angles in conjunction with 3 phase shifts per angle are required to reconstruct a 2D SR-SIM image, then the time required for switching these 9 patterns is equal to 39 ms. This corresponds to 3 phase shifts (3×6 ms) and 6 switches of the

angle (6×3.5 ms) - 3 remaining angle switches are executed simultaneously with the phase shift (see Fig. 2.19C). The theoretical maximum SR-SIM image rate can then reach ∼26 fps. The inexpensive industrial CMOS camera (IDS, Germany), which we utilized, can run at a rate of up to 41 fps. Acquisition of 9 consecutive images reduces the actual frame rate down to ∼4.5 fps, which makes the camera image acquisition time (∼25 ms) the only speed limitation of the fiber-based SR-SIM illumination unit. The current setup can run up to ∼4 SR images per second. If sliding window reconstruction is utilized[117], then this frame rate increases to ∼34 fps. Currently, the relatively long distance between the hexagonal collimator and the objective lens, as required by the long telescope ($f_{L2}+f_{L3} = 350$ mm), in combination with the telescope magnification ($f_{L2}/f_{L3} = 6\times$), restricts the effective field of view (FOV) of the illumination unit to 13.25 µm ×13.25 µm. This unit is, however, designed for flexibility, so that a larger FOV can be achieved by utilizing different lens sets.

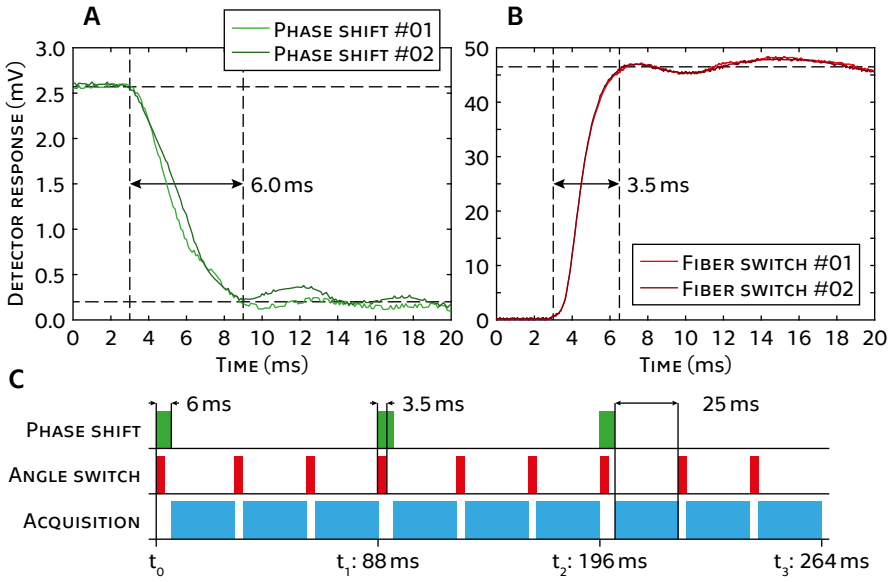

Figure 2.19: Speed measurements of the electro-mechanical components in the setup and timing diagram of the current SR-SIM raw data acquisition. (A) Measurement of the time required for a phase shift of 1π, where the horizontal dashed lines represent the maximum and minimum photo detector response, thus the maximum and minimum intensities of the sinusoidal line pattern. (B) Measurement of the time required for the MEMS fiber switch to switch from *OFF* to *ON* state. In both graphs, negligible ringing can be observed. (C) Timing diagram representing an acquisition of one raw dataset of 9 images (3 angles × 3 phases) required for 2D SR-SIM reconstruction.

2.4 The Potential of SIM in live cell biology

Structured illumination has proven great potential in many biological applications. Therefore, further development of this technique is in place. Recently published rapid SIM microscope allowing real-time imaging with doubled resolution *fastSIM*[71,109] is a representative example of a progress in SIM imaging. Moreover, the dual iterative SIM (SIM^2)[118] brings a 3D multicolor imaging tool with improved spatiotemporal resolution of 60–100 nm in lateral and <200 nm in axial dimension. SR-SIM imaging has been limited to single cells due to image quality degradation caused by optical aberrations in thick samples. Imaging deep into live organisms then becomes a very challenging task. Several approaches of deep SIM imaging have been presented, which are able to effectively compensate aberrations in thick samples[119,120].

Furthermore, the interesting combination of SIM with other techniques can profit from each other. Although SIM is capable of effective optical sectioning, TIRF can enhance the modulation depth of SIM illumination pattern, which allows imaging of the samples with lower fluorescence. Moreover, TIRF-SIM maximizes the lateral resolution enhancement by shifting the illumination pattern frequency to the limit of the objective lens[121]. Brunstein and coworkers utilized a compact Michelson-type interferometer to achieve total internal reflection fluorescence excitation SIM (TIRF-SIM) along three lateral directions[122]. Similarly, Cnossen et al. used an interferometric 2-beam SIM system to demonstrate a 2-fold improvement in the localization of single fluorescent molecules in a mechanism they called SIMFLUX[121,123]. Together with SIMFLUX, structured illumination based point localization estimator (SIMPLE)[124] have shown the increase in the SMLM precision to ∼5 nm. While optical fiber-based interferometers have, however, been utilized extensively to set up optical coherence tomography (OCT) instruments[125,126], they are currently underrepresented in SR-SIM microscopy, although such systems can offer some significant advantages. SIM illumination pattern generated by line-scanning has shown promising results even in an unmodified two-photon microscope[A4]. All these examples prove that structured illumination microscopy has great potential in biomedical research and deserves further development.

3

Assessing Resolution in Microscopy

The most common resolution assessment techniques and their current development are presented in the following chapter. The first section provides a brief overview of the resolution limits in fluorescence microscopy. The state of the art in the field of assessing resolution. Furthermore, an assessing resolution technique based on the power spectral density (PSD) analysis is presented. Parts of this chapter were published in the impacted journal GigaScience (2019)[A2], or presented at international conferences SPIE Optics+Photonics (2019, 2018)[A5,A6], SPIE Photonics Prague[A7], and IEEE International Conference Radioelektronika (2018)[A10].

Contents

3.1 Assessing Resolution in Microscopy

Theoretical resolution limits of an optical microscope have been defined as it is described in the Section *1.3: Resolution in Microscopy*. However, the actual resolution of a microscope image is affected by many factors, including the sample preparation, optical aberrations in the system, or a human factor that can cause, for instance, a slight defocus, thus losing the maximum resolution capability of the microscope. Therefore, an accurate resolution assessing tool is essential for the evaluation of the microscope

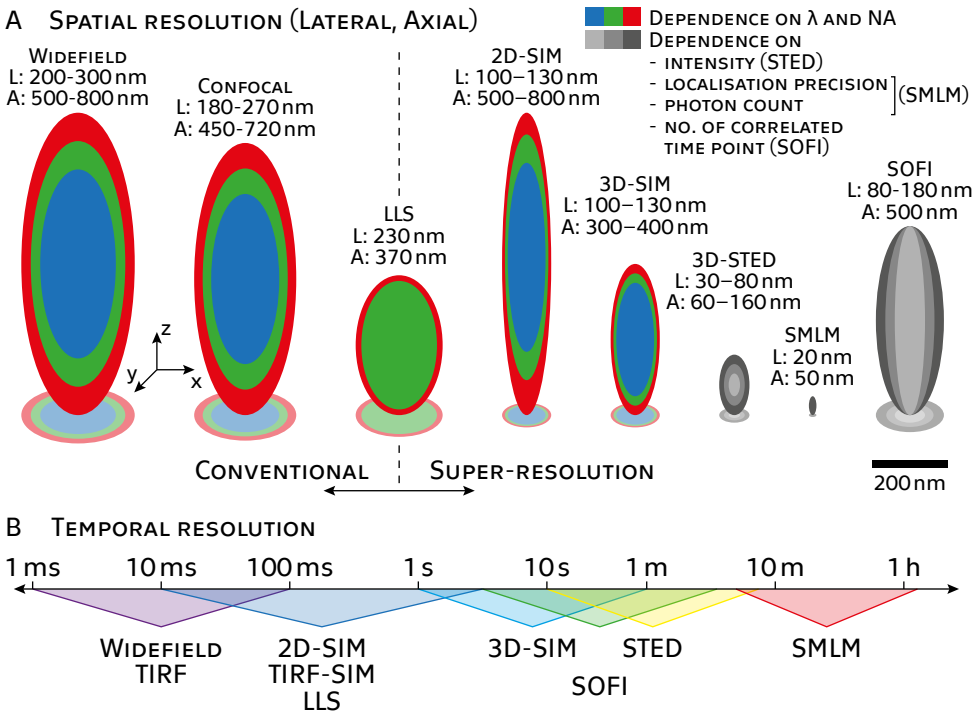

Figure 3.1: Visualization of the spatial (A) and temporal (B) resolution limits of a conventional and SR microscopy techniques. Ovals indicate the theoretical resolution in x, y, and z dimension of each microscope technique in optimal conditions. Red, green, and blue areas demonstrate the dependence of the resolution on the wavelength. The temporal resolution in (B) corresponds to the acquisition speed based on the lowest exposure time required to image a single plane with a comparable signal-to-noise ratio. The diagrams show that in order to increase the spatial resolution down to nano-scales, the temporal resolution has to be sacrificed, and vice versa. A good compromise is the SIM which doubles the resolution of the microscope with the rapid (close to real-time) acquisition[1].

image quality, especially in the super-resolution microscopy where the SR image can be degraded by improper settings of the reconstruction algorithm. In this chapter, the most common methods for estimation the resolution limit of the microscope system are discussed and the current development of the methods focused on the resolution estimation from a single image (video frame) is detailed. To get a better idea of the resolution limits in modern microscopy, Figure 3.1 visualises the spatial and temporal resolution limits of the most common conventional and SR microscopy techniques[1].

3.2 Conventional Assessment Methods

Conventional resolution assessment methods could be divided into two strategies. Measurement of image features in the spatial domain or using image Fourier transform analysis. The first approach is based on the measurement of full width at half maximum (FWHM), which requires one point source of light e.g. fluorescence beads. The FWHM is calculated from the line profile of the observed object. This line profile is usually fitted with a Gaussian distribution, which improves the sensitivity of measurement[58]. The resolution of an optical microscope can be characterized by the modulation transfer function (MTF). MTF is the magnitude response of the optical system to sinusoidal functions of different spatial frequencies and phase shifts. Generally, the MTF is a decreasing function of spatial frequency in Fourier domain. However, the MTF is often calculated from the image in spatial domain using calibration target with the periodic pattern[3,127]. Both FWHM and MTF approaches are well suitable for the evaluation of the microscope system resolution limits, however, calibrated samples (fluorescence beads or special resolution targets) are required. The reconstruction quality of any SR technique is often affected by the observed sample structure in cell biology. Therefore, an approach able to evaluate the resolution directly from the images of the real cell sample is essential. Resolution assessment methods based on Fourier transform analysis are frequently used in different variants[18,58,128] to determine the resolution in the reconstructed image. Nevertheless, the accurate estimation in live cell biology is still a challenging task. The Fourier ring correlation (FRC) provides an effective tool for measuring the resolution of SMLM images[18,19]. Despite FRC measure provides reliable resolution estimate of fixed samples (e.g. SMLM, or fluorescent beads) this approach in not applicable in live cell microscopy (further explanation in Section *3.2.3: Fourier Ring Correlation*). In 2019, Descloux et al. introduced a novel parameter-free image resolution estimation approach based on image decorrelation analysis[22] which provides promising results from a single image of a live cell. However, estimation of the resolution in the live cell video sequences is still very challenging task and further development in the field of resolution assessment in SR microscopy is essential.

In the following sections, the most common resolution assessing methods are discussed and the current development is presented.

3.2.1 Full Width at Half Maximum

The full width at half maximum (FWHM) is typically measured from individual fluorescent beads with the size below the diffraction limit of the system. This method is widely used to determine the resolving capability of the optical system due to the close connection with the Abbe diffraction limit. To determine the FWHM with higher precision, Gaussian function is fit to the horizontal and vertical line profiles of a fluorescent bead. The standard deviation σ of the Gaussian fit model directly leads to the FWHM of $2\sqrt{2\ln 2}\,\sigma$[58]. This resolution estimation approach is robust and provides very credible results under two conditions. First, the size of the fluorescent beads has to be below the diffraction limit of the system to be sure that the response to the light point source corresponds to the PSF. Second, the user has to ensure that the sample of fluorescent beads contains the individual isolated beads at which the FWHM is measured. When both conditions are fulfilled, the individual beads used for the measurement have to be selected manually.

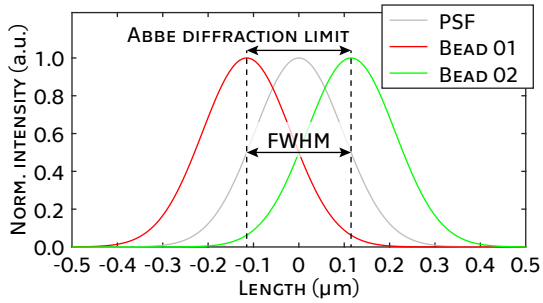

Figure 3.2: Illustration of how full width at half maximum relates to Abbe diffraction limit. Gray line represents the PSF of the system. Red and green lines represent line profiles of two fluorescent beads imaged with the diffraction limited system. Beads are in the distance of the Abbe diffraction limit, which corresponds to the FWHM of the PSF.

Figure 3.3 shows the FWHM measurements step by step. Manually selected individual beads on which the FWHM was measured are highlighted by white squares in the Fig. 3.3A. The improvement of the lateral resolution in both dimensions can be observed in the subfigures (B) and (C). Multiple gray lines in Fig. 3.3D and E represent x- and y-line profiles of individual beads from (A). The Gaussian fit model (red and cyan) is then applied to the average of all line profiles. From this model, the average FWHM value was determined. Although FWHM measurement offers a very accurate estimation of the resolution limit of an optical microscope, it has to be noted that the PSF shape typically varies over the full range of field of view[A10]. Furthermore, resolution estimation in cell structures is not possible since individual light emitters are required.

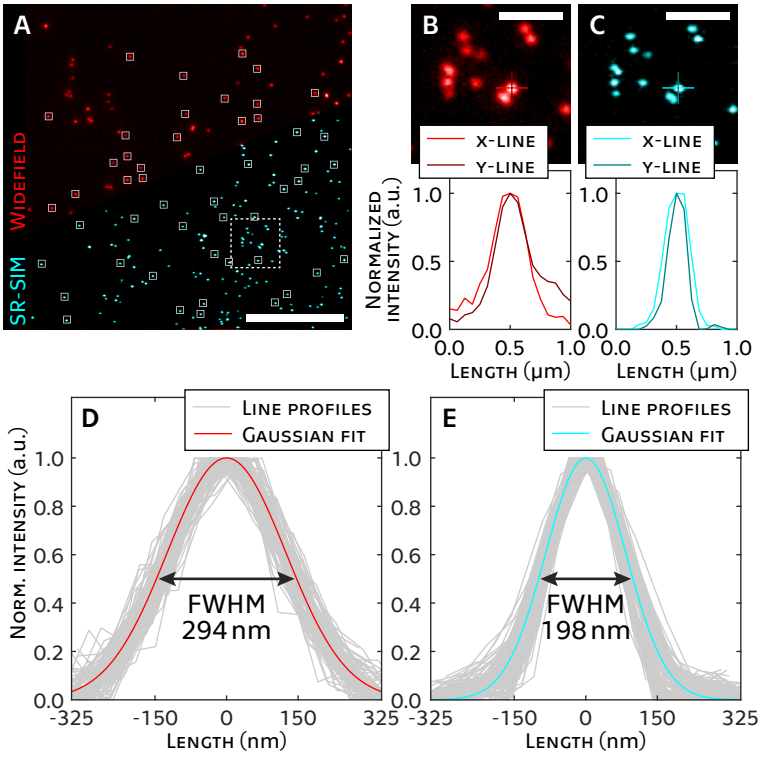

Figure 3.3: FWHM measurement demonstrated on fluorescent beads using FLCOS SIM system. (A) Widefield image (red) and SR-SIM reconstructed image (cyan) of the fluorescence beads with the size of 100 nm. White dashed box defines the region of interest detailed in (B) and (C). Horizontal and vertical normalized intensity profiles of the selected fluorescent bead are plotted in (B) and (C) to demonstrate the resolution enhancement in both lateral directions. Grey lines in (D) and (E) correspond to the x- and y-line profiles of all individual beads marked with white box in (A). The Gaussian fit model is applied on the average of all grey line profiles. The standard deviation of this model corresponds directly to the FWHM. The scale bar in (A) is 10 µm. The scale bars in (B) and (C) are 2 µm.

3.2.2 Modulation Transfer Function

One of the most important parameters in optical microscopy is the resolution and the related modulation transfer function (MTF). The MTF gives the information about the contrast that the optical system can achieve depending on the spatial frequency. The spatial frequency where the MTF drops to zero (for noiseless images) is called *cut-off* frequency. It corresponds to the resolution of the optical system[3,129–132]. A straightforward way to measure the MTF is to acquire an image of an ideal point light source that creates an Airy disk in the image plane of the optical systems. This

shape corresponds to the point spread function (PSF) of the optical system. Using the Fourier transform the optical transfer function (OTF) is calculated. The module of OTF corresponds to the MTF. The main limitation of this method is the complex realization of a close to ideal point light source. However, this approach is often used in fluorescence microscopy by imaging an individual fluorescent bead. In the following sections, the two most common methods of the MTF evaluation are detailed.

Resolution Target

Several types of resolution test charts are used in optical microscopy (e.g., 1951 USAF, or Siemens star resolution target). These charts contain a set of precisely manufactured patterns with an increasing spatial frequency. These patterns are usually dark (black) and bright (white) stripes oriented in the horizontal and vertical direction (see Fig. 3.4B and C). The modulation transfer function (MTF) is then given by the contrast of each

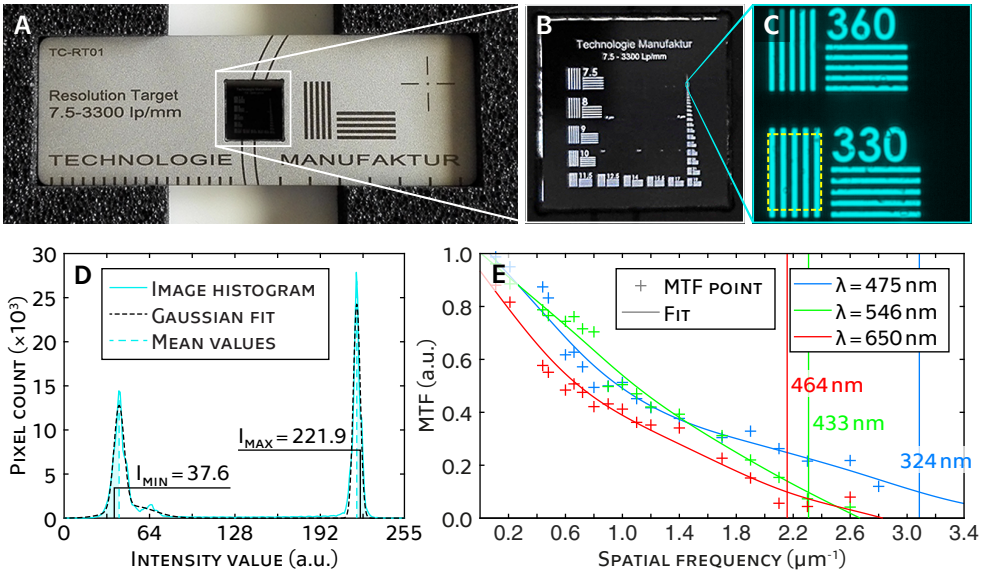

Figure 3.4: Example of the histogram evaluation approach in a brightfield microscope. (A) Resolution target designed for brightfield microscopy. Close details of the resolution target are shown in (B) and (C). (D) Image histogram of the region of interest (yellow dashed box in (C)). The cyan line represents the histogram of the input image while the black dashed line shows the Gaussian fit. The cyan dashed lines point out the Gaussian distributions mean values. I_{min} and I_{max} are determined as the average of the pixels belonging to the cyan area below and above the mean values, respectively. (E) MTF results for three wavelengths. Red, green, and blue cross marks represent the contrast measured in the individual stripe patterns. These MTF points are fitted by smoothing splines for better visualization.

pattern with a certain frequency as the following[129,130]

$$\mathrm{MTF}(\boldsymbol{k}) = \frac{\frac{I(\boldsymbol{k})_{max} - I(\boldsymbol{k})_{min}}{I(\boldsymbol{k})_{max} + I(\boldsymbol{k})_{min}}}{\frac{I_{wht} - I_{blk}}{I_{wht} + I_{blk}}}, \tag{3.1}$$

where $I(\boldsymbol{k})_{max/min}$ represents the maximum/minimum intensity in line pair with corresponding spatial frequency $\boldsymbol{k} = (k_x, k_y)$. I_{wht} and I_{blk} are constants with the highest and the lowest intensity value of the measured image, respectively.

To increase the accuracy of the image values readout, the semi-automated statistical approach based on histogram evaluation can be used. Assuming that the region of interest (yellow dashed ROI in Fig. 3.4C) only consists of black and white areas blurred by PSF, the two major peaks can be observed in the image histogram (Fig. 3.4D). In the ideal case, these histogram peaks have a shape close to the Gaussian distribution. The histogram evaluation exploits the mean values of the Gaussian distribution (dashed cyan lines) to determine the area where the maximum and minimum values are estimated (light cyan areas in Fig. 3.4D). The final values I_{min} and I_{max} are then calculated as the average of all pixels within this area. With the increasing spatial frequency of the

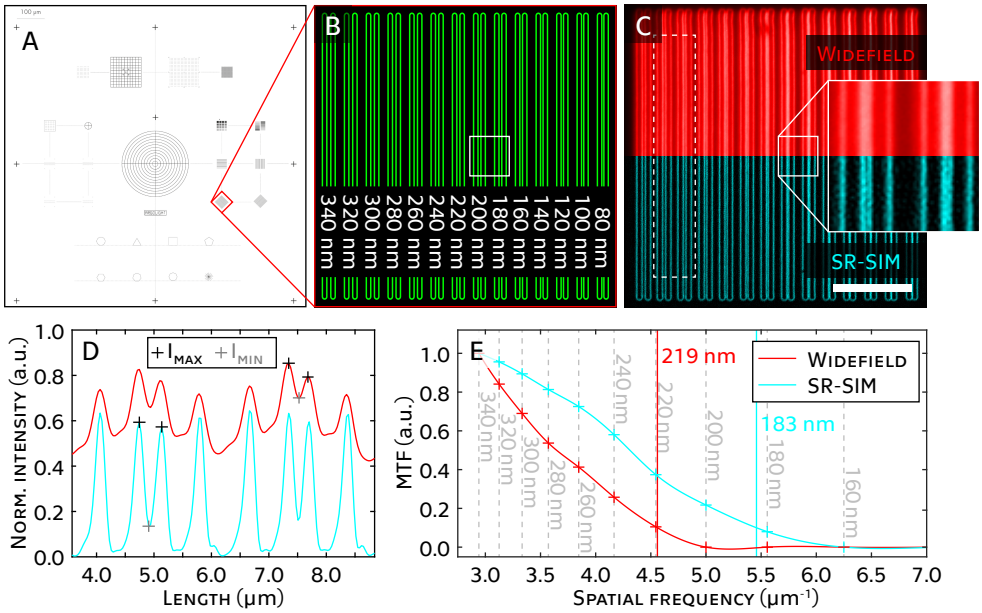

Figure 3.5: MTF measurement using Argo-SIM monitoring slide (Argolight, France). (A) Overview of the whole slide containing 14 different patterns. (B) Illustration of the 45° oriented Pattern E – gradually spaced pairs of 36 µm-long lines which spacing gradually increases, from 80 to 340 nm, with a step of 20 nm and it's real widefield and SR-SIM image (C). Line profiles in (D) correspond to the ROI (dashed white box) in (C). Modulation transfer functions of the widefield and SR-SIM images are plotted in the graph (E). The scale bar in (C) is 10 µm.

stripe patterns, the contrast drops to zero. Wavelength dependency can be observed on the MTF diagram (Fig. 3.4E).

A slightly different approach of the MTF determination brought French company Argolight. Precisely manufactured Argo-SIM[d] monitoring slide consists of 14 different patterns designed to check the stability of the characteristics of the microscope system. Pattern E contains pairs of 36 µm-long lines with spacing that gradually increases from 80 to 340 nm, with a step of 20 nm. The MTF is then calculated using Eq. 3.1, where the $I(\boldsymbol{k})_{max}$ is defined by the average of the maximum intensities of neighbouring lines in pair and $I(\boldsymbol{k})$ corresponds the minimum intensity in between these two lines (see Fig. 3.5D).

Individual Fluorescence Bead

Modulation transfer function represents the absolute value of the optical transfer function (OTF) which corresponds to the Fourier transform of the optical system response (point spread function - PSF) to an infinitely small light source (see Section *1.3: Resolution in Microscopy*). Assuming a diffraction limit of the microscope ∼300 nm, and SR-SIM doubling this resolution limit, a fluorescent bead with the diameter of 100 nm suits for the following experiment. The fluorescent bead smaller than the diffraction limit of the microscope appears as the system PSF on the image plane of the objective lens. Absolute value of the PSF's Fourier transform results in desired MTF. Measuring the MTF from a single fluorescent bead can be quite inaccurate since the shape of one PSF

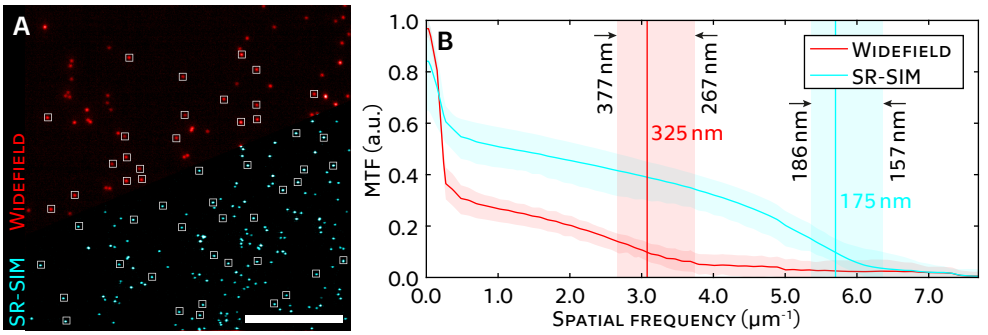

Figure 3.6: MTF measurement using individual fluorescence beads. (A) Widefield image (red) and SR-SIM reconstructed image (cyan) of the fluorescence beads with the size of 100 nm. (B) All modulation transfer functions are calculated by circular averaging the magnitude of the Fourier transform of individual beads marked with a white box in (A). Red and cyan MTF lines display the average MTF for each microscopy technique, widefield and SR-SIM. Light areas around these MTF lines represent different MTFs measured over the full field of view. The scale bar is 10 µm.

[d] https://argolight.com/products/argo-sim/

can be affected by several factors, e.g., low signal-to-noise ratio, presence of a second bead closer than the diffraction limit, or optical aberrations in the system. Therefore, selecting a subset of isolated individual beads distributed over the field of view (white boxes in Fig. 3.6A) is recommended. Subsequent averaging of the MTFs provides more accurate measurement. Variance of the MTFs over the field of view can be seen in the Fig. 3.6B, where the light red and cyan area display all overlapping MTFs calculated from all selected beads.

Edge Spread Function

Any sharp knife-edge where the light intensity drops from the maximum (bright) to minimum (dark) is blurred by the optical system PSF (see Fig. 3.7). The steepness (gradient) of such intensity edge increases with the better resolving capability of the system. The line profile perpendicular to this knife-edge is called edge spread function ESF which contains 1D information about the PSF of the system. The first derivative

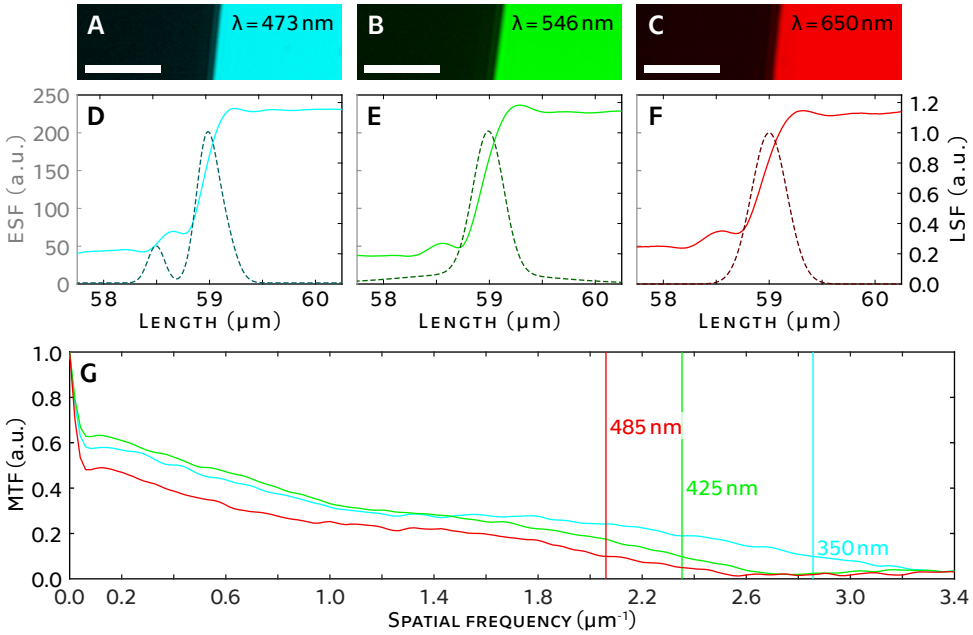

Figure 3.7: MTF measured from the edge spread function (ESF). (A) The sharp knife-edge of the resolution target was imaged with the UPlanFLN 40×/0.75 air/dry objective lens in a brightfield mode using three wavelengths (473 nm, 546 nm, and 650 nm). (B) The averages of the edge spread functions over the height of the edge from (A) with the first derivatives of ESFs, thus line spread functions (LSF, dashed dark lines). (C) The modulation transfer functions as the absolute values of the Fourier transform of each LSF. The scale bars are 10 µm.

of the ESF results in the line spread function LSF which can be considered as one dimensional PSF. The MTF corresponds then to the absolute value of the Fourier transform of LSF[133]. In order to reduce noise in the image, it is appropriate to use the averaging of multiple line profiles over the length of the edge. However, any shift between the ESF line profiles results in degradation of the edge sharpness, thus devaluing the MTF measurements. Therefore, it is necessary to ensure the individual ESF line profiles are not shifted relative to each other.

Edge spread function experiment was performed usingUPlanFLN 40×/0.75 air/dry objective lens mounted in the IX71 bright-field microscope (Olympus, Japan). Three illumination single bandpass filters were used with the center wavelength of 473 nm, 546 nm, and 650 nm, respectively, to image the sharp edge of the resolution target. Rayleigh resolution limits (Eq. 1.4 in the Section 1.3.1) of the microscope setup for each illumination wavelength are equal to $d = 385$ nm, 444 nm, and 529 nm, respectively.

ESF approach can be also applied to cell samples instead of precisely manufactured testing slides. However, one condition has to be fulfilled. The gradient of the edge must be higher than the gradient of the system point spread function. Therefore, the

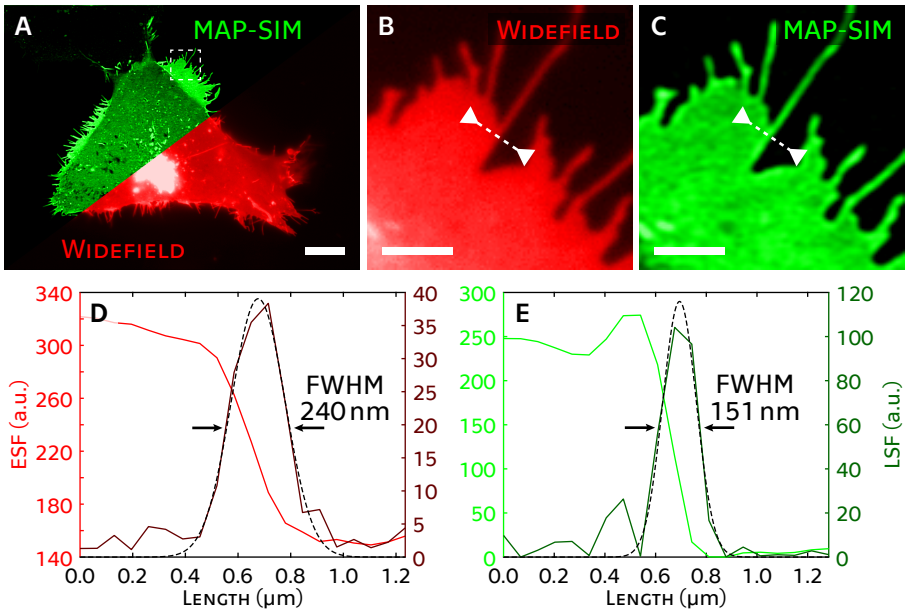

Figure 3.8: FWHM measured from the edge spread function (ESF). (A) Widefield image (red) and MAP-SIM reconstructed image (green) of the U2-OS cell. White dashed box in (A) marks the details in (B) and (C), where the dashed white lines with arrows show the edge spread functions (dark red and green) plotted in (D) and (E). Gaussian functions (black dashed lines) fit the line spread functions (red and green) in order to determine the full width at half maximum (FWHM).

selection of the proper edge is usually a manual task. The advantage of this method is that there is no need to use any special test pattern[130]. Moreover, the FWHM can be calculated from the line spread function directly (Fig. 3.8).

3.2.3 Fourier Ring Correlation

Fourier ring correlation FRC evaluates the similarity of two stochastically independent images of the same observed scene in frequency space to determine the resolution threshold. These two identical observations differ only in noise content. In 2013, Banterle et al. have shown the FRC can be applied to SR data[18]. In order to generate two identical images $I_1(x, y)$ and $I_2(x, y)$ the raw SMLM dataset is usually split into two subsets (e.g. first subset contains odd frames and second subset consists of even frames). The SMLM reconstruction method is then applied to both datasets, resulting in two identical images with different noise content. Another way how to get these two stochastically independent images is an acquisition of the one fixed sample twice in minimum delay between acquisition. The FRC is then calculated as

$$FRC(q) = \frac{\sum_\theta \widetilde{I}_1(q,\theta)\widetilde{I}_2(q,\theta)^*}{\sqrt{\sum_\theta \left|\widetilde{I}_1(q,\theta)\right|^2 \sum_\theta \left|\widetilde{I}_2(q,\theta)\right|^2}} \tag{3.2}$$

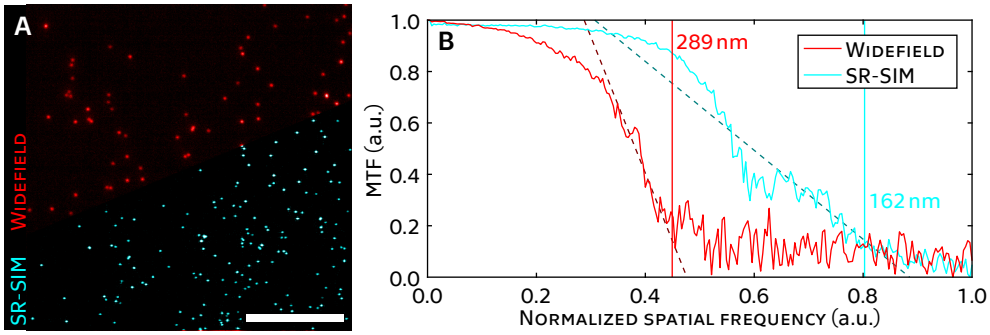

Figure 3.9: Fourier ring correlation (FRC) measurement on fluorescent beads. (A) Widefield image (red) and SR-SIM reconstructed image (cyan) of the fluorescence beads with the size of 100 nm. (B) FRC calculated from two consecutively acquired images of fluorescent beads. Dashed lines illustrate linear slope of the FRC decline, where the cut-off frequency is estimated. The threshold value for determining the cut-off frequency is 1/7, which is the most appropriate value for microscopy images[134,135]. The spatial frequency is normalized by the sampling rate $f_s = 1/(2 \cdot pps) = 7.69\,\mu m^{-1}$, where $pps = 65$ nm is a projected pixel size given by the physical size of the pixels on the camera sensor (6.50 µm) and the magnification of the objective lens in combination with the tube lens (100×). The scale bar is 10 µm.

where $\widetilde{I}(q,\theta)$ is complex Fourier transform of the image $I(x,y)$ with polar coordinates (frequency q and angle θ). Symbol * denotes complex conjugate. The FRC curve reaches 1 for low frequencies close to DC component, whereas for high spatial frequencies the FRC decays to 0. The cut-off frequency is determined as the frequency where the FRC curve drops below fixed threshold 1/7, which has been experimentally determined as the most appropriate value for microscopy images[134,135].

Recently, Laine et al. have presented NanoJ - a high-performance open-source super-resolution microscopy toolbox[20], which contains a resolution assessing tool called NanoJ-SQUIRREL (super-resolution quantitative image rating and reporting of error locations). This tool provides complex image quality measurement including mapping of FRC resolution across an image.

3.2.4 Summary of the Conventional Assessment Methods

Conventional methods for assessing the resolution described above typically provide a reliable and accurate estimation of the resolution limits of the microscopy system. However, specific samples, e.g., precisely manufactured resolution charts or fluorescent beads, are required for these measurements. The exception might be the Fourier ring correlation, which can measure the resolution directly from the cell sample. Nevertheless, two observations of the same static sample are essential for the accurate measurement. Any spatial change within the sample during the acquisition decreases the resolution limit and devalues the measurement. Moreover, the final resolution in the image of a live cell is strongly affected by the cell structure. Therefore, these methods do not seem to be well suited for resolution measurements within live cell imaging, where the evaluation resolution of a single image (video frame) is essential. Recently, Descloux et al. have introduced an image resolution assessment method based on decorrelation analysis[22], which brings a novel approach of assessing the resolution limit of a single image. Further development of robust resolution assessment methods in SR-SIM microscopy is still necessary.

3.3 Circular Average Power Spectral Density

In this section, a quantitative evaluation of the resolution enhancement based on the circular average power spectral density ($\mathrm{PSD_{ca}}$) analysis is presented. PSD describes the distribution of the power of a signal with respect to its frequency. The PSD of an image $I(\boldsymbol{r})$ is the squared magnitude of its Fourier transform, that can be written as

$$\mathrm{PSD}(\boldsymbol{k}) = \left|\mathscr{F}\left\{I(\boldsymbol{r})\right\}\right|^2 \tag{3.3}$$

where $\mathscr{F}$ represents the Fourier transform, $\boldsymbol{r} = [r_x, r_y]$ indices individual pixels of the 2D image, respectively, and $\boldsymbol{k} = [k_x, k_y]$ are coordinates in the discrete frequency domain. The circular average PSD ($\mathrm{PSD_{ca}}$) is then calculated in polar coordinates with frequency q and angle θ as

$$\mathrm{PSD_{ca}}(q) = 10 \cdot \log_{10}\left(\frac{1}{N_q}\sum_{\theta}\mathrm{PSD}(q,\,\theta)\right) \tag{3.4}$$

which averages PSD at spatial frequency q. N_q is the number of spectral coefficients at a particular frequency q.

Assuming a noiseless case, the cut-off frequency is equal to the spatial frequency at which $\mathrm{PSD_{ca}}$ drops to zero. In practice, $\mathrm{PSD_{ca}}$ contains non-zero values over the whole frequency range caused by noise. The signal-to-noise ratio (SNR) in Fourier space is generally very close to the cut-off frequency, which makes precise determination of the cut-off frequency very challenging. Therefore, the spectral subtraction method[A7] is used before the cut-off frequency estimation. Assuming additive noise in the frequency domain, $\mathrm{PSD_{ca}}$ after the spectral subtraction is equal to

$$\widehat{\mathrm{PSD}}_{\mathrm{ca}}(q) \approx \mathrm{PSD_{ca}}(q) - \mathbb{E}\left[|N(q)|\right] \tag{3.5}$$

where $\mathrm{PSD_{ca}}$, $\widehat{\mathrm{PSD}}_{\mathrm{ca}}$, and $\mathbb{E}\left[|N(q)|\right]$ represent the noisy signal, the desired signal, and the noise spectrum estimate, respectively. The noise spectrum $|N(q)|$ is estimated from

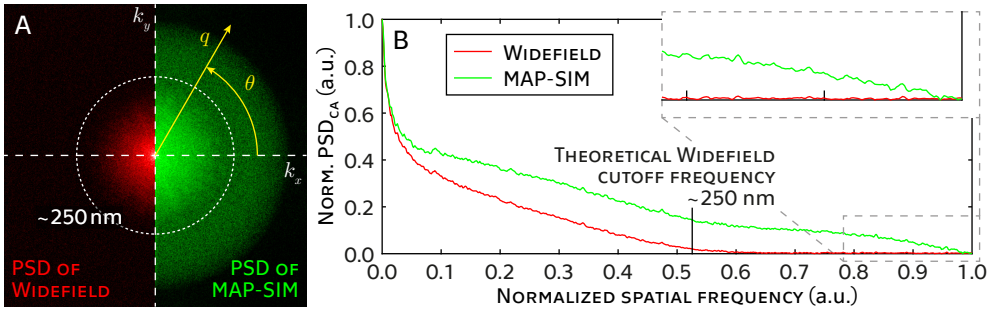

Figure 3.10: Explanation of the circular average power spectral density approach. (A) Two dimensional power spectral density (PSD) of the widefield (red) and MAP-SIM image. White dashed lines represent the Cartesian coordinates, and yellow arrows represent the polar coordinates in the frequency domain. The theoretical diffraction limit of the microscope ~250 nm is marked with the white dashed circle. (B) Normalized $\mathrm{PSD_{ca}}$ curves are defined as an average of the 2D PSDs (A) over the θ in the polar coordinates. Detailed view on the higher frequencies (dashed box) shows the area of $\mathrm{PSD_{ca}}$ where the noise used in the noise subtraction step is estimated. The spatial frequency is normalized by the sampling rate $f_s = 1/(2 \cdot pps) = 7.69\,\mu\mathrm{m}^{-1}$, where $pps = 65$ nm is a projected pixel size given by the physical size of the pixels on the camera sensor (6.50 µm) and the magnification of the objective lens in combination with the tube lens (100×).

the parts of $\mathrm{PSD_{ca}}$ signal where only noise is present. Assuming that the $\mathrm{PSD_{ca}}$ at the last 5% of the highest frequencies does not contain any useful information, the frequency threshold varies over the range $\langle 0.95 \cdot q_{max};\, q_{max} \rangle$ for the noise estimation. The average cut-off frequency with the variance is given by this iterative measurement. The q_{max} is equal to

$$q_{max} = \frac{q_s}{2} = \frac{1}{2 \cdot pps}, \tag{3.6}$$

where q_s and pps are the sampling frequency and the projected pixel size, respectively. The resolution limit then corresponds to the frequency for which the $\widehat{\mathrm{PSD}}_{\mathrm{ca}}$ drops below 5%. Compared to the threshold $1/7 = 0.143$, used in Fourier ring correlation method (Section 3.2.3), experimentally determined threshold 0.05 provides the most accurate results after the noise subtraction step.

3.3.1 Estimation in Different Fourier Space Sectors

Structure of the cell sample may affect the resolution measurements in different angles, e.g., SIM reconstruction using only one angle of illumination pattern. Standard $\mathrm{PSD_{ca}}$ calculates the circular average of the Fourier transform along 2π. It leads to suppressing the potential maximum cut-off frequency achieved by averaging both the maximum and minimum f_c. To avoid this, the Fourier space can be divided into several sectors by the angle θ. The number of averaged points over the circle in the Fourier space is

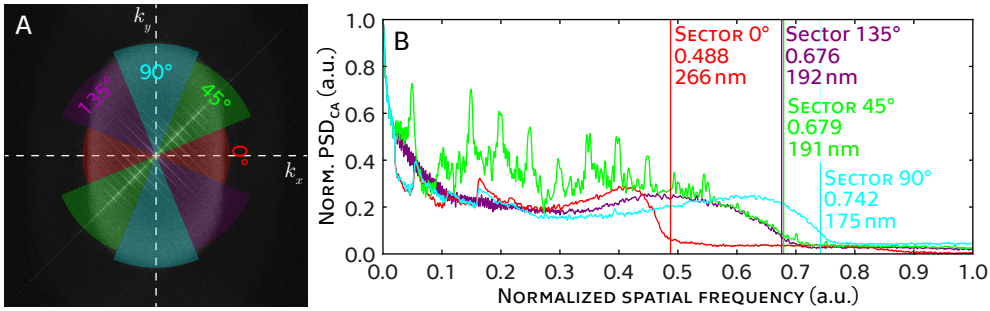

Figure 3.11: $\mathrm{PSD_{ca}}$ averaged within 4 equally distributed sectors. (A) Power spectral density of the SR-SIM reconstruction using only one illumination pattern angle which results in uneven estimation of the resolution enhancement over 360°. Transparent colored areas in (A) highlight the sector the resolution was measured in. The radius of each sector represents the cut-off frequency estimated using the $\mathrm{PSD_{ca}}$ method. Vertical lines in (B) represent the cut-off frequencies, thus resolution limits, of each normalized $\mathrm{PSD_{ca}}$ measured in different sectors. The spatial frequency is normalized by the sampling rate $f_s = 1/(2 \cdot pps) = 7.69\,\mu\mathrm{m}^{-1}$, where $pps = 65\,\mathrm{nm}$ is a projected pixel size given by the physical size of the pixels on the camera sensor (6.50 µm) and the magnification of the objective lens in combination with the tube lens (100×).

much lower closer to the zero frequency. However, frequencies higher then $0.5 \cdot f_s$ are important for determining the cut-off frequency where the number of averaged points is high enough even in reducing the averaged sector. Sectors are equally divided by N, where the sector angle limits are defined as

$$\theta_n = \frac{\pi}{2N}\langle 2\,(n-1)-1, 2n-1) \tag{3.7}$$

3.3.2 Welch's Method for Spectral Density Estimation

Welch's power spectrum estimation is a classical *non-parametric* method, which makes no assumption on image data generation. This estimation technique can reduce the variance in the spectral estimate[136,137], which is essential for cut-off frequency determination. Reducing the variance in the periodogram, an estimate of the spectral density of a signal[138], involves three main steps. First, assume a 1D data sequence $s(x)$ is subdivided into L segments as

$$\begin{aligned} s_i(x) = s(x+iD), \qquad & x = 0, 1, \ldots, M-1 \\ & i = 0, 1, \ldots, L-1 \end{aligned} \tag{3.8}$$

where M is the length of each segment, D is the segment shift, and iD corresponds to the starting point for i-th segment. If $D = M/2$, there is 50% segments overlap.

Then, for each i-th segment, the periodogram is computed as

$$\tilde{P}_{ss}^{(i)}(f) = \left|\mathcal{F}\left\{s_i(x)w(x)\right\}\right|^2 = \frac{1}{U}\left|\sum_{x=0}^{M-1} s_i(x)w(x)e^{-j2\pi fx}\right|^2, \tag{3.9}$$

where $\mathcal{F}$ represents Fourier transform (fast Fourier transform - FFT - for discrete signals), U is a normalization factor for the power in the window function $w(n)$ and is calculated as

$$U = \sum_{x=0}^{M-1} w^2(x). \tag{3.10}$$

The final Welch's power spectrum estimate is the average of all periodograms[136]:

$$P_{ss}^{W}(f) = \frac{1}{L}\sum_{i=0}^{L-1} \tilde{P}_{ss}^{(i)}(f). \tag{3.11}$$

Welch's PSD approach only works correctly with stationary signals. This condition allows to achieve noise suppression in the power spectral density estimate. To fulfill the stationarity of the measured image, we assume a single cell in the middle of the image

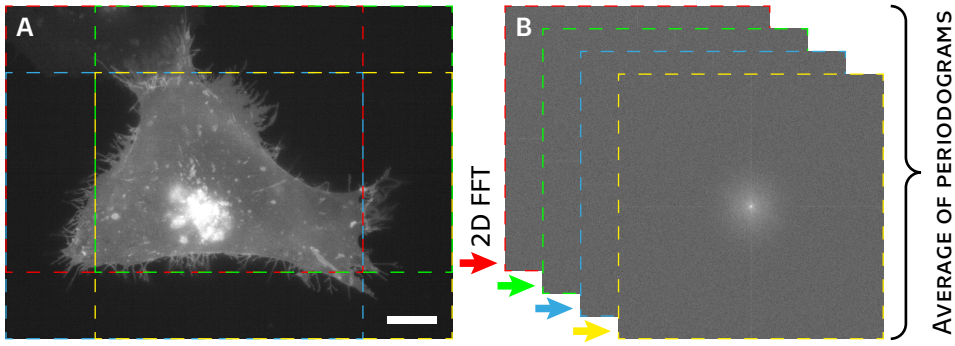

Figure 3.12: Welch's method for power spectral density estimation in 2D. (A) Observed live cell image. (B) The final average of periodograms illustration. Periodograms are calculated using Eq. 3.12. The scale bar is 10 µm.

surrounded with a noise background (Fig. 3.12). This assumption allows us to define 2D discrete periodograms

$$\begin{aligned}\tilde{P}_{ss}^{(i)}\left[\boldsymbol{k}\right] &= \left|\mathcal{F}\left\{s_i\left[\boldsymbol{r}\right] w\left[\boldsymbol{r}\right]\right\}\right|^2 \\ &= \frac{1}{U}\left|\sum_{r_x=0}^{M-1}\sum_{r_y=0}^{N-1} s_i[\boldsymbol{r}]w[\boldsymbol{r}]e^{-j2\pi\left(k_x\frac{r_x}{M}+k_y\frac{r_y}{N}\right)}\right|^2\end{aligned} \tag{3.12}$$

with normalization factor

$$U = \sum_{r_x=0}^{M-1}\sum_{r_y=0}^{N-1} w^2(\boldsymbol{r}), \tag{3.13}$$

where $\boldsymbol{r} = [r_x, r_y]$ indices the individual pixels of 2D image, respectively, and $\boldsymbol{k} = [k_x, k_y]$ are coordinates in the discrete frequency domain.

Final smooth 2D-Welch's power spectral density estimate is then achieved by substitution of 2D-periodograms into the Eq. 3.11. In the experiments, 2-dimensional fast Fourier transform (2D FFT) was used, utilizing MATLAB[139] build-in function.

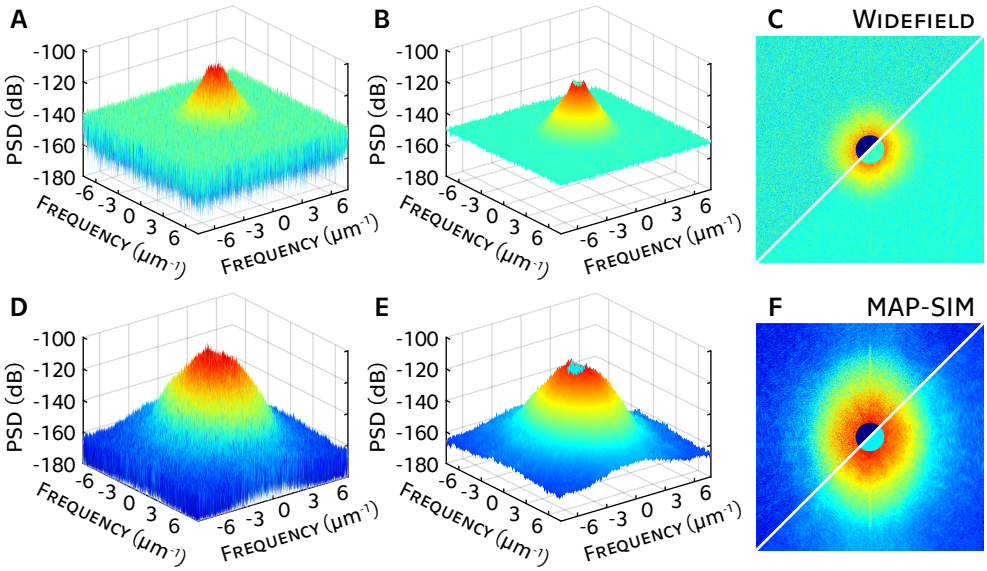

Figure 3.13: Results of the smoothing using Welch's method. (A) and (D) are 3-dimensional representation of the power spectral densities of Widefield and MAP-SIM images, respectively. (B) and (E) show the periodograms of the same image as (A) and (D) after applying the Welch's method. Images (C) and (F) show the 2-dimensional representation of images (A), (B), (D), and (E).

3.3.3 Power Spectral Density Analysis Results

The performance of the resolution assessment method based on the power spectral density analysis was tested on several datasets representing different scenarios, e.g., live cell video sequence, multiplane (3D) imaging, or SIM data reconstructed only in one direction. PSD_{ca} estimates resolution in a single 2D image, therefore, all data sequences (video, or 3D dataset) were processed frame by frame. The following figures display the

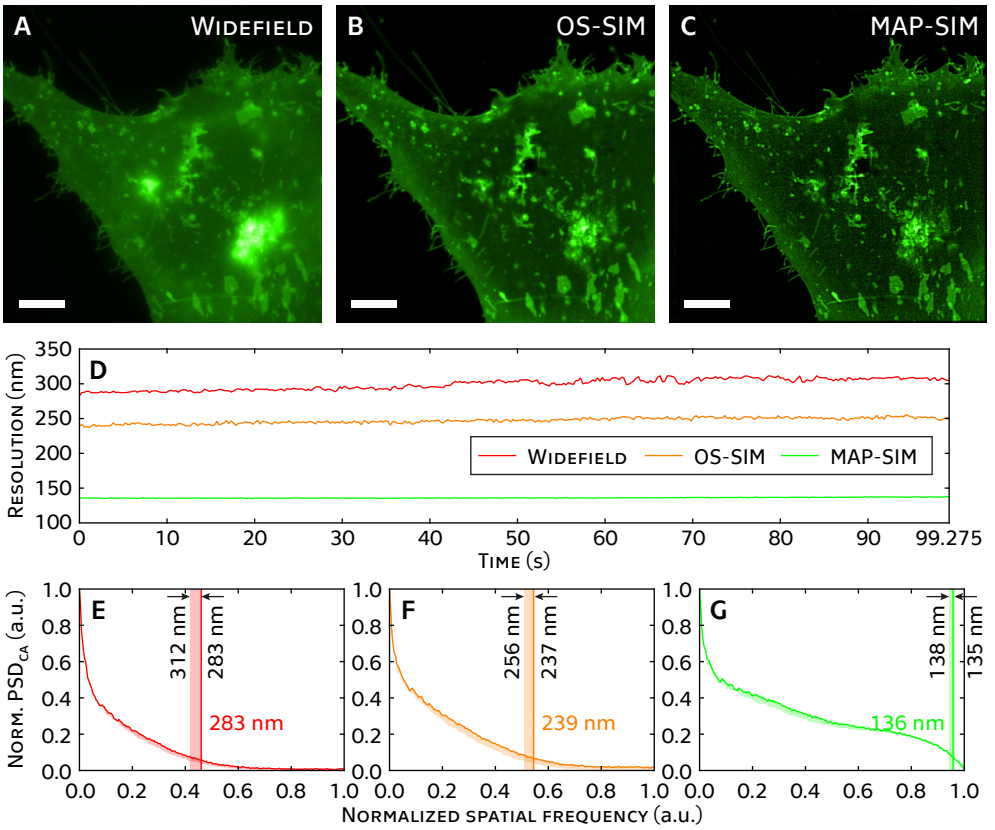

Figure 3.14: The results of PSD_{ca} measurement on the video sequence of live U2-OS cell (**SIM data 1** in the Section 2.2) expressing LAMP1-GFP. (D) The evolution of resolution in the video sequence of live cell measured with PSD_{ca}. The power spectral density lines in (E)-(G) represent the PSD_{ca} analysis of the first frame of the video sequence (A)-(C). Light areas around the lines correspond to the PSD_{ca} lines of the full video sequence (362 frames, 99.275 s). The spatial frequency is normalized by the sampling rate $f_s = 1/(2 \cdot pps) = 7.69\,\mu m^{-1}$, where $pps = 65$ nm is a projected pixel size given by the physical size of the pixels on the camera sensor (6.50 µm) and the magnification of the objective lens in combination with the tube lens (100×).

results of individual measurements.

Figure 3.14 shows the result of the PSD_{ca} measurement of ∼100 s long video of live HEP-G2 cell. Experiment includes widefield, OS-SIM, and MAP-SIM video sequences (Fig. 3.14A-C) presented in the Section 2.2 as **SIM data 4**. Fig. 3.14D displays the dependence of the resolution on the time. Widefield and OS-SIM show slow degradation of the resolution caused mostly by the photobleaching (light-induced degradation)[31] of the fluorophores leading to lower signal-to-noise ratio (SNR). However, MAP-SIM reconstruction is able to restore details even with bad SNR conditions and keep the resolution very stable over time.

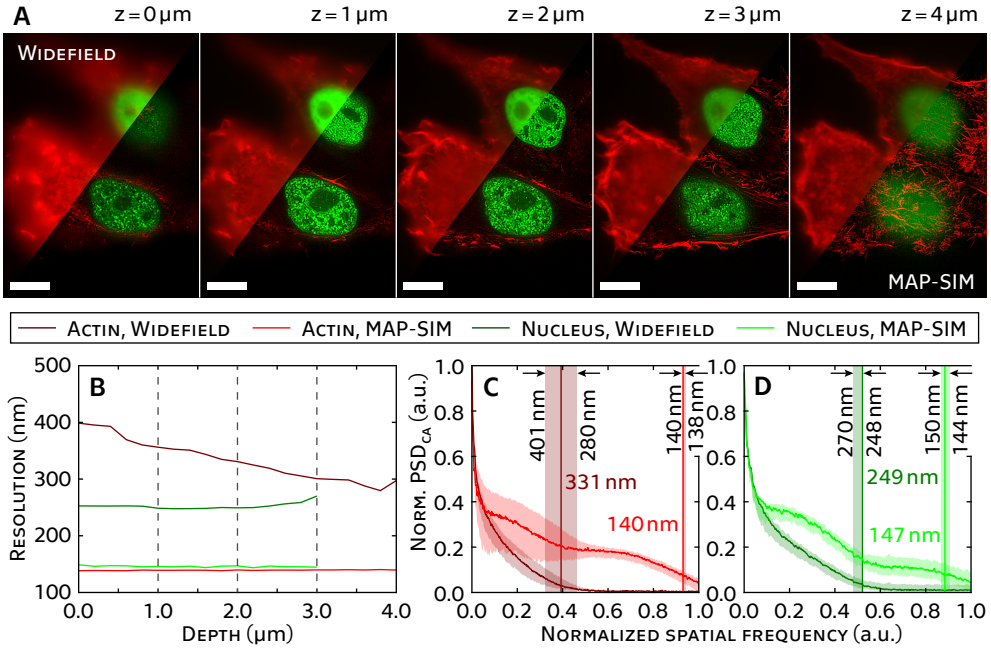

Figure 3.15: The results of PSD_{ca} measurement on the 3D image stack of the HEP-G2 cell (**SIM data 4** in the Section 2.2) expressing actin (red) and nucleus (green). (A) Representative ROIs showing 5 z-planes with the step of 1 µm through the cell (dashed vertical lines in (B) mark individual z-planes). (B) The dependence of the resolution on the depth. The measurement was performed on each z-plane image of the 3D stack individually. The PSD_{ca} curves for all z-planes are shown in (C) and (D), where the transparent areas represent all PSD_{ca} curves across the 3D stack. Red and green (both bright and dark) curves show the PSD_{ca} of the z-plane equal to 2 µm (approximately the center of the cell). The spatial frequency is normalized by the sampling rate $f_s = 1/(2 \cdot pps) = 7.69\,\mu m^{-1}$, where $pps = 65$ nm is a projected pixel size given by the physical size of the pixels on the camera sensor (6.50 µm) and the magnification of the objective lens in combination with the tube lens (100×). The scale bar is 10 µm.

SIM dataset 4 (from the Section 2.2) represents the volumetric imaging of the fixed cell. The whole 3D stack consists of 2D images acquired by scanning in the axial direction with the step of 200 nm. Actin (red) and nucleus (green) were acquired using LCOS-based SIM microscope running in multicolor imaging mode. The PSD_{ca} method gives the resolution estimate for each z-plane individually, resulting in the resolution dependence over the cell volume (see Fig. 3.15B). Figure 3.15A shows images of 5 z-planes (both Widefield and MAP-SIM reconstruction) in the range of 4 µm. These z-planes are marked in the Fig. 3.15B with dashed lines. Effective out-of-focus light suppression using MAP-SIM reconstruction can be observed in the cell images, which also results in the constant resolution enhancement close to the sampling of the image (∼140 nm for Actin and ∼145 nm for Nucleus).

An excellent example of the importance of the PSD_{ca} analysis of individual sectors in Fourier space separately is **SIM dataset 3** from the Section 2.2, where the SIM reconstruction was performed with the pattern of only one angle. Two dimensional

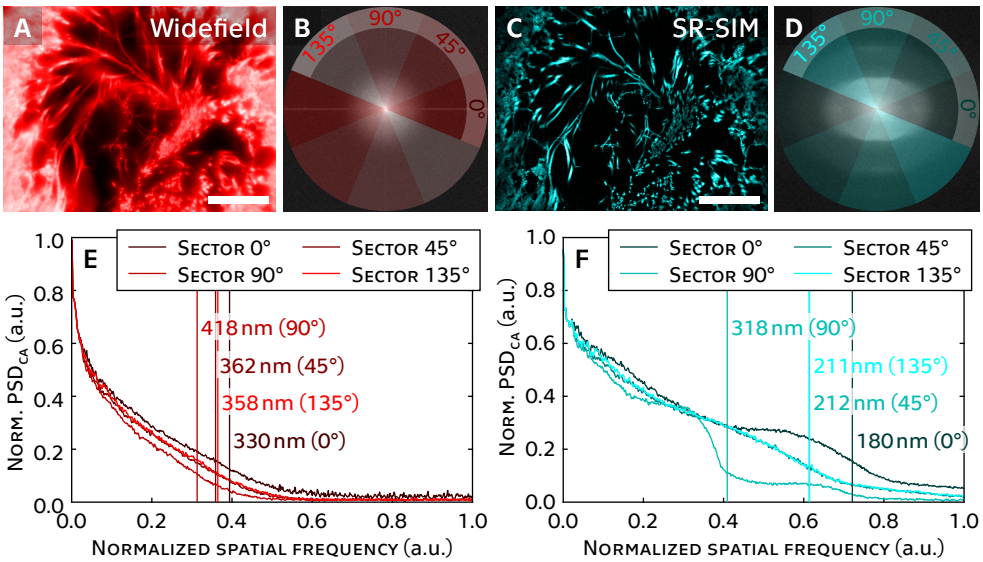

Figure 3.16: The results of the PSD_{ca} measurements on the sectioned rabbit testis stained with hematoxylin and eosin (**SIM data 3** in the Section 2.2). PSD_{ca} was measured in 4 sectors with the step of 45° to illustrate the measurement on uneven PSD. SR-SIM image was reconstructed using only one angle of illumination pattern resulting in resolution enhancement in one direction. The differences in the resolution in (E) are caused by the structure of the image, however, more significant difference in (F) is caused by the SR-SIM reconstruction. The spatial frequency is normalized by the sampling rate $f_s = 1/(2 \cdot pps) = 7.69\,\mu m^{-1}$, where $pps = 65$ nm is a projected pixel size given by the physical size of the pixels on the camera sensor (6.50 µm) and the magnification of the objective lens in combination with the tube lens (100×). The scale bars are 10 µm.

power spectral density in the Fig. 3.16D shows the resolution enhancement mostly in the horizontal direction while almost no enhancement in the vertical direction. Calculating the circular average over the full range would lead to the degradation of the actual maximum resolution of the image. Assuming an equal resolution limit over all angles in the widefield image (Fig. 3.16A), the resolution deviation (Fig. 3.16E) is mainly caused by the structure of the tissue sample.

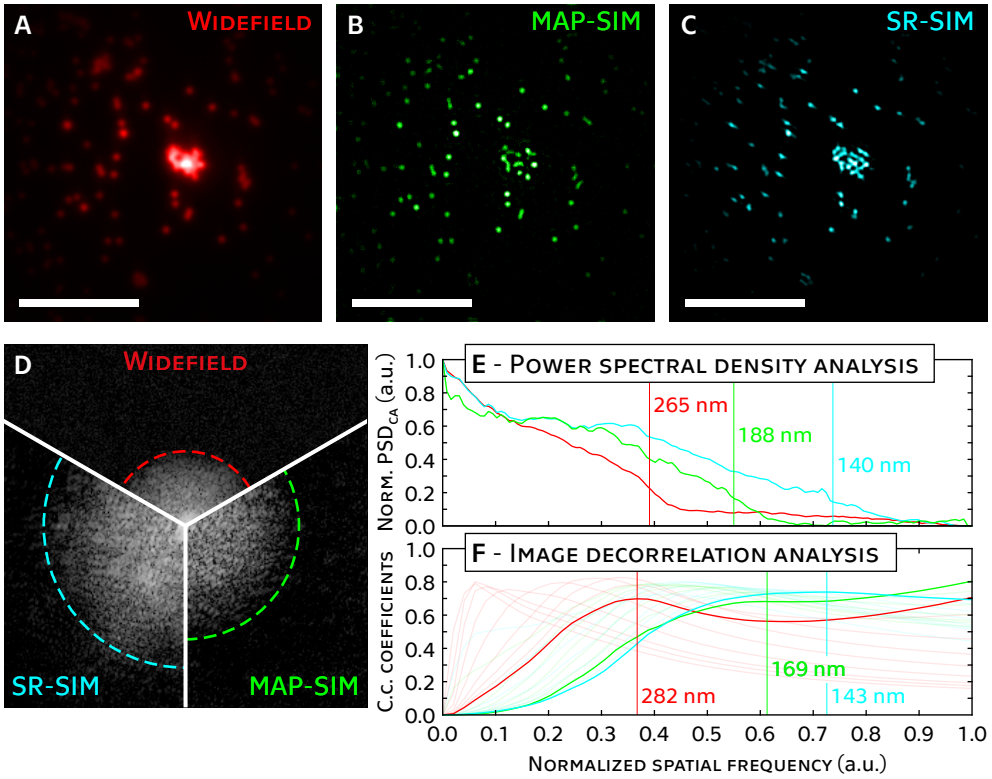

Figure 3.17: Comparison of PSD_{ca} with image decorrelation analysis. A 13.25 µm ×13.25 µm FOV of the widefield, MAP-SIM and SR-SIM reconstructed images (A)-(C), respectively. Determination of the global spatial resolution in image data using power spectral density analysis (PSD_{ca}) (E) and image decorrelation analysis (imDecorr[22]) (F). (D) Sections of the 2D Fourier transform of the images (A)-(C). The resolution limit of each imaging technique was determined with PSD_{ca} and the decorrelation method ((E) and (F)). The spatial frequency is normalized by the sampling rate $f_s = 1/(2 \cdot pps) = 9.66\,\mu m^{-1}$, where $pps = 51.75$ nm is a projected pixel size given by the physical size of the pixels on the camera sensor (3.45 µm) and the magnification of the objective lens in combination with the tube lens (66.666×). All resolution assessing methods indicate an improvement in the reconstructed SR-SIM images by almost a factor of 2. The scale bars are 5 µm.

Performance of the presented power spectral density analysis (PSD_{ca}) was compared with another recently published resolution assessment method based on image decorrelation analysis (imDecorr)[22]. The figure 3.17 shows the results of the resolution estimation in the image of fluorescence beads with the diameter of 200 nm. Beads were imaged with the *fiberSIM* microscope and reconstructed with SIM reconstruction tools *SIMToolbox*[55] and *fairSIM*[140] (for more details see Section *2.3: fiberSIM: Highly Compact SR-SIM Microscope Based on Fiber Optics*). In this case, both approaches, PSD_{ca} and imDecorr, assume the even resolution enhancement in all lateral directions (see Section 3.3.1), thus determine one representative resolution estimate. Despite different estimation approaches, both methods give very similar results. Almost two-fold enhancement in the resolution of the widefield fluorescence microscope can be achieved by using SR-SIM reconstruction (see Fig. 3.17).

4

Conclusions

The chapter summarizes the content of the dissertation, discusses achieved results, current developments, and future outlook with respect to ongoing projects.

Contents

Structured illumination microscopy is one of the most popular means in live cell biology to overcome the diffraction limit of a fluorescence microscope. Current commercially available super-resolution SIM (SR-SIM) microscopes are complex and often bulky systems whose high initial costs reduce their affordability. Therefore, a development of the compact low-cost SR-SIM systems making this technology available to every biological laboratory is essential.

Highly compact SR-SIM microscope based on fiber optics presented in this work shows the high potential of using fiber optics to dramatically reduce the size of the excitation part of the SIM microscope with high laser power efficiency. Further, custom-built SR-SIM systems requires suitable software able to successfully reconstruct the SIM data. Although there are open-source reconstruction tools available, e.g. *SIMToolbox*[e], or *fairSIM*[f], further software development is necessary.

Freely available SIM datasets are suitable for the software development and optimization of reconstruction and analysis tools. Therefore, we provide a fully documented SIM dataset[g] acquired with the custom-built SIM microscope based on the non-coherent illumination source and FLCOS microdisplay. Such a development of a compact SIM microscope system requires a robust method of quantitative evaluation of the reconstruction quality.

One of the most important metrics is the resolution gain of the SIM system. There are several conventional resolution assessment techniques that require specific resolution charts or fluorescence beads to evaluate the resolution limit of the microscope. However, assessing the resolution from a single image of a living cell is a more challenging task. Recently, a few novel approaches measuring the resolution from a single image were introduced, including the circular average power spectral density (PSD_{ca}) analysis presented in the thesis. The combination of freely available SIM reconstruction and analysis software enables more efficient development of custom-built SIM systems, making this super-resolution technique more affordable to any living cell biology laboratory.

4.1 Summary

The thesis is divided into three parts, covering the theoretical light microscopy background, followed by an overview of modern super-resolution microscopy techniques, including the current instrument development. The last part deals with the resolution assessment important to the quantitative evaluation of the resolution gain while using super-resolution microscopy.

[e] https://simtoolbox.github.io/
[f] https://www.fairsim.org/
[g] http://gigadb.org/dataset/100514

Chapter 1 introduces the fundamentals of light microscopy, especially fluorescence microscopy. Most common modern fluorescence microscopy techniques are discussed that lay the groundwork for all super-resolution microscopy approaches described in the following chapter. Furthermore, the diffraction limit, one of the most limiting factors in fluorescence microscopy, is detailed and followed by the

Chapter 2 introduces a general overview of the most common super-resolution techniques with the focus on structured illumination microscopy (SR-SIM). Detailed explanation of how SR-SIM technique recovers high resolution information beyond a diffraction limited widefield microscope is followed by a close look at the current development in the field of SIM microscopy. Freely available SIM datasets fully documented in this work are suitable for further software development of reconstruction and analysis tools as well as bring a benchmark for further development of custom-built SIM devices.

A novel approach for 2-beam structured illumination microscopy using an all-fiber optical implementation is presented in Chapter 2, Section 2.3. The highly compact design and flexibility of this SR-SIM device, while also maintaining the robustness required for interferometry, were achieved by using a microelectromechanical systems (MEMS) based fiber switch for rapid pattern angle switching in combination with 1×2 fiber splitters and a piezoelectric crystal for pattern phase shifting. By suitable selection of the telescope magnification, the pattern period can be flexibly adjusted from a coarse interference pattern up to the highest possible pattern frequency. A single pattern frequency was demonstrated as a proof-of-concept by utilizing very cost-efficient components, such as an industry-grade CMOS camera, which currently limits the maximum frame rate of the system.

The most common resolution assessment techniques in light microscopy, especially fluorescence microscopy, are introduced and discussed in Chapter 3. The chapter provides a broad overview of methods for determining the resolution limits of a microscope often used during the development or calibration of the system. Precisely manufactured testing charts or fluorescence beads are required to provide accurate resolution limit measurements using these methods. Therefore, a robust method for assessing the resolution directly from the image of a biological sample is essential in super-resolution microscopy. Such a method quantitatively determines the resolution gain of a particular SR imaging technique. The current development of such assessment methods is discussed in the chapter, including a detailed description of the circular average power spectral density (PSD_{ca}) analysis approach.

4.2 Contributions

The author's contributions to the field of super-resolution microscopy are listed below and put in the context of the aims stated in the introduction.

1. **Freely available SIM datasets**
   The datasets introduced in Chapter 2, Section 2.2 offer a suitable benchmark for the development SIM reconstruction algorithms to compare the results with those presented here, including the Bayesian method MAP-SIM. Furthermore, data may be utilized in other ways, e.g., single-particle tracking experiments in LAMP1-GFP cells (see Appendix B.2).

2. **Highly compact, low-cost illumination unit for SR-SIM**
   The proposed fiber optics-based super-resolution SIM equipment demonstrated in Chapter 2, Section 2.3 provides very promising imaging results indicating that this device could become the basis of a versatile "Plug&Play" illumination module with the capability of turning any conventional microscope body into a SR-SIM microscope.

3. **Performance evaluation based on spatial resolution assessment**
   An algorithm for assessing the resolution of a single image of a living cell based on circular average power spectral density (PSD_{ca}) analysis has been proposed. A detailed description of the method is included, followed by the comparison of the results obtained from resolution assessment using the proposed PSD_{ca} method and selected conventional approaches. A comprehensive overview of the most common conventional resolution assessment methods used in light microscopy, discussed in Chapter 3, may help with the choice of the proper method for a particular application.

4.3 Future work

The *fiberSIM* approach allows for the rather straightforward realization of multi-color SIM imaging in the future. Currently, the next generation of the *fiberSIM* device is under development, allowing the user to easily change the illumination pattern line spacing, thus the resolution enhancement factor up to TIRF mode. Furthermore, adding a center illumination beam to the current 2D *fiberSIM* turns the new device into the 3D SR-SIM system.

Broad overview of resolution assessment methods, including circular average power spectral density (PSD_{ca}) analysis, lies the base to create a complex set of functions suitable for resolution assessment in structured illumination microscopy. Further analysis of the reconstruction quality, such as quantitative determination of the most common SIM reconstruction artifacts can provide an essential feedback in the development of a custom-built SIM system. Implementation of these analysis functions can provide a comprehensive toolbox to complement existing open-source SIM reconstruction means *SIMToolbox*[h].

[h] https://simtoolbox.github.io/

A

Equipment and Materials

List of major optical components, optomechanical components, electronics, and chemicals used in this work.

Table A.1: Table of optical components, optomechanical components, and electronics listed in the work excluding standard lenses and mirrors. Sorted alphabetically by the item name.

Item	Part number	Producer	Description
AU	Uno Rev3	Arduino	An open-source microcontroller board based on the Microchip ATmega328P microcontroller
BPF1	ET460/36m	Chroma	Band pass filter, center wavelength of 460 nm, width 36 nm
BPF2	ET473/24m	Chroma	Band pass filter, center wavelength of 473 nm, width 24 nm
BPF3	ET525/20m	Chroma	Band pass filter, center wavelength of 525 nm, width 20 nm
BPF4	ET546/10x	Chroma	Band pass filter, center wavelength of 546 nm, width 10 nm
BPF5	ET625/30m	Chroma	Band pass filter, center wavelength of 625 nm, width 30 nm
BPF5	ET650/45x	Chroma	Band pass filter, center wavelength of 650 nm, width 45 nm
LDM1	T505lpxr	Chroma	Low pass dichroic mirror, edge wavelength 505 nm
LDM2	T600lpxr	Chroma	Low pass dichroic mirror, edge wavelength of 600 nm

Continued on next page

Table A.1 – continued from previous page

Item	Part number	Producer	Description
LDM3	FF538-FDI01	Semrock	Low pass dichroic mirror, edge wavelength of 538 nm
Cam1	Neo 5.5	Andor	Scientific CMOS camera
Cam2	Zyla 4.2+	Andor	Scientific CMOS camera
Cam3	Edge 5.5	PCO	Scientific CMOS camera
Cam4	UI-3270CP	IDS	Industrial CMOS camera
FLCOS	SXGA-3DM	ForthDD	Fast switching reflective SLM
FOC	TW470R5F1	Thorlabs	1×2 wideband fiber optic coupler, 50:50 split ratio
FPC	CPC900	Thorlabs	In-line fiber optic polarization controller
FS	SN1x4-9N	Sercalo	Fast opto-mechanical switch based on micromechanical mirrors
HWP	AHWP3	BVO	VIS achromatic half-wave retarder
K-CUBE	KPZ101	Thorlabs	K-Cube piezo controller
LED1	LP-54	Luminus	Monochromatic high power LED
LED2	LP-120	Luminus	Monochromatic high power LED
MS1	IX71	Olympus	Inverted microscope system
MS2	IX83	Olympus	Inverted microscope system
MS3	DMi8	Leica	Inverted microscope system
Obj1	PlanApo 60×/1.45	Olympus	Apochromat oil objective lens
Obj2	UPlanApo 100×/1.50	Olympus	Apochromat oil objective lens for super-resolution
Obj3	UPlanSApo 100×/1.4	Olympus	Super apochromat oil objective lens
Obj4	UPlanFLN 100×/1.3	Olympus	Semi-apochromat oil objective lens
Obj5	UPlanFLN 40×/0.75	Olympus	Semi-apochromat air/dry objective lens
Obj6	HCX PLAPO TIRF 100×/1.47	Leica	Apochromat TIRF oil objective lens

Continued on next page

Table A.1 – continued from previous page

Item	Part number	Producer	Description
PC	PA4GEH5W	Thorlabs	Piezo chip, 150 V, 2 µm displacement, $7 \times 7 \times 2$ mm
PS	TPS002	Thorlabs	± 15 V/5 V power supply unit for K-Cube piezo controller
SiDET	DET10A	Thorlabs	Si detector, wavelength range 200-1100 nm, 1 ns rise time

Table A.2: Table of chemicals mentioned in the thesis. Sorted alphabetically by the item name.

Item	Description
Alexa Fluor™ 488	Green-fluorescent dye with excitation of 488 nm
Atto 565	A fluorescent label belonging to the class of rhodamine dyes with excitation in the range 545-575 nm
Eosin	Red fluorescent dye that is a bromine derivative of fluorescein
Fetal bovine serum	A byproduct of harvesting cattle for the meatpacking industry used as a supplement to basal growth medium in cell culture applications
Hematoxylin	Naturally derived dye extracted from heartwood of the logwood tree
LAMP1-GFP	Fusion construct of lysosomal associated membrane protein 1 and green fluorescent protein
MitoTracker Red CMXRos	Red-fluorescent dye that stains mitochondria in live cells
Mowiol 4-88	Water soluble hydrocolloid mucoadhesive based on polyvinyl alcohol used as an embedding medium for preserving stained cell dishes
Paraformaldehyde	Formaldehyde polymer used for applications requiring a formaldehyde solution without stabilising additives

Continued on next page

Table A.2 – continued from previous page

Item	Description
PBS	Phosphate-buffered saline is a balanced salt solution providing an environment that helps to maintain the structural and physiological integrity of cells
Penicillin, streptomycin, and L-glutamate	Antibiotics used to prevent bacterial contamination in cell cultures due to their effective combined action against gram-positive and gram-negative bacteria
Phalloidin	Bicyclic peptide commonly used in imaging applications to selectively label F-actin in cells
Triton X-100	Detergent used in laboratories to permeabilize the membranes of living cells

B

Live Cell MAP-SIM

B.1 OS-SIM and MAP-SIM

In this section, the combination of the optical sectioning SIM (OS-SIM) with the maximum a posteriori probability SIM (MAP-SIM) is described in detail.

B.1.1 Optical Sectioning SIM

Several data processing methods are possible for generating optically sectioned images from SIM data (OS-SIM)[98,141]. The most familiar implementation of this technique was introduced in 1997 by Mark Neil[15]. Their method works by projecting a line illumination pattern onto a sample, followed by the acquisition of a set of three widefield images with the pattern shifted by relative spatial phases 0, $2\pi/3$, and $4\pi/3$. An optically sectioned image can be recovered computationally as

$$I_{OS-SIM} = \left[(I_1 - I_2)^2 + (I_1 - I_3)^2 + (I_2 - I_3)^2\right]^{1/2}, \tag{B.1}$$

where I_{OS-SIM} is optically sectioned image, and I_1, I_2, and I_3 are the three images acquired with different pattern positions (sometimes referred as *square law method*). If the sum of the individual SIM patterns results in homogeneous illumination, as is the case in FLCOS based SIM setups, a widefield image can be recovered from SIM data as an average of all images:

$$I_{Widefield} = \frac{1}{N}\sum_{n=1}^{N} I_n. \tag{B.2}$$

This is the approach of generating the Widefield images in the thesis.

In this study, a method known as homodyne detection[15,98,141] has been used for

optical sectioning SIM.

$$I_{OS-SIM} = \left| \sum_{n=1}^{N} I_n exp\left(2\pi i \frac{n}{N}\right) \right|. \tag{B.3}$$

It was previously shown that this processing method offers results with better optical sectioning than the square law method of Eq. (B.2)[98].

B.1.2 MAXIMUM A POSTERIORI PROBABILITY ESTIMATION SIM

Image acquisition in structured illumination microscopy for SIM with maximum a posteriori probability estimation can be described as[54]

$$\boldsymbol{y}_k = HM_k\boldsymbol{x} + \boldsymbol{n}_k, \tag{B.4}$$

where M_k represents the $k-th$ illumination pattern, $\boldsymbol{y}_k$ denotes a low-resolution (LR) image acquired using the $k-th$ illumination pattern, $\boldsymbol{x}$ is an unknown, high-resolution (HR) image, and $\boldsymbol{n}_k$ is additive noise. H is a matrix describing the convolution between the HR image and the point spread function (PSF) of the system. The position of the illumination patterns in the camera images were determined using a calibrated camera according to our previous work[98]. The PSF is represented as an Airy disk, which Fourier transform leads to an optical transfer function (OTF) of the form[112]

$$\mathrm{OTF}(\boldsymbol{f}) = \frac{1}{\pi}\left[2cos^{-1}\left(\frac{\boldsymbol{f}}{f_c}\right) - sin\left(2cos^{-1}\left(\frac{\boldsymbol{f}}{f_c}\right)\right)\right], \tag{B.5}$$

where $\boldsymbol{f}$ is the spatial frequency. The cut-off frequency f_c is estimated by calculating the radial average of the power spectral density (PSD) of a Widefield image of 100 nm fluorescent beads.

Using a Bayesian approach[54,89,90,142–144], high-resolution image estimation can be expressed as a minimization of a cost function according to

$$\boldsymbol{x}_{HR-MAP} = \arg\min_{x}\left[\sum_{k=1}^{K} \|\boldsymbol{y}_k - HM_k\boldsymbol{x}\|^2 + \lambda\Gamma(\boldsymbol{x})\right]. \tag{B.6}$$

The cost function in Eq. (B.6) consists of two terms. The first term describes the mean square error between the estimated HR image and the observed LR images. The second term is a regularization term. To ensure positivity and promote a smoothness condition on the HR image, algorithm relies on quadratic regularization composed of finite difference approximations of the first order derivative at each pixel location[145]

$$\Gamma(\boldsymbol{x}) = \sum_i \left[(\Delta_h\boldsymbol{x})_i^2 + (\Delta_v\boldsymbol{x})_i^2\right], \tag{B.7}$$

where Δ_h and Δ_v are the finite difference operators along the horizontal and vertical direction of an image, respectively, and $(\cdot)_i$ denotes the $i-th$ element of a vector. The

contribution of $\Gamma(\boldsymbol{x})$ is controlled by the parameter λ a small positive constant defining the strength of the regularization (typically $\lambda = 0.01$). Algorithm solves Eq. (B.6) using gradient descent methods.

B.1.3 Spectral Merging

MAP estimation of high resolution images obtained with structured illumination enables reconstruction of high resolution images (HR-MAP) with details unresolvable in a widefield microscope. However, MAP estimation as described above does not suppress out of focus light. On the other hand, the homodyne detection method used in the optical sectioning SIM (OS-SIM)[15,98]

$$I_{OS-SIM} = \boldsymbol{x}_{LR-HOM} = \left| \sum_{k=1}^{K} \boldsymbol{y}_k exp\left(2\pi i \frac{k}{K}\right) \right| \tag{B.8}$$

provides images (LR-HOM) with optical sectioning but with only a slight improvement in lateral resolution. Noting that the unwanted out of focus light is dominant at low spatial frequencies, MAP-SIM algorithm merges the LR-HOM and HR-MAP images in the frequency domain to obtain the final HR image (MAP-SIM). Frequency domain Gaussian low pass filtering is applied to the LR-HOM image and a complementary high pass filter is applied to the HR-MAP image. Weighting scheme used in the spectral merging can be described by

$$\begin{aligned} \boldsymbol{x}_{MAP-SIM} = \mathcal{F}^{-1}\Bigg\{ & (1-\beta)\,\mathcal{F}\{\boldsymbol{x}_{LR-HOM}\}\, exp\left(-\frac{\boldsymbol{f}^2}{2\sigma^2}\right) \\ & + \beta \mathcal{F}\{\boldsymbol{x}_{HR-MAP}\}\left(1 - exp\left(-\frac{\boldsymbol{f}^2}{2\sigma^2}\right)\right)\Bigg\}, \end{aligned} \tag{B.9}$$

where $\mathcal{F}, \mathcal{F}^{-1}$ denotes the Fourier transform operator and its inverse, respectively. $\boldsymbol{f}$ is the spatial frequency, σ is the standard deviation of the Gaussian filter, and β is a

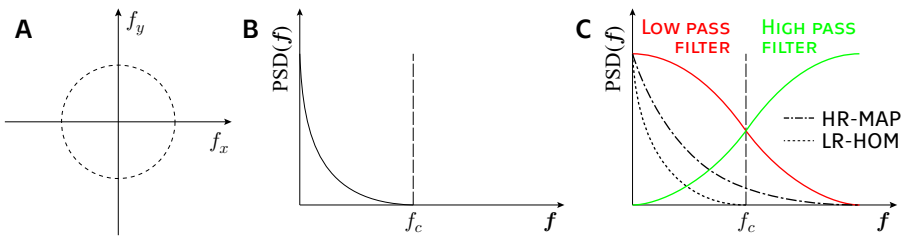

Figure A.1: Schematic of spectral merging step in MAP-SIM reconstruction algorithm. (A) Spatial frequencies in Fourier space, where f_c is the cut off frequency for a widefield microscope. (B) Power spectral density (PSD) in relation to the spatial frequency. (C) Blending frequency spectra of high resolution MAP (HR-MAP) estimation and the homodyne detection (LR-HOM) using low and high pass filters.

weighting coefficient (usually $\beta = 0.85$). A circularly symmetric cosine bell apodizing function is used to shape the final MAP-SIM spectrum before the final inverse Fourier transform. The spectral merging method is shown schematically in the Fig. A.1.

B.2 Example of Data Re-use

Using the optical sectioning effect of SIM allows tracking of low signal to background ratio particles in LAMP1-GFP cells. Single particle tracking (SPT) is a computer enhanced microscopy method used to track the motion of biological molecules or vesicles[146–148]. In SPT, a particle trajectory is obtained from position coordinates over a series of time steps. There are three basic steps in single particle tracking analysis[149]. The first is detection of the particles in the raw data. This may be regarded as segmentation or feature detection. The second step is localization of the particle, usually accomplished by fitting a small region of interest (7×7 pixels in the experiment presented here) to a two-dimensional Gaussian function. The third step is to link the localizations together from one frame to the next to create a particle trajectory which is as long as possible. These three steps combine to determine whether a particle can be successfully tracked. If a particle is not detected in every frame through the sequence, the trajectory will be truncated at the point where the particle was lost. MAP-SIM

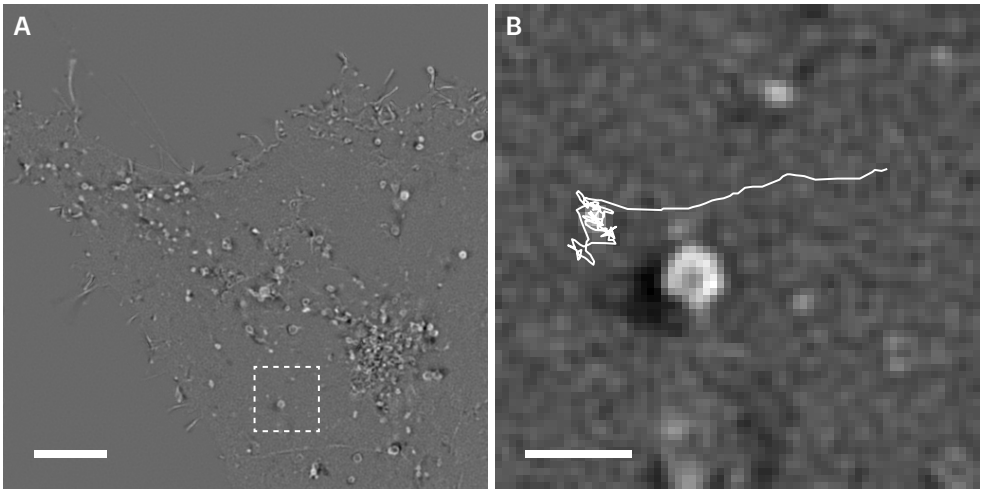

Figure A.2: Example of the single-particle tracking in LAMP1-GFP cell. (A) MAP-SIM image from Fig. 2.8C after subtraction of the average of the stack of images. (B) LAMP1-GFP particle trajectory (132 frames) within the boxed region in (A). The particle exhibits confined diffusion followed by directed movement. The scale bar is 5 µm in (A) and 1 µm in (B).

offers very high optical sectioning ability[54]. Because of this, the signal to background ratio (SBR) of the particles is higher, and the particles are thereby much easier to detect in the images. Single particle tracking algorithm[150] used in this work is state of the art, however, in this particular case, it is unable to detect dim, faster moving particles in the widefield data consistently enough to be able to build a trajectory longer than a few frames. However, using MAP-SIM allows to successfully track these particles.

In this experiment, the trajectories of single LAMP1-GFP particles (lysosomes, endosomes, or other vesicles containing LAMP1-GFP), were obtained by a SPT algorithm implemented in MATLAB[150]. The intensity average of the reconstructed Widefield or MAP-SIM image stack was subtracted from each individual image within the stack to reduce sCMOS camera-induced fixed pattern noise and for feature enhancement (shown in Fig. A.2A). Single particle trajectories were determined from the processed data sets by selecting the initial starting particle coordinates by hand. Gaussian fitting of the imaged particle, and building trajectories from coordinates based on determining the probability of finding a diffusing particle in two dimensions at a given distance from its starting point after a given time[150]. The particles were tracked for at least 12 up to a maximum of 132 time steps of 250 ms each. Fig. A.2B shows an example trajectory of a tracked particle. After this process of building uninterrupted trajectories,

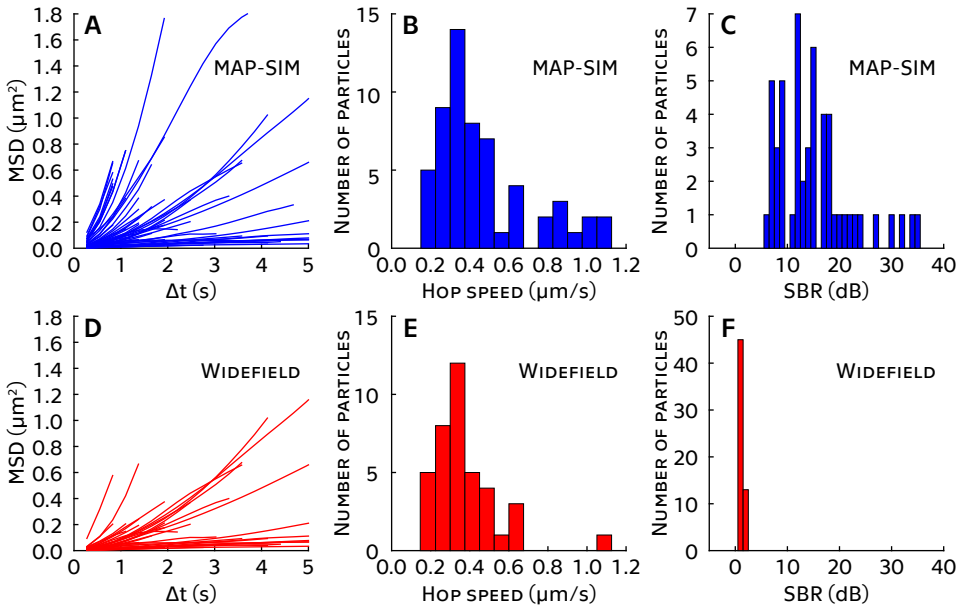

Figure A.3: MSD plot of LAMP1-GFP particle trajectories obtained from MAP-SIM (A - 60 trajectories) and Widefield (D - 39 trajectories) image sequence. (B) and (E) show histograms of particle hop speeds computed for the average distance traveled during the time lag $\Delta t = 250$ ms. (C) and (F) are histograms of the signal to background ratio calculated for each particle that was tracked in the MAP-SIM (C) and Widefield (F) data.

the mean-squared displacement (MSD), was calculated. The MSD is a measure of the average speed a particle travels and is calculated for each time difference Δt in the track. The MSD plot was computed up to $n\Delta t < 1/4$ of the total number of acquired time frames, where n is the number of available displacements of a given duration $n\Delta t$ in the track record[146,150].

In total, 60 LAMP1-GFP particles were tracked in the MAP-SIM image sequence taken from Fig. 2.8 presented in the Chapter 2, section 2.2. Figure A.3A describes the corresponding MSD plots and Fig. A.3B shows a histogram of the number of particles with a given hop speed computed from the average distance traveled during the shortest lag time ($\Delta t = 250$ ms). The same experiment was performed in the widefield image sequence to track the same particles using the same initial particle coordinates and tracking algorithm. All algorithm settings were kept identical between the two data sets (MAP-SIM and Widefield) except for the size of the point spread function. Of the 60 particles tracked in MAP-SIM, 39 particles (65%) were successfully tracked in the Widefield data. Figure A.3D depicts the corresponding MSD plots obtained from the Widefield single particle trajectories and Fig. A.3E shows a histogram of the number of particles with a given hop speed. Comparing the MAP-SIM MSD plot, Fig. A.3A, to the Widefield MSD plot, Fig. A.3D, it is evident that fast moving LAMP1-GFP particles, represented by steeper MSD curves, cannot be tracked as successfully in the Widefield data. As noted above, MAP-SIM increased the SBR of the particles we attempted to track. This is shown in Figs. A.3C and A.3F. To determine the SBR of the particles, a region of interest (ROI) around each particle (9×9 pixels) was evaluated. The local SBR was determined as the ratio between the maximum (average of the 5% of the highest pixel values) and minimum (average of the 5% of the lowest pixel values) in the region. To analyze single particle tracking (SPT) experiments, we used custom routines[150,A8] in MATLAB using DIPimage[151].

B.3 How Exposure Time Affects Resolution

As noted in the main part of the thesis, the FLCOS microdisplay (and vendor-supplied microdisplay-timing program) used in the SIM setup can display an illumination pattern and switch to the next pattern in the sequence in 1.14 ms. This allows unprocessed SIM images to be acquired at rates of approximately 875 Hz. An exposure time of about 1 ms would be needed to achieve this imaging rate. However, such rapid imaging is not useful if the reconstructed SIM images are of poor quality, for example if they suffer from low signal-to-noise ratios (SNR). Specifying the fastest possible acquisition rate is thus inadequate without consideration of the resolution and SNR of the results.

Figure A.4 demonstrates the effect of varying the camera exposure time on $\mathrm{PSD}_{\mathrm{ca}}$ and thus on the spatial resolution. We imaged LAMP1-GFP cells and varied the camera exposure time from 10 ms to 100 ms per one SIM sub-image. Low signal-to-noise

ratios (in this case due to a short exposure time) causes a loss of fine details and thus a reduction in effective resolution as estimated by power spectral density analysis[A8]. These findings are not surprising, but the relationship between SNR (and therefore exposure times and usable imaging rates) and image resolution is typically not discussed in the SIM literature. This effect sometimes leads to very high noise and lower effective resolution when trying to push SIM imaging rates.

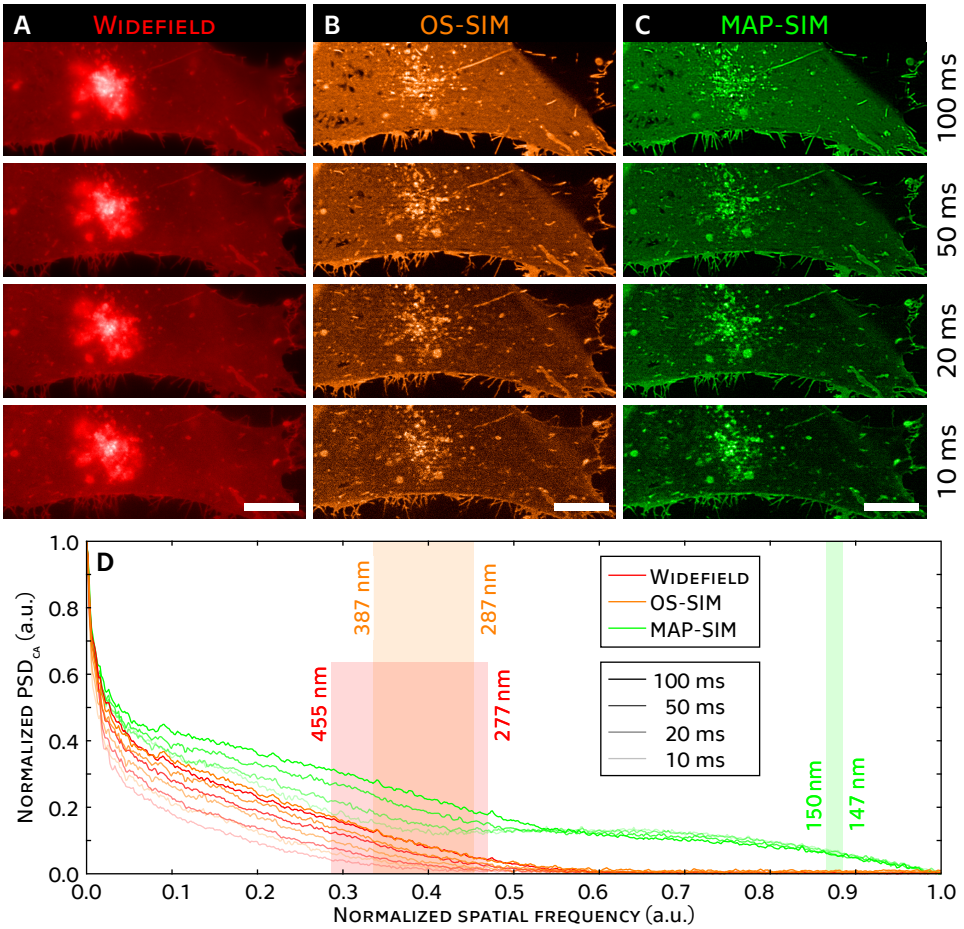

Figure A.4: Resolution assessment in images acquired with different exposure times for Widefield, OS-SIM, and MAP-SIM. A lower signal-to-noise ratio (SNR), due to the shorter exposure time, leads to a loss of the fine details, thus a reduction in the resolution. The scale bars are 5 µm.

Bibliography

1. Schermelleh, L. *et al.* Super-resolution microscopy demystified. *Nature Cell Biology* **21,** 72–84. ISSN: 1476-4679. https://doi.org/10.1038/s41556-018-0251-8 (2019).
2. Plášek, J. Superresolution in Optical Microscopy. The 2014 Nobel Prize for Chemistry. *Proceedings in Mathematics, Physics and Astronomy* **60,** 19–38. ISSN: 0032-2423 (2015).
3. Murphy, D. B. & Davidson, M. W. *Fundamentals of Light Microscopy and Electronic Imaging* Second, 1–552. ISBN: 978-0-47-169214-0. https://doi.org/10.1002/9781118382905 (John Wiley & Sons, Inc., Hoboken, NJ, USA, 2012).
4. Betzig, E. *et al.* Imaging Intracellular Fluorescent Proteins at Nanometer Resolution. *Science* **313,** 1642–1645. ISSN: 0036-8075. https://doi.org/10.1126/science.1127344 (2006).
5. Hess, S. T., Girirajan, T. P. & Mason, M. D. Ultra-High Resolution Imaging by Fluorescence Photoactivation Localization Microscopy. *Biophysical Journal* **91,** 4258–4272. ISSN: 0006-3495. https://doi.org/10.1529/biophysj.106.091116 (2006).
6. Rust, M. J., Bates, M. & Zhuang, X. Sub-diffraction-limit imaging by stochastic optical reconstruction microscopy (STORM). *Nature Methods* **3,** 793–796. ISSN: 1548-7091. https://doi.org/10.1038/nmeth929 (2006).
7. Heilemann, M. *et al.* Subdiffraction-Resolution Fluorescence Imaging with Conventional Fluorescent Probes. *Angewandte Chemie International Edition* **47,** 6172–6176. ISSN: 1433-7851. https://doi.org/10.1002/anie.200802376 (2008).
8. Dertinger, T., Colyer, R., Iyer, G., Weiss, S. & Enderlein, J. Fast, background-free, 3D super-resolution optical fluctuation imaging (SOFI). *Proceedings of the National Academy of Sciences Dec 2009* **106,** 22287–22292. ISSN: 1091-6490. https://doi.org/10.1073/pnas.0907866106 (2009).
9. Geissbuehler, S. *et al.* Mapping molecular statistics with balanced super-resolution optical fluctuation imaging (bSOFI). *Optical Nanoscopy* **1,** 1–7. ISSN: 2192-2853. https://doi.org/10.1186/2192-2853-1-4 (2012).
10. Wegel, E. *et al.* Imaging cellular structures in super-resolution with SIM, STED and Localisation Microscopy: A practical comparison. *Scientific Reports* **6,** 1–13. ISSN: 2045-2322. https://doi.org/10.1038/srep27290 (2016).
11. Hell, S. W. & Wichmann, J. Breaking the diffraction resolution limit by stimulated emission: stimulated-emission-depletion fluorescence microscopy. *Optics Letters* **19,** 780–782. ISSN: 0146-9592. https://doi.org/10.1364/OL.19.000780 (1994).

12. Gustafsson, M. G. L. Surpassing the lateral resolution limit by a factor of two using structured illumination microscopy. SHORT COMMUNICATION. *Journal of Microscopy* **198,** 82–87. ISSN: 0022-2720. https://doi.org/10.1046/j.1365-2818.2000.00710.x (2000).

13. Gustafsson, M. G. L. Nonlinear structured-illumination microscopy: wide-field fluorescence imaging with theoretically unlimited resolution. *Proceedings of the National Academy of Sciences of the United States of America* **102,** 13081–13086. ISSN: 0027-8424. https://doi.org/10.1073/pnas.0406877102 (2005).

14. Gustafsson, M. G. L. *et al.* Three-dimensional resolution doubling in wide-field fluorescence microscopy by structured illumination. *Biophysical Journal* **94,** 4957–4970. ISSN: 0006-3495. https://doi.org/10.1529/biophysj.107.120345 (2008).

15. Neil, M. A. A., Juškaitis, R. & Wilson, T. Method of obtaining optical sectioning by using structured light in a conventional microscope. *Optics Letters* **22,** 1905–1907. ISSN: 0146-9592. https://doi.org/10.1364/OL.22.001905 (1997).

16. Geissbuehler, S., Dellagiacoma, C. & Lasser, T. Comparison between SOFI and STORM. *Biomedical Optics Express* **2,** 408–420. ISSN: 2156-7085. https://doi.org/10.1364/BOE.2.000408 (2011).

17. Koho, S. *et al.* Fourier ring correlation simplifies image restoration in fluorescence microscopy. *Nature Communications* **10,** 1–9. ISSN: 2041-1723. https://doi.org/10.1038/s41467-019-11024-z (2019).

18. Banterle, N., Bui, K. H., Lemke, E. A. & Beck, M. Fourier ring correlation as a resolution criterion for super-resolution microscopy. *Journal of Structural Biology* **183,** 363–367. ISSN: 10478477. https://doi.org/10.1016/j.jsb.2013.05.004 (2013).

19. Van Heel, M. & Schatz, M. Fourier shell correlation threshold criteria. *Journal of Structural Biology* **151,** 250–262. ISSN: 10478477. https://doi.org/10.1016/j.jsb.2005.05.009 (2005).

20. Laine, R. F. *et al.* NanoJ: A high-performance open-source super-resolution microscopy toolbox. *Journal of Physics D: Applied Physics* **52,** 1–10. ISSN: 1361-6463. https://doi.org/10.1088/1361-6463/ab0261 (2019).

21. Culley, S. *et al.* Quantitative mapping and minimization of super-resolution optical imaging artifacts. *Nature Methods* **15,** 263–266. ISSN: 1548-7091. https://doi.org/10.1038/nmeth.4605 (2018).

22. Descloux, A., Grußmayer, K. S. & Radenovic, A. Parameter-free image resolution estimation based on decorrelation analysis. *Nature Methods* **16,** 819–824. ISSN: 1548-7091. https://doi.org/10.1038/s41592-019-0515-7 (2019).

23. Abbe, E. Beiträge zur Theorie des Mikroskops und der mikroskopischen Wahrnehmung. *Archiv für Mikroskopische Anatomie* **9,** 413–468. ISSN: 0176-7364. https://doi.org/10.1007/BF02956173 (1873).

24. Mulvey, T. in *Advances in Imaging and Electron Physics* 259–283 (1995). ISBN: 0120147335. https://doi.org/10.1016/S1076-5670(08)70113-7.

25. De Jonge, N. & Peckys, D. B. Live cell electron microscopy is probably impossible. *ACS Nano* **10,** 9061–9063. ISSN: 1936-086X. https://doi.org/10.1021/acsnano.6b02809 (2016).

26. Park, J. *et al.* Direct observation of wet biological samples by graphene liquid cell transmission electron microscopy. *Nano Letters* **15,** 4737–4744. ISSN: 1530-6992. https://doi.org/10.1021/acs.nanolett.5b01636 (2015).

27. Peckys, D. B., Mazur, P., Gould, K. L. & De Jonge, N. Fully hydrated yeast cells imaged with electron microscopy. *Biophysical Journal* **100,** 2522–2529. ISSN: 0006-3495. https://doi.org/10.1016/j.bpj.2011.03.045 (2011).

28. Weiss, P. S. Nobel Prizes for Super-Resolution Imaging. *ACS Nano* **8,** 9689–9690. ISSN: 1936-0851. https://doi.org/10.1021/nn505967q (2014).

29. Saleh, B. E. A. & Teich, M. C. in *Fundamentals of Photonics* 1–40 (John Wiley & Sons, Inc., New York, USA, 1991). ISBN: 9780471213741. https://doi.org/10.1002/0471213748.ch1.

30. Fiolka, R., Belyaev, Y., Ewers, H. & Stemmer, A. Even illumination in total internal reflection fluorescence microscopy using laser light. *Microscopy Research and Technique* **71,** 45–50. ISSN: 1059-910X. https://doi.org/10.1002/jemt.20527 (2008).

31. Song, L., Hennink, E., Young, I. T. & Tanke, H. J. Photobleaching kinetics of fluorescein in quantitative fluorescence microscopy. *Biophysical Journal* **68,** 2588–2600. ISSN: 0006-3495. https://doi.org/10.1016/S0006-3495(95)80442-X (1995).

32. Keller, P. J. *et al.* Fast, high-contrast imaging of animal development with scanned light sheet–based structured-illumination microscopy. *Nature Methods* **7,** 637–642. ISSN: 1548-7091. https://doi.org/10.1038/nmeth.1476 (2010).

33. Chang, B.-J., Perez Meza, V. D. & Stelzer, E. H. K. csiLSFM combines light-sheet fluorescence microscopy and coherent structured illumination for a lateral resolution below 100 nm. *Proceedings of the National Academy of Sciences of the United States of America* **114,** 4869–4874. ISSN: 0027-8424. https://doi.org/10.1073/pnas.1609278114 (2017).

34. Ren, Y.-X. *et al.* Parallelized volumetric fluorescence microscopy with a reconfigurable coded incoherent light-sheet array. *Light: Science & Applications* **9,** 1–11. ISSN: 2047-7538. https://doi.org/10.1038/s41377-020-0245-8 (2020).

35. Olarte, O. E., Andilla, J., Artigas, D. & Loza-Alvarez, P. Decoupled illumination detection in light sheet microscopy for fast volumetric imaging. *Optica* **2,** 702–705. ISSN: 2334-2536. https://doi.org/10.1364/OPTICA.2.000702 (2015).

36. Meddens, M. B. M. *et al.* Single objective light-sheet microscopy for high-speed whole-cell 3D super-resolution. *Biomedical Optics Express* **7,** 2219–2236. ISSN: 2156-7085. https://doi.org/10.1364/BOE.7.002219 (2016).

37. Hinsdale, T. A., Stallinga, S. & Rieger, B. High-speed multicolor structured illumination microscopy using a hexagonal single mode fiber array. *Biomedical Optics Express* **12,** 1–8. ISSN: 2156-7085. https://doi.org/10.1364/BOE.416546 (2021).

38. Webb, R. H. Confocal optical microscopy. *Reports on Progress in Physics* **59,** 427–471. ISSN: 0034-4885. https://doi.org/10.1088/0034-4885/59/3/003 (1996).

39. Badon, A. *et al.* Video-rate large-scale imaging with Multi-Z confocal microscopy. *Optica* **6,** 389–395. ISSN: 2334-2536. https://doi.org/10.1364/OPTICA.6.000389 (2019).

40. Duocastella, M., Vicidomini, G. & Diaspro, A. Simultaneous multiplane confocal microscopy using acoustic tunable lenses. *Optics Express* **22,** 19293–19301. ISSN: 1094-4087. https://doi.org/10.1364/OE.22.019293 (2014).

41. Chia, C.-M., Vyas, S., Wu, T.-H., Yeh, J. A. & Luo, Y. Multi-plane confocal microscopy with multiplexed volume holographic gratings [Invited]. *Applied Optics* **60,** B141–B150. ISSN: 1559-128X. https://doi.org/10.1364/AO.416364 (2021).

42. Tsang, J.-M. *et al.* Fast, multiplane line-scan confocal microscopy using axially distributed slits. *Biomedical Optics Express* **12,** 1339–1350. ISSN: 2156-7085. https://doi.org/10.1364/BOE.417286 (2021).

43. Xiao, G. Q., Corle, T. R. & Kino, G. S. Real-time confocal scanning optical microscope. *Applied Physics Letters* **53,** 716–718. ISSN: 0003-6951. https://doi.org/10.1063/1.99814 (1988).

44. Oreopoulos, J., Berman, R. & Browne, M. in *Methods in Cell Biology* 153–175 (Academic Press Inc., 2014). https://doi.org/10.1016/B978-0-12-420138-5.00009-4.

45. Gräf, R., Rietdorf, J. & Zimmermann, T. in *Advances in Biochemical Engineering/Biotechnology* 57–75 (Springer, Berlin, Heidelberg, 2005). ISBN: 3540236988. https://doi.org/10.1007/b102210.

46. Inoué, S. & Inoué, T. in *Methods in Cell Biology* 70, 87–127 (Academic Press Inc., 2002). https://doi.org/10.1016/S0091-679X(02)70003-4.

47. Wang, E., Babbey, C. M. & Dunn, K. W. Performance comparison between the high-speed Yokogawa spinning disc confocal system and single-point scanning confocal systems. *Journal of Microscopy* **218,** 148–159. ISSN: 0022-2720. https://doi.org/10.1111/j.1365-2818.2005.01473.x (2005).

48. Mattheyses, A. L. & Axelrod, D. Direct measurement of the evanescent field profile produced by objective-based total internal reflection fluorescence. *Journal of Biomedical Optics* **11,** 014006–1. ISSN: 1083-3668. https://doi.org/10.1117/1.2161018 (2006).

49. Rayleigh, L. J. W. S. XXXI. Investigations in optics, with special reference to the spectroscope. *The London, Edinburgh, and Dublin Philosophical Magazine and Journal of Science* **8,** 261–274. ISSN: 1941-5982. https://doi.org/10.1080/14786447908639684 (1879).

50. Blom, H. & Widengren, J. Stimulated Emission Depletion Microscopy. *Chemical Reviews* **117,** 7377–7427. ISSN: 0009-2665. https://doi.org/10.1021/acs.chemrev.6b00653 (2017).

51. Latychevskaia, T. Lateral and axial resolution criteria in incoherent and coherent optics and holography, near- and far-field regimes. *Applied Optics* **58,** 3597–3603. ISSN: 1559-128X. https://doi.org/10.1364/AO.58.003597 (2019).

52. *PCO: pco.edge 5.5* 2021. https://www.pco.de/scientific-cameras/pcoedge-55/.

53. *IDS: UI-3270CP Rev. 2* 2021. https://en.ids-imaging.com/store/ui-3270cp-rev-2.html.

54. Lukeš, T. *et al.* Three-dimensional super-resolution structured illumination microscopy with maximum a posteriori probability image estimation. *Optics Express* **22,** 29805–29817. ISSN: 1094-4087. https://doi.org/10.1364/OE.22.029805 (2014).

55. Křížek, P., Lukeš, T., Ovesný, M., Fliegel, K. & Hagen, G. M. SIMToolbox: A MATLAB toolbox for structured illumination fluorescence microscopy. *Bioinformatics* **32,** 318–320. ISSN: 1460-2059. https://doi.org/10.1093/bioinformatics/btv576 (2016).

56. Hell, S. W. *et al.* The 2015 super-resolution microscopy roadmap. *Journal of Physics D: Applied Physics* **48,** 1–35. ISSN: 0022-3727. https://doi.org/10.1088/0022-3727/48/44/443001 (2015).

57. Whelan, D. R. & Bell, T. D. M. Image artifacts in Single Molecule Localization Microscopy: why optimization of sample preparation protocols matters. *Scientific Reports* **5,** 1–10. ISSN: 2045-2322. https://doi.org/10.1038/srep07924 (2015).

58. Demmerle, J., Wegel, E., Schermelleh, L. & Dobbie, I. M. Assessing resolution in super-resolution imaging. *Methods* **88,** 3–10. ISSN: 1046-2023. https://doi.org/10.1016/j.ymeth.2015.07.001 (2015).

59. Agarwal, A. K. *et al.* Role of tumor cell surface lysosome-associated membrane protein-1 (LAMP1) and its associated carbohydrates in lung metastasis. *Journal of Cancer Research and Clinical Oncology* **141,** 1563–1574. ISSN: 1432-1335. https://doi.org/10.1007/s00432-015-1917-2 (2015).

60. Xu, K., Zhong, G. & Zhuang, X. Actin, Spectrin, and Associated Proteins Form a Periodic Cytoskeletal Structure in Axons. *Science* **339,** 452–456. ISSN: 0036-8075. https://doi.org/10.1126/science.1232251 (2013).

61. Doksani, Y., Wu, J. Y., de Lange, T. & Zhuang, X. Super-Resolution Fluorescence Imaging of Telomeres Reveals TRF2-Dependent T-loop Formation. *Cell* **155,** 345–356. ISSN: 0092-8674. https://doi.org/10.1016/j.cell.2013.09.048 (2013).

62. Dani, A., Huang, B., Bergan, J., Dulac, C. & Zhuang, X. Superresolution Imaging of Chemical Synapses in the Brain. *Neuron* **68,** 843–856. ISSN: 08966273. https://doi.org/10.1016/j.neuron.2010.11.021 (2010).

63. Szymborska, A. *et al.* Nuclear Pore Scaffold Structure Analyzed by Super-Resolution Microscopy and Particle Averaging. *Science* **341,** 655–658. ISSN: 0036-8075. https://doi.org/10.1126/science.1240672 (2013).

64. Dertinger, T., Colyer, R., Vogel, R., Enderlein, J. & Weiss, S. Achieving increased resolution and more pixels with Superresolution Optical Fluctuation Imaging (SOFI). *Optics Express* **18,** 18875–18885. ISSN: 1094-4087. https://doi.org/10.1364/OE.18.018875 (2010).

65. Dedecker, P., Mo, G. C. H., Dertinger, T. & Zhang, J. Widely accessible method for superresolution fluorescence imaging of living systems. *Proceedings of the National Academy of Sciences of the United States of America* **109,** 10909–10914. ISSN: 1091-6490. https://doi.org/10.1073/pnas.1204917109 (2012).

66. Girsault, A. *et al.* SOFI Simulation Tool: A Software Package for Simulating and Testing Super-Resolution Optical Fluctuation Imaging. *PLOS One* **11** (ed Degtyar, V. E.) 1–13. ISSN: 1932-6203. https://doi.org/10.1371/journal.pone.0161602 (2016).

67. Watanabe, T. M., Fukui, S., Jin, T., Fujii, F. & Yanagida, T. Real-Time Nanoscopy by Using Blinking Enhanced Quantum Dots. *Biophysical Journal* **99,** L50–L52. ISSN: 0006-3495. https://doi.org/10.1016/j.bpj.2010.07.036 (2010).

68. Hell, S. W. Far-Field Optical Nanoscopy. *Science* **316,** 1153–1158. ISSN: 0036-8075. https://doi.org/10.1126/science.1137395 (2007).

69. Kner, P., Chhun, B. B., Griffis, E. R., Winoto, L. & Gustafsson, M. G. L. Super-resolution video microscopy of live cells by structured illumination. *Nature Methods* **6,** 339–342. ISSN: 1548-7105. https://doi.org/10.1038/nmeth.1324 (2009).

70. Heintzmann, R. & Huser, T. Super-Resolution Structured Illumination Microscopy. *Chemical Reviews* **117,** 13890–13908. ISSN: 0009-2665. https://doi.org/10.1021/acs.chemrev.7b00218 (2017).

71. Markwirth, A. *et al.* Video-rate multi-color structured illumination microscopy with simultaneous real-time reconstruction. *Nature Communications* **10,** 1–11. ISSN: 2041-1723. https://doi.org/10.1038/s41467-019-12165-x (2019).

72. Schermelleh, L. *et al.* Subdiffraction Multicolor Imaging of the Nuclear Periphery with 3D Structured Illumination Microscopy. *Science* **320,** 1332–1336. ISSN: 0036-8075. https://doi.org/10.1126/science.1156947 (2008).

73. Schlichenmeyer, T. C., Wang, M., Elfer, K. N. & Brown, J. Q. Video-rate structured illumination microscopy for high-throughput imaging of large tissue areas. *Biomedical Optics Express* **5,** 366–377. ISSN: 2156-7085. https://doi.org/10.1364/BOE.5.000366 (2014).

74. Sandmeyer, A. *et al.* Cost-Effective Live Cell Structured Illumination Microscopy with Video-Rate Imaging. *ACS Photonics* **8,** 1639–1648. ISSN: 2330-4022. https://doi.org/10.1021/acsphotonics.0c01937 (2021).

75. Heintzmann, R. & Cremer, C. G. *Laterally Modulated Excitation Microscopy: Improvement of resolution by using a diffraction grating* in *Optical Biopsies and Microscopic Techniques III* (eds Bigio, I. J., Schneckenburger, H., Slavik, J., Svanberg, K. & Viallet, P. M.) **3568** (SPIE, Stockholm, Sweden, 1999), 185–196. https://doi.org/10.1117/12.336833.

76. Hirvonen, L. M., Wicker, K., Mandula, O. & Heintzmann, R. Structured illumination microscopy of a living cell. *European Biophysics Journal* **38,** 807–812. ISSN: 0175-7571. https://doi.org/10.1007/s00249-009-0501-6 (2009).

77. Shao, L., Kner, P., Rego, E. H. & Gustafsson, M. G. L. Super-resolution 3D microscopy of live whole cells using structured illumination. *Nature Methods* **8,** 1044–1046. ISSN: 1548-7091. https://doi.org/10.1038/nmeth.1734 (2011).

78. Fiolka, R., Shao, L., Hesper Rego, E., Davidson, M. W. & Gustafsson, M. G. Time-lapse two-color 3D imaging of live cells with doubled resolution using structured illumination. *Proceedings of the National Academy of Sciences of the United States of America* **109,** 5311–5315. ISSN: 0027-8424. https://doi.org/10.1073/pnas.1119262109 (2012).

79. York, A. G. *et al.* Resolution doubling in live, multicellular organisms via multifocal structured illumination microscopy. *Nature Methods* **9,** 749–754. ISSN: 1548-7091. https://doi.org/10.1038/nmeth.2025 (2012).

80. Ingaramo, M. *et al.* Two-photon excitation improves multifocal structured illumination microscopy in thick scattering tissue. *Proceedings of the National Academy of Sciences of the United States of America* **111,** 5254–5259. ISSN: 1091-6490. https://doi.org/10.1073/pnas.1314447111 (2014).

81. York, A. G. *et al.* Instant super-resolution imaging in live cells and embryos via analog image processing. *Nature Methods* **10,** 1122–1126. ISSN: 1548-7091. https://doi.org/10.1038/nmeth.2687 (2013).

82. Schropp, M. & Uhl, R. Two-dimensional structured illumination microscopy. *Journal of Microscopy* **256,** 23–36. ISSN: 1365-2818. https://doi.org/10.1111/jmi.12154 (2014).

83. Schropp, M., Seebacher, C. & Uhl, R. XL-SIM: Extending Superresolution into Deeper Layers. *Photonics* **4,** 1–17. ISSN: 2304-6732. https://doi.org/10.3390/photonics4020033 (2017).

84. Planchon, T. A. *et al.* Rapid three-dimensional isotropic imaging of living cells using Bessel beam plane illumination. *Nature Methods* **8,** 417–423. ISSN: 1548-7091. https://doi.org/10.1038/nmeth.1586 (2011).

85. Gao, L. *et al.* Noninvasive Imaging beyond the Diffraction Limit of 3D Dynamics in Thickly Fluorescent Specimens. *Cell* **151,** 1370–1385. ISSN: 0092-8674. https://doi.org/10.1016/j.cell.2012.10.008 (2012).

86. Chen, B.-C. *et al.* Lattice light-sheet microscopy: Imaging molecules to embryos at high spatiotemporal resolution. *Science* **346,** 1257998–1. ISSN: 0036-8075. https://doi.org/10.1126/science.1257998 (2014).

87. Li, D. *et al.* Extended-resolution structured illumination imaging of endocytic and cytoskeletal dynamics. *Science* **349,** 3500–1. ISSN: 0036-8075. https://doi.org/10.1126/science.aab3500 (2015).

88. Dong, S., Nanda, P., Shiradkar, R., Guo, K. & Zheng, G. High-resolution fluorescence imaging via pattern-illuminated Fourier ptychography. *Optics Express* **22,** 20856–20870. ISSN: 1094-4087. https://doi.org/10.1364/OE.22.020856 (2014).

89. Orieux, F., Sepulveda, E., Loriette, V., Dubertret, B. & Olivo-Marin, J. C. Bayesian estimation for optimized structured illumination microscopy. *IEEE Transactions on Image Processing* **21,** 601–614. ISSN: 1057-7149. https://doi.org/10.1109/TIP.2011.2162741 (2012).

90. Lukeš, T. *et al. Comparison of image reconstruction methods for structured illumination microscopy* in *Biophotonics: Photonic Solutions for Better Health Care IV* (eds Popp, J., Tuchin, V. V., Matthews, D. L., Pavone, F. S. & Garside, P.) **9129** (SPIE, Brussels, Belgium, 2014), 1–13. https://doi.org/10.1117/12.2052621.

91. Mudry, E. *et al.* Structured illumination microscopy using unknown speckle patterns. *Nature Photonics* **6,** 312–315. ISSN: 1749-4885. https://doi.org/10.1038/nphoton.2012.83 (2012).

92. Huang, X. *et al.* Fast, long-term, super-resolution imaging with Hessian structured illumination microscopy. *Nature Biotechnology* **36,** 451–459. ISSN: 1087-0156. https://doi.org/10.1038/nbt.4115 (2018).

93. Perez, V., Chang, B.-J. & Stelzer, E. H. K. Optimal 2D-SIM reconstruction by two filtering steps with Richardson-Lucy deconvolution. *Scientific Reports* **6,** 1–11. ISSN: 2045-2322. https://doi.org/10.1038/srep37149 (2016).

94. Chu, K. *et al.* Image reconstruction for structured-illumination microscopy with low signal level. *Optics Express* **22,** 8687–8702. ISSN: 1094-4087. https://doi.org/10.1364/OE.22.008687 (2014).

95. Chakrova, N., Rieger, B. & Stallinga, S. Deconvolution methods for structured illumination microscopy. *Journal of the Optical Society of America A* **33,** B12–B20. ISSN: 1084-7529. https://doi.org/10.1364/JOSAA.33.000B12 (2016).

96. Frohn, J. T., Knapp, H. F. & Stemmer, A. True optical resolution beyond the Rayleigh limit achieved by standing wave illumination. *Proceedings of the National Academy of Sciences* **97,** 7232–7236. ISSN: 0027-8424. https://doi.org/10.1073/pnas.130181797 (2000).

97. Křížek, P. & Hagen, G. M. in *Microscopy: Science, Technology, Applications and Education* (eds Méndez-Vilas, A. & Díaz, J.) 4th, 1366–1377 (Formatex, 2010). ISBN: 978-84-614-6190-5.

98. Křížek, P., Raška, I. & Hagen, G. M. Flexible structured illumination microscope with a programmable illumination array. *Optics Express* **20,** 24585–24599. ISSN: 1094-4087. https://doi.org/10.1364/OE.20.024585 (2012).

99. Lal, A., Shan, C. & Xi, P. Structured Illumination Microscopy Image Reconstruction Algorithm. *IEEE Journal of Selected Topics in Quantum Electronics* **22,** 50–63. ISSN: 1077-260X. https://doi.org/10.1109/JSTQE.2016.2521542 (2016).

100. Demmerle, J. *et al.* Strategic and practical guidelines for successful structured illumination microscopy. *Nature Protocols* **12,** 988–1010. ISSN: 1754-2189. https://doi.org/10.1038/nprot.2017.019 (2017).

101. Hagen, G. M. *et al. Biological applications of an LCoS-based programmable array microscope (PAM)* in *Imaging, Manipulation, and Analysis of Biomolecules, Cells, and Tissues V* (eds Farkas, D. L., Leif, R. C. & Nicolau, D. V.) **6441** (SPIE, 2007), 1–12. ISBN: 0819465542. https://doi.org/10.1117/12.710995.

102. Werley, C. A., Chien, M.-P. & Cohen, A. E. Ultrawidefield microscope for high-speed fluorescence imaging and targeted optogenetic stimulation. *Biomedical Optics Express* **8,** 5794–5813. ISSN: 2156-7085. https://doi.org/10.1364/BOE.8.005794 (2017).

103. Dan, D. *et al.* DMD-based LED-illumination Super-resolution and optical sectioning microscopy. *Scientific Reports* **3,** 1–7. ISSN: 2045-2322. https://doi.org/10.1038/srep01116 (2013).

104. Hagen, G. M. *et al.* Fluorescence recovery after photobleaching and photoconversion in multiple arbitrary regions of interest using a programmable array microscope. *Microscopy Research and Technique* **72,** 431–440. ISSN: 1059-910X. https://doi.org/10.1002/jemt.20686 (2009).

105. Song, L. *et al.* Fast structured illumination microscopy using rolling shutter cameras. *Measurement Science and Technology* **27,** 1–6. ISSN: 0957-0233. https://doi.org/10.1088/0957-0233/27/5/055401 (2016).

106. Cvačková, Z., Mašata, M., Staněk, D., Fidlerová, H. & Raška, I. Chromatin position in human HepG2 cells: Although being non-random, significantly changed in daughter cells. *Journal of Structural Biology* **165,** 107–117. ISSN: 1047-8477. https://doi.org/10.1016/j.jsb.2008.10.007 (2009).

107. Young, L. J., Ströhl, F. & Kaminski, C. F. A guide to structured illumination TIRF microscopy at high speed with multiple colors. *Journal of Visualized Experiments* **2016,** 1–16. ISSN: 1940-087X. https://doi.org/10.3791/53988 (2016).

108. Förster, R. *et al.* Simple structured illumination microscope setup with high acquisition speed by using a spatial light modulator. *Optics Express* **22,** 20663–20677. ISSN: 1094-4087. https://doi.org/10.1364/OE.22.020663 (2014).

109. Lu-Walther, H.-W. *et al.* fastSIM: a practical implementation of fast structured illumination microscopy. *Methods and Applications in Fluorescence* **3,** 1–9. ISSN: 2050-6120. https://doi.org/10.1088/2050-6120/3/1/014001 (2015).

110. Kantelhardt, S. R. *et al.* Specific Visualization of Glioma Cells in Living Low-Grade Tumor Tissue. *PLoS ONE* **5** (ed Heintzmann, R.) 1–11. ISSN: 1932-6203. https://doi.org/10.1371/journal.pone.0011323 (2010).

111. Huang, F. *et al.* Video-rate nanoscopy using sCMOS camera-specific single-molecule localization algorithms. *Nature Methods* **10,** 653–658. ISSN: 1548-7091. https://doi.org/10.1038/nmeth.2488 (2013).

112. Goodman, J. W. in *Introduction to Fourier Optics* 2nd, 126–171 (McGraw-Hill Int., 1968).

113. Chung, E., Kim, D. & So, P. T. Extended resolution wide-field optical imaging: objective-launched standing-wave total internal reflection fluorescence microscopy. *Optics Letters* **31,** 945–947. ISSN: 0146-9592. https://doi.org/10.1364/OL.31.000945 (2006).

114. Sandmeyer, A. *et al.* DMD-based super-resolution structured illumination microscopy visualizes live cell dynamics at high speed and low cost. *bioRxiv,* 1–32. https://doi.org/10.1101/797670 (2019).

115. Wicker, K. Non-iterative determination of pattern phase in structured illumination microscopy using auto-correlations in Fourier space. *Optics Express* **21,** 24692–24701. ISSN: 1094-4087. https://doi.org/10.1364/OE.21.024692 (2013).

116. Wicker, K., Mandula, O., Best, G., Fiolka, R. & Heintzmann, R. Phase optimisation for structured illumination microscopy. *Optics Express* **21,** 2032–2049. ISSN: 1094-4087. https://doi.org/10.1364/OE.21.002032 (2013).

117. Guo, Y. *et al.* Visualizing Intracellular Organelle and Cytoskeletal Interactions at Nanoscale Resolution on Millisecond Timescales. *Cell* **175,** 1430–1442. ISSN: 0092-8674. https://doi.org/10.1016/j.cell.2018.09.057 (2018).

118. Löschberger, A. *et al. Super-Resolution Imaging by Dual Iterative Structured Illumination Microscopy* tech. rep. (Carl Zeiss NTS Ltd., 2021), 1–18. https://www.zeiss.com/microscopy/int/products/super-resolution/elyra-7.html.

119. Huang, F. *et al.* Ultra-High Resolution 3D Imaging of Whole Cells. *Cell* **166,** 1028–1040. ISSN: 1097-4172. https://doi.org/10.1016/j.cell.2016.06.016 (2016).

120. Lin, R., Kipreos, E. T., Zhu, J., Khang, C. H. & Kner, P. Subcellular three-dimensional imaging deep through multicellular thick samples by structured illumination microscopy and adaptive optics. *Nature Communications* **12,** 1–14. ISSN: 2041-1723. https://doi.org/10.1038/s41467-021-23449-6 (2021).

121. Roth, J., Mehl, J. & Rohrbach, A. Fast TIRF-SIM imaging of dynamic, low-fluorescent biological samples. *Biomedical Optics Express* **11,** 4008. ISSN: 2156-7085. https://doi.org/10.1364/BOE.391561 (2020).

122. Brunstein, M., Wicker, K., Hérault, K., Heintzmann, R. & Oheim, M. Full-field dual-color 100-nm super-resolution imaging reveals organization and dynamics of mitochondrial and ER networks. *Optics Express* **21,** 26162–26173. ISSN: 1094-4087. https://doi.org/10.1364/OE.21.026162 (2013).

123. Cnossen, J. *et al.* Localization microscopy at doubled precision with patterned illumination. *Nature Methods* **17,** 59–63. ISSN: 1548-7091. https://doi.org/10.1038/s41592-019-0657-7 (2020).

124. Reymond, L. *et al.* SIMPLE: Structured illumination based point localization estimator with enhanced precision. *Optics Express* **27,** 24578–24590. ISSN: 1094-4087. https://doi.org/10.1364/OE.27.024578 (2019).

125. Hyle Park, B. *et al.* Real-time fiber-based multi-functional spectral-domain optical coherence tomography at 13 µm. *Optics Express* **13,** 3931–3944. ISSN: 1094-4087. https://doi.org/10.1364/OPEX.13.003931 (2005).

126. Coquoz, S., Bouwens, A., Marchand, P. J., Extermann, J. & Lasser, T. Interferometric synthetic aperture microscopy for extended focus optical coherence microscopy. *Optics Express* **25,** 30807–30819. ISSN: 1094-4087. https://doi.org/10.1364/OE.25.030807 (2017).

127. Lukeš, T. *Super-Resolution Microscopy Live Cell Imaging and Image Analysis* PhD thesis (Czech Technical University in Prague, 2017), 1–95. https://hdl.handle.net/10467/66802.

128. Vainrub, A. Precise measurement of the resolution in light microscopy using Fourier transform. *Review of Scientific Instruments* **79,** 046112. ISSN: 0034-6748. https://doi.org/10.1063/1.2912954 (2008).

129. Boreman, G. D. in *Modulation Transfer Function in Optical and Electro-Optical Systems* 1–30 (SPIE, 2001). ISBN: 978-0-81-948045-3. https://doi.org/10.1117/3.419857.

130. Zhang, X. *et al. Measuring the modulation transfer function of image capture devices: what do the numbers really mean?* in *Image Quality and System Performance IX* (eds Gaykema, F. & Burns, P. D.) **8293** (SPIE, Burlingame, California, USA, 2012), 829307–829317. ISBN: 978-0-81-948940-1. https://doi.org/10.1117/12.912989.

131. Orych, A. Review of methods for determining the spatial resolution of UAV sensors. *International Archives of the Photogrammetry, Remote Sensing and Spatial Information Sciences - ISPRS Archives* **XL-1/W4,** 391–395. ISSN: 1682-1750. https://doi.org/10.5194/isprsarchives-XL-1-W4-391-2015 (2015).

132. Honkavaara, E. *et al.* A Permanent Test Field for Digital Photogrammetric Systems. *Photogrammetric Engineering and Remote Sensing* **1,** 95–106. ISSN: 0099-1112. https://doi.org/10.14358/PERS.74.1.95 (2008).

133. Cunningham, I. A. & Fenster, A. A method for modulation transfer function determination from edge profiles with correction for finite-element differentiation. *Medical Physics* **14,** 533–537. ISSN: 0094-2405. https://doi.org/10.1118/1.596064 (1987).

134. Tortarolo, G., Castello, M., Diaspro, A., Koho, S. & Vicidomini, G. Evaluating image resolution in stimulated emission depletion microscopy. *Optica* **5,** 32–35. ISSN: 2334-2536. https://doi.org/10.1364/OPTICA.5.000032 (2018).

135. Nieuwenhuizen, R. P. J. *et al.* Measuring image resolution in optical nanoscopy. *Nature Methods* **10,** 557–562. ISSN: 1548-7091. https://doi.org/10.1038/nmeth.2448 (2013).

136. Proakis, J. G. & Manolakis, D. G. *Digital Signal Processing Principoles, Algorithms and Applications* Third Edit, 1–968. ISBN: 978-0-13-373762-2 (Prentice-Hall, Inc., New Jersey, 1996).

137. Welch, P. D. The use of fast Fourier transform for the estimation of power spectra: A method based on time averaging over short, modified periodograms. *IEEE Transactions on Audio and Electroacoustics* **15,** 70–73. ISSN: 0018-9278. https://doi.org/10.1109/TAU.1967.1161901 (1967).

138. Stioca, P. & Moses, R. *Spectral analysis of signals* (ed Robbins, T.) 1–480. ISBN: 0-13-113956-8 (Prentice Hall, Inc., Upper Saddle River, New Jersey, 2005).

139. *MATLAB version 9.8.0.1323502 (R2020a)* Natick, Massachusetts, 2020.

140. Müller, M., Mönkemöller, V., Hennig, S., Hübner, W. & Huser, T. Open-source image reconstruction of super-resolution structured illumination microscopy data in ImageJ. *Nature Communications* **7,** 1–6. ISSN: 2041-1723. https://doi.org/10.1038/ncomms10980 (2016).

141. Heintzmann, R. in *Handbook Of Biological Confocal Microscopy* 265–279 (Springer US, Boston, MA, 2006). https://doi.org/10.1007/978-0-387-45524-2_13.

142. Verveer, P. J. & Jovin, T. M. Efficient superresolution restoration algorithms using maximum a posteriori estimations with application to fluorescence microscopy. *Journal of the Optical Society of America A* **14,** 1696–1706. ISSN: 1084-7529. https://doi.org/10.1364/JOSAA.14.001696 (1997).

143. Verveer, P. J., Gemkow, M. J. & Jovin, T. M. A comparison of image restoration approaches applied to three- dimensional confocal and wide-field fluorescence microscopy. *Journal of Microscopy* **193,** 50–61. ISSN: 0022-2720. https://doi.org/10.1046/j.1365-2818.1999.00421.x (1999).

144. Vermolen, B. J., Garini, Y. & Young, I. T. 3D restoration with multiple images acquired by a modified conventional microscope. *Microscopy Research and Technique* **64,** 113–125. ISSN: 1059-910X. https://doi.org/10.1002/jemt.20072 (2004).

145. Chaudhuri, S. *Super-Resolution Imaging* (ed Chaudhuri, S.) ISBN: 0-7923-7471-1. https://doi.org/10.1007/b117840 (Kluwer Academic Publishers, Boston, 2002).

146. Saxton, M. J. & Jacobson, K. SINGLE-PARTICLE TRACKING:Applications to Membrane Dynamics. *Annual Review of Biophysics and Biomolecular Structure* **26,** 373–399. ISSN: 1056-8700. https://doi.org/10.1146/annurev.biophys.26.1.373 (1997).

147. Suzuki, K., Ritchie, K., Kajikawa, E., Fujiwara, T. & Kusumi, A. Rapid Hop Diffusion of a G-Protein-Coupled Receptor in the Plasma Membrane as Revealed by Single-Molecule Techniques. *Biophysical Journal* **88,** 3659–3680. ISSN: 0006-3495. https://doi.org/10.1529/biophysj.104.048538 (2005).

148. Kusumi, A., Sako, Y. & Yamamoto, M. Confined lateral diffusion of membrane receptors as studied by single particle tracking (nanovid microscopy). Effects of calcium-induced differentiation in cultured epithelial cells. *Biophysical Journal* **65,** 2021–2040. ISSN: 0006-3495. https://doi.org/10.1016/S0006-3495(93)81253-0 (1993).

149. Chenouard, N. *et al.* Objective comparison of particle tracking methods. *Nature Methods* **11,** 281–289. ISSN: 1548-7091. https://doi.org/10.1038/nmeth.2808 (2014).

150. Andrews, N. L. *et al.* Actin restricts FceRI diffusion and facilitates antigen-induced receptor immobilization. *Nature Cell Biology* **10,** 955–963. ISSN: 1465-7392. https://doi.org/10.1038/ncb1755 (2008).

151. *DIPimage | DIPlib* https://diplib.org/DIPimage.html.

Publications of the Author Relevant to the Thesis

Publications in Impacted Journals

A1. Pospíšil, J., Wiebusch, G., Fliegel, K., Klíma, M. & Huser, T., A highly compact and cost-effective two-beam super-resolution structured illumination microscope based on all-fiber optic components. *Optics Express* **29**, 11833–11844. ISSN: 1094-4087. https://doi.org/10.1364/OE.420592 (2021).

The author participated in the device development, data acquisition, image processing, and data analysis. Shares: **20**/20/20/20/20

A2. Pospíšil, J., Lukeš, T., Bendesky, J., Fliegel, K., Spendier, K. & Hagen, G. M., Imaging tissues and cells beyond the diffraction limit with structured illumination microscopy and Bayesian image reconstruction. *GigaScience* **8**, 1–12. ISSN: 2047-217X. https://doi.org/10.1093/gigascience/giy126 (2019).

Supporting data for "Imaging tissues and cells beyond the diffraction limit with structured illumination microscopy and Bayesian imagereconstruction." GigaDB. https://doi.org/10.5524/100514 (2018).

The author participated in the software development, and data analysis. Shares: **17**/17/17/17/17/17

A3. Lukeš, T., Pospíšil, J., Fliegel, K., Lasser, T. & Hagen, G. M. Quantitative super-resolution single molecule microscopy dataset of YFP-tagged growth factor receptors. *GigaScience* **7**, 1–10. ISSN: 2047-217X. https://doi.org/10.1093/gigascience/giy002 (2018).

The author participated in the software development, and data analysis. Shares: 20/**20**/20/20/20

A4. Pilger, C., Pospíšil, J., Müller, M., Ruoff, M., Schütte, M., Spiecker, H. & Huser, T. Super-resolution fluorescence microscopy by line-scanning with an unmodified two-photon microscope. *Philosophical Transactions of the Royal Society A* **379**, 1–11. ISSN: 1364-503X. https://doi.org/10.1098/rsta.2020.0300 (2021).

The author participated in the data analysis. Shares: 14/**14**/14/14/14/14/14

Publications Excerpted by ISI

A5. Pospíšil, J., Fliegel, K., Švihlík, J. & Klíma, M. *Evaluation resolution in live cell structured illumination microscopy* in *Applications of Digital Image Processing XLII* (eds Tescher, A. & Ebrahimi, T.) **11137** (SPIE, San Diego, California, USA, 2019). ISSN: 0277-786X. https://doi.org/10.1117/12.2527885

The author participated in the software development, image processing, and data analysis. Shares: **25**/25/25/25

A6. Pospíšil, J., Fliegel, K., Švihlík, J. & Klíma, M. *Comparison of resolution estimation methods in optical microscopy* in *Applications of Digital Image Processing XLI* (eds Tescher, A.) **10752** (SPIE, San Diego, California, USA, 2018). ISSN: 1996-756X. https://doi.org/10.1117/12.2321301

The author participated in the software development, data acquisition, image processing, and data analysis. Shares: **25**/25/25/25

A7. Pospíšil, J., Fliegel, K. & Klíma, M. *Assessing resolution in live cell structured illumination microscopy* in *Photonics, Devices, and Systems VII* (eds Páta, P. & Fliegel, K.) **10603** (SPIE, Prague, Czech Republic, 2017). ISSN: 0277-786X. https://doi.org/10.1117/12.2292793

The author participated in the software development, image processing, and data analysis. Shares: **33**/33/33

A8. Pospíšil, J., Fliegel, K. & Klíma, M. *Analysis of image reconstruction artifacts in structured illumination microscopy* in *Applications of Digital Image Processing XL* (eds Tescher, A.) **10396** (SPIE, San Diego, California, USA, 2017). ISSN: 0277-786X. https://doi.org/10.1117/12.2274418

The author participated in the software development, image processing, and data analysis. Shares: **33**/33/33

A9. Pospíšil, J., Fliegel, K. & Klíma, M. *Phase estimation of illumination pattern in structured illumination microscopy* in *27th International Conference Radioelektronika (RADIOELEKTRONIKA)* (IEEE, Brno, Czech Republic, 2017). ISBN: 978-1-5090-4591-4 https://doi.org/10.1109/RADIOELEK.2017.7937590

The author participated in the software development, image processing, and data analysis. Shares: **33**/33/33

A10. Janout, P., Pospíšil, J., Fliegel, K., Klíma, M. & Páta, P. *Interpolation methods for the improvement of the point spread function estimation* in *28th International Conference Radioelektronika* (IEEE, Prague, Czech Republic, 2018). ISBN: 978-1-5386-2485-2. https://doi.org/10.1109/RADIOELEK.2018.8376375

The author participated in the data analysis. Shares: 20/**20**/20/20/20

Other Publications of the Author

A11. Willème, A., Mahmoudpour, S., Viola, I., Fliegel, K., Pospíšil, J., Ebrahimi, T., Schelkens, P., Descampe, A., Macq, B. *Overview of the JPEG XS core coding system subjective evaluations* in *Applications of Digital Image Processing XLI* **10752** (SPIE, San Diego, California, USA, 2018). ISSN: 0277-786X. https://doi.org/10.1117/12.2323435

The author participated in performing subjective tests.
Shares: 11/11/11/11/**11**/11/11/11/11

A12. Pospíšil, J. *Hot Pixels Suppression in Structured Illumination Microscopy* in *Proceedings of the International Student Scientific Conference Poster* (CTU in Prague, Prague, Czech Republic, 2017). http://poseidon2.feld.cvut.cz/conf/poster/proceedings/Poster_2017/Section_EI/EI_041_Pospisil.pdf

The author participated in the software development, image processing, and data analysis. Shares: **100**

A13. Novotný, M., Pospíšil, J., Čmejla, R. & Rusz, J. *Automatic detection of voice onset time in dysarthric speech* in *IEEE International Conference on Acoustics, Speech, and Signal Processing* (IEEE, New Jersey, USA, 2015). ISSN: 2379-190X. https://doi.org/10.1109/ICASSP.2015.7178790

The author participated in the software development, and data analysis.
Shares: 25/**25**/25/25

Activities

Participation in Projects

European Union's Horizon 2020 research and innovation program under the Marie Skłodowska-Curie Grant Agreement

- *DeLIVER*
  no. 766181

Ministry of Industry and Trade

- *Videodetection of persons in tunnels in real-time*
  no. FV20548

Czech Science Foundation

- *Multicriteria optimization of shift-variant imaging system models*
  no. GA17-05840S

Student grant agency of CTU in Prague

- *Modern Optical Imaging Systems with Non-linear Point Spread Function and Advanced Algorithms for Image Data Processing*
  no. SGS20/179/OHK3/3T/13

- *Analysis and advanced algorithms for ultra-wide imaging systems*
  no. SGS18/141/OHK3/2T/13

- *Algorithms for video-sequenced live cell super-resolution microscopy*
  no. SGS16/167/OHK3/2T/13

Internships and Training Schools

Secondments during DeLIVER project:

- **Institution:** Department of Biochemistry at University of Oxford, UK
  Supervisor: Dr. Lothar Schermelleh
  Topic: Super-resolution imaging and analysis of living cells

- **Institution:** Dynamic Optics and Photonics, Department of Biochemistry at University of Oxford, UK
  Supervisor: Prof. Martin Booth
  Topic: Adaptive optics in super-resolution microscopy

Internship:

- **Institution:** Laboratoire d'Optique Biomédicale, École polytechnique fédérale de Lausanne, Switzerland
  Supervisor: Prof. Theo Laser
  Topic: Simulations of a structured illumination microscope system

Training School:

- **Name:** 2016 IEEE-EURASIP Summer School on Signal Processing (S3P-2016)
  Organized by: IEEE Signal Processing Society, European Association for Signal Processing, GTTI: Italian Group for Telecommunications and Information Technology, University of Trento, Italy
  Topic: Semantics in Media
  Received award: IEEE "Raising star" award for poster presentation

COMPACT STRUCTURED ILLUMINATION MICROSCOPY AND PERFORMANCE EVALUATION IN LIVE CELL SUPER-RESOLUTION IMAGING

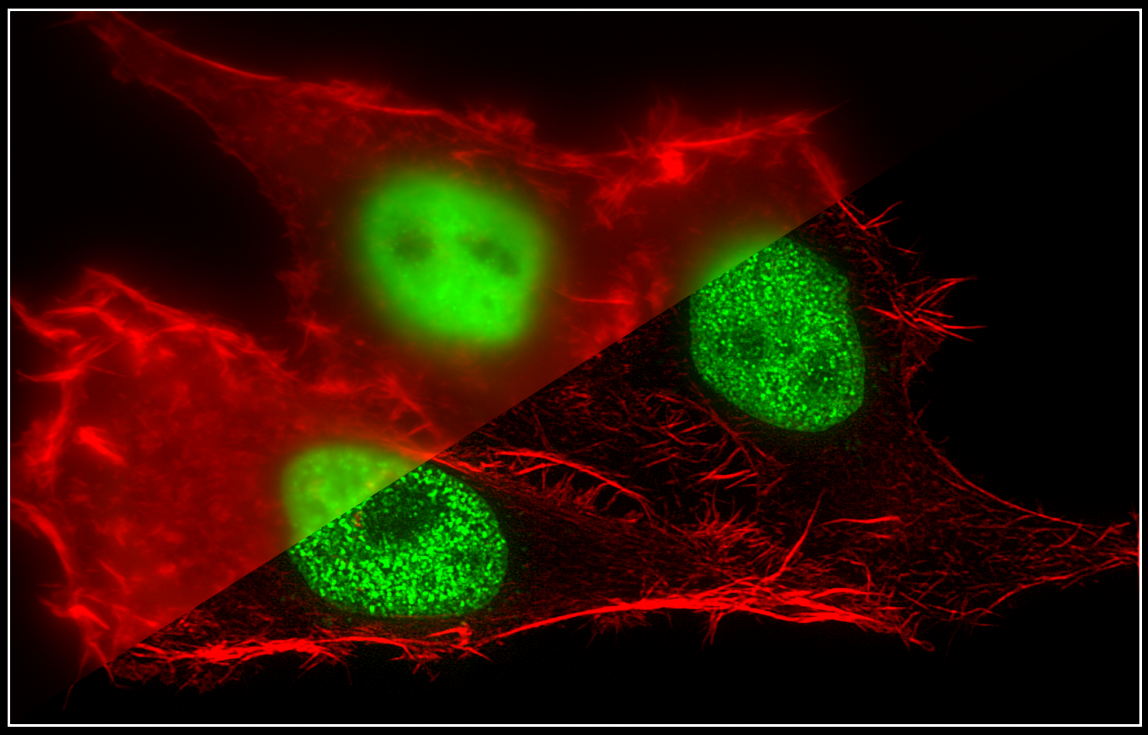

FACULTY
OF ELECTRICAL
ENGINEERING
CTU IN PRAGUE

2021